

INFORMATION TO USERS

This manuscript has been reproduced from the microfilm master. UMI films the text directly from the original or copy submitted. Thus, some thesis and dissertation copies are in typewriter face, while others may be from any type of computer printer.

The quality of this reproduction is dependent upon the quality of the copy submitted. Broken or indistinct print, colored or poor quality illustrations and photographs, print bleedthrough, substandard margins, and improper alignment can adversely affect reproduction.

In the unlikely event that the author did not send UMI a complete manuscript and there are missing pages, these will be noted. Also, if unauthorized copyright material had to be removed, a note will indicate the deletion.

Oversize materials (e.g., maps, drawings, charts) are reproduced by sectioning the original, beginning at the upper left-hand corner and continuing from left to right in equal sections with small overlaps. Each original is also photographed in one exposure and is included in reduced form at the back of the book.

Photographs included in the original manuscript have been reproduced xerographically in this copy. Higher quality 6" x 9" black and white photographic prints are available for any photographs or illustrations appearing in this copy for an additional charge. Contact UMI directly to order.

UMI

A Bell & Howell Information Company
300 North Zeeb Road, Ann Arbor MI 48106-1346 USA
313/761-4700 800/521-0600



UNIVERSITY OF OKLAHOMA

GRADUATE COLLEGE

**SCALAR MEASUREMENTS AND ANALYSIS OF HYDROGEN GAS-JET
DIFFUSION FLAMES IN NORMAL AND MICROGRAVITY**

A Dissertation

SUBMITTED TO THE GRADUATE FACULTY

in partial fulfillment of the requirements for

the degree of

Doctor of Philosophy

By

Khalid N. Al-Ammar
Norman, Oklahoma
1998

UMI Number: 9914407

**UMI Microform 9914407
Copyright 1999, by UMI Company. All rights reserved.**

**This microform edition is protected against unauthorized
copying under Title 17, United States Code.**

UMI
300 North Zeeb Road
Ann Arbor, MI 48103

© Copyright Khalid N. Al-Ammar 1998
All Rights Reserved

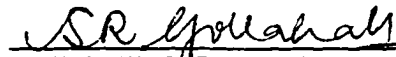
**SCALAR MEASUREMENTS AND ANALYSIS OF HYDROGEN GAS-JET
DIFFUSION FLAMES IN NORMAL AND MICROGRAVITY**

A Dissertation APPROVED FOR THE
SCHOOL OF AEROSPACE AND MECHANICAL ENGINEERING

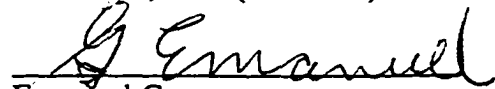
BY



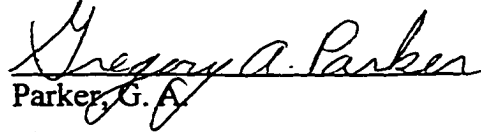
Agrawal, A. K. (Chair)



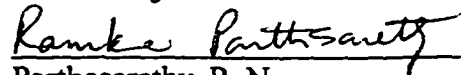
Gollahalli, S. R. (Co-Chair)



Emanuel G.



Parker, G. A.



Parthasarathy, R. N.

ACKNOWLEDGMENT

First, I would like to thank Allah, the almighty, for his blessings and countless bounties that He bestowed on my family and me. I thank Him for His protection, and I ask Him His mercy and forgiveness for me, my parents, and for my family.

I sincerely thank my advisor Dr. A. K. Agrawal for his continuous guidance and support throughout my graduate years. I thank him for his academic and experimental guidance, and I hope that my work with him had marked the beginning of a life-long relationship.

I also thank my co-advisor Dr. S. R. Gollahalli, Lesch Centennial Professor of Aerospace and Mechanical Engineering, for his academic support and guidance throughout my graduate years. I cherish his countless advice to me, and I will always be indebted to him.

Special thanks are extended to the members of my advisory committee Dr. G. Emanuel, Dr. G. A. Parker, and Dr. R. N. Parthasarathy for their support and guidance. I also thank them for teaching me during my undergraduate and graduate years.

I also would like to thank Dr. DeVon Griffin and members of the drop tower at NASA Lewis Research Center for their technical help and support.

Also, special thanks are extended to my colleagues Anil Kumar Shenoy, Steven Cherry, and Burt W. Albers for their help and support.

Finally, I would like to thank members of the AME machine shop, including Billy Mays, Mark Winn, Trent Hobbs, and Greg Williams for their time and efforts.

Dedicated to

my father and my mother, my wife and my daughter,
and my brother Muhammad

May Allah reward you all.

TABLE OF CONTENTS

Chapter 1	INTRODUCTION	1
	1.1 Background	1
	1.1.1 Diffusion Flames	1
	1.1.2 Buoyancy Effects on Laminar Diffusion Flames	5
	1.1.3 Buoyancy Effects on Transitional Diffusion Flames	12
	1.2 Objectives and Scope of the Present Study	14
Chapter 2	APPLICATION OF EXISTING THEORY	16
	2.1 Diffusion Flames in Microgravity	17
	2.1.1 Model I	17
	2.1.2 Model II	20
	2.1 Diffusion Flames in Normal Gravity	23
Chapter 3	EXPERIMENTAL SETUP AND PROCEDURE	30
	3.1 Drop Test Rig	30
	3.1.1 Rainbow Schlieren Deflectometry (RSD)	31
	3.1.1.1 RSD Apparatus	32
	3.1.1.2 Abel Inversion	33
	3.1.1.3 State Relationships	35
	3.1.1.4 Error Analysis	38
	3.1.2 Fuel Supply and Ignition Systems	39
	3.1.3 Data Acquisition and Control Systems	39
	3.1.4 Power Distribution System	40
	3.2 Normal Gravity Probe Measurements	40

	3.2.1 Oxygen Mole Fraction	40
	3.2.2 Temperature Measurement	41
	3.3 Test Procedure	42
	3.3.1 Drop Tower	42
	3.3.2 Drop Procedure	42
Chapter 4	RESULTS AND DISCUSSION	58
	4.1 Probe and RSD Measurements in Normal Gravity	58
	4.2 RSD Measurements	59
	4.3 Buoyancy Effects on Laminar Diffusion Flames	61
	4.3.1 Base-Line Case	72
	4.3.1.1 Temporal Evolution of Flame in the Drop Tower	72
	4.3.1.2 Scalar Profiles	88
	4.3.1.3 Flame Shape	88
	4.3.2 Burner Diameter Effect	89
	4.3.3 Scaling with Reynolds Number	101
	4.3.4 Comparison with Theory	124
	4.4 Buoyancy Effects on Transitional Diffusion Flames	127
	4.4.1 Reynolds Number Effect	127
	4.4.2 Helium Dilution Effect	147
Chapter 5	CONCLUSIONS AND RECOMMENDATIONS	167
	REFERENCES	171
	APPENDIX A	178
	APPENDIX B	180

LIST OF FIGURES

Figure 2.1: An axisymmetric jet	24
Figure 2.2: Flame height coefficient as a function of Reynolds number	25
Figure 2.3: Mixture fraction distribution: $Re_T = 500$, $Sc = 0.7$, $d = 1.19$ mm, and $z/d = 10$	26
Figure 2.4: Mixture fraction distribution: $Re_T = 100$, $Sc = 0.7$, $d = 1.19$ mm, and $z/d = 2$	27
Figure 2.5: Mixture fraction distribution: $Re_T = 500$, $Sc=0.2$, $d = 1.19$ mm, and $z/d=10$	28
Figure 2.6: Mixture fraction distribution: $Re_T=100$, $Sc=0.2$, $d = 1.19$ mm, and $z/d=2$	29
Figure 3.1: A photograph of the drop rig	44
Figure 3.2: Optical layout of the rainbow schlieren	45
Figure 3.3: A photograph of the symmetric color filter	46
Figure 3.4: Light ray traversing a non-uniform refractive index field	47
Figure 3.5: Ray displacement at the knife-edge for a given angular deflection	48
Figure 3.6: Filter calibration curve	49
Figure 3.7: Measured and computed profiles of temperature versus mixture fraction	50
Figure 3.8: Temperature versus normalized refractive index difference at chemical equilibrium	51
Figure 3.9: Oxygen mole fraction versus normalized refractive index difference at chemical equilibrium	52
Figure 3.10: Error coefficient versus radial location	53
Figure 3.11: Schematic of the fuel supply system	54
Figure 3.12: Power distribution system	55

Figure 3.13: Sampling probe	56
Figure 3.14: Drop rig inside the drag shield during the drop	57
Figure 4.1.1: Temperature versus oxygen mole fraction; $Re = 70$, $d = 1.19$ mm, and $z/d = 4.2$	62
Figure 4.1.2: Temperature versus oxygen mole fraction; $Re = 70$, $d = 1.19$ mm, and $z/d = 8.4$	63
Figure 4.2.1: Schlieren image of hydrogen gas-jet diffusion flame in normal gravity; $Re = 70$ and $d = 1.19$ mm	64
Figure 4.2.2: Hue distribution; $Re = 70$, $d = 1.19$ mm, and $z/d = 4.2$	65
Figure 4.2.3: Angular deflection distribution; $Re = 70$, $d = 1.19$ mm, and $z/d = 4.2$	66
Figure 4.2.4: Normalized refractive index distribution; $Re = 70$, $d = 1.19$ mm, and $z/d = 4.2$	67
Figure 4.2.5: Oxygen mole fraction; $Re = 70$, $d = 1.19$ mm, and $z/d = 4.2$	68
Figure 4.2.6: Temperature distribution; $Re = 70$, $d = 1.19$ mm, and $z/d = 4.2$	69
Figure 4.2.7: Oxygen mole fraction; $Re = 70$, $d = 1.19$ mm, and $z/d = 8.4$	70
Figure 4.2.8: Temperature distribution; $Re = 70$, $d = 1.19$ mm, and $z/d = 8.4$	71
Figure 4.3.1: Schlieren images of hydrogen gas-jet diffusion flame in normal (a) and microgravity (b); $Re = 70$ and $d = 1.19$ mm	75
Figure 4.3.2: Contours of angular deflection in units of 10^{-4} radians; $Re = 70$, $d = 1.19$ mm, and $t = 0$ s	76
Figure 4.3.3: Contours of angular deflection in units of 10^{-4} radians; $Re = 70$, $d = 1.19$ mm, and $t = 0.2$ s	77
Figure 4.3.4: Contours of angular deflection in units of 10^{-4} radians; $Re = 70$, $d = 1.19$ mm, and $t = 0.41$ s	78

Figure 4.3.5: Contours of angular deflection in units of 10^{-4} radians; Re = 70, d = 1.19 mm, and t = 0.61 s	79
Figure 4.3.6: Contours of angular deflection in units of 10^{-4} radians; Re = 70, d = 1.19 mm, and t = 0.78 s	80
Figure 4.3.7: Contours of angular deflection in units of 10^{-4} radians; Re = 70, d = 1.19 mm, and t = 1.01 s	81
Figure 4.3.8: Contours of angular deflection in units of 10^{-4} radians; Re = 70, d = 1.19 mm, and t = 1.25 s	82
Figure 4.3.9: Contours of angular deflection in units of 10^{-4} radians; Re = 70, d = 1.19 mm, and t = 1.47 s	83
Figure 4.3.10: Contours of angular deflection in units of 10^{-4} radians; Re = 70, d = 1.19 mm, and t = 1.62 s	84
Figure 4.3.11: Contours of angular deflection in units of 10^{-4} radians; Re = 70, d = 1.19 mm, and t = 1.82 s	85
Figure 4.3.12: Contours of angular deflection in units of 10^{-4} radians; Re = 70, d = 1.19 mm, and t = 1.95 s	86
Figure 4.3.13: Contours of angular deflection in units of 10^{-4} radians; Re = 70, d = 1.19 mm, and t = 2.14 s	87
Figure 4.3.14: Temperature profiles during the drop; z/d = 4, Re = 70, and d = 1.19 mm	90
Figure 4.3.15: Temperature profiles during the drop; z/d = 8, Re = 70, and d = 1.19 mm	91
Figure 4.3.16: Buoyancy effects on normalized refractive index difference profiles; Re = 70, d = 1.19 mm, and z/d = 4	92
Figure 4.3.17: Buoyancy effects on oxygen mole fraction profiles; Re = 70, d = 1.19 mm, and z/d = 4	93
Figure 4.3.18: Buoyancy effects on temperature profiles; Re = 70, d = 1.19 mm, and z/d = 4	94
Figure 4.3.19: Buoyancy effects on oxygen mole fraction profiles; Re = 70, d = 1.19 mm, and z/d = 8	95

Figure 4.3.20: Buoyancy effects on temperature profiles; $Re = 70$, $d = 1.19$ mm, and $z/d = 8$	96
Figure 4.3.21: Buoyancy effect on flame shape; $Re = 70$ and $d = 1.19$ mm	97
Figure 4.3.22: Contours of angular deflection in units of 10^{-4} radians in normal gravity; $Re = 70$ and $d = 0.3$ mm	102
Figure 4.3.23: Contours of angular deflection in units of 10^{-4} radians in microgravity; $Re = 70$ and $d = 0.3$ mm	103
Figure 4.3.24: Temperature profiles during the drop; $z/d = 4$, $Re = 70$, and $d = 0.3$ mm	104
Figure 4.3.25: Temperature profiles during the drop; $z/d = 8$, $Re = 70$, and $d = 0.3$ mm	105
Figure 4.3.26: Burner diameter effect on oxygen mole fraction profiles in normal and microgravity; $Re = 70$ and $z/d = 4$	106
Figure 4.3.27: Burner diameter effect on temperature profiles in normal and microgravity; $Re = 70$ and $z/d = 4$	107
Figure 4.3.28: Burner diameter effect on oxygen mole fraction profiles in normal and microgravity; $Re = 70$ and $z/d = 8$	108
Figure 4.3.29: Burner diameter effect on temperature profiles in normal and microgravity; $Re = 70$ and $z/d = 8$	109
Figure 4.3.30: Burner diameter effect on flame shape in normal and microgravity; $Re = 70$	110
Figure 4.3.31: Contours of angular deflection in units of 10^{-4} radians in normal gravity; $Re = 40$ and $d = 1.19$ mm	111
Figure 4.3.32: Contours of angular deflection in units of 10^{-4} radians in microgravity; $Re = 40$ and $d = 1.19$ mm	112
Figure 4.3.33: Contours of angular deflection in units of 10^{-4} radians in normal gravity; $Re = 40$ and $d = 0.3$ mm	113
Figure 4.3.34: Contours of angular deflection in units of 10^{-4} radians in microgravity; $Re = 40$ and $d = 0.3$ mm	114
Figure 4.3.35: Temperature profiles during the drop; $z/d = 4$, $Re = 40$, and $d = 1.19$ mm	115

Figure 4.3.36: Temperature profiles during the drop; $z/d = 8$, $Re = 40$, and $d = 1.19$ mm	116
Figure 4.3.37: Temperature profiles during the drop; $z/d = 4$, $Re = 40$, and $d = 0.3$ mm	117
Figure 4.3.38: Temperature profiles during the drop; $z/d = 8$, $Re = 40$, and $d = 0.3$ mm	118
Figure 4.3.39: Burner diameter effect on oxygen mole fraction profiles in normal and microgravity; $Re = 40$ and $z/d = 4$	119
Figure 4.3.40: Burner diameter effect on temperature profiles in normal and microgravity; $Re = 40$ and $z/d = 4$	120
Figure 4.3.41: Burner diameter effect on oxygen mole fraction profiles in normal and microgravity; $Re = 40$ and $z/d = 8$	121
Figure 4.3.42: Burner diameter effect on temperature profiles in normal and microgravity; $Re = 40$ and $z/d = 8$	122
Figure 4.3.43: Burner diameter effect on flame shape in normal and microgravity; $Re = 40$	123
Figure 4.3.44: Reynolds number effect on oxygen mole fraction profiles in normal and microgravity; $d = 1.19$ mm, $z/d = 4$ for $Re = 70$, and $z/d = 2.3$ for $Re = 40$	128
Figure 4.3.45: Reynolds number effect on temperature profiles in normal and microgravity; $d = 1.19$ mm, $z/d = 4$ for $Re = 70$, and $z/d = 2.3$ for $Re = 40$	129
Figure 4.3.46: Reynolds number effect on oxygen mole fraction profiles in normal and microgravity; $d = 0.3$ mm, $z/d = 4$ for $Re = 70$, and $z/d = 2.3$ for $Re = 40$	130
Figure 4.3.47: Reynolds number effect on temperature profiles in normal and microgravity; $d = 0.3$ mm, $z/d = 4$ for $Re = 70$, and $z/d = 2.3$ for $Re = 40$	131
Figure 4.3.48: Reynolds number effect on flame shape in normal and microgravity; $d = 1.19$ mm	132
Figure 4.3.49: Reynolds number effect on flame shape in normal and microgravity; $d = 0.3$ mm	133

Figure 4.3.50: Oxygen mole fraction profiles from RSD and theory in microgravity; $Re = 70$ ($Re_T = 130$) and $z/d = 4$	134
Figure 4.3.51: Flame shape from the RSD and theory in microgravity; $Re = 70$ ($Re_T = 130$)	135
Figure 4.3.52: Oxygen mole fraction profiles from RSD and theory in microgravity; $Re = 70$ ($Re_T = 130$) and $z/d = 4$	136
Figure 4.3.53: Temperature profiles from RSD and theory in microgravity; $Re = 70$ ($Re_T = 130$) and $z/d = 4$	137
Figure 4.3.54: Oxygen mole fraction profiles from RSD and theory in microgravity; $Re = 70$ ($Re_T = 130$) and $z/d = 8$	138
Figure 4.3.55: Temperature profiles from RSD and theory in microgravity; $Re = 70$ ($Re_T = 130$) and $z/d = 8$	139
Figure 4.3.56: Flame shape from RSD and theory in microgravity; $Re = 70$ ($Re_T = 130$)	140
Figure 4.3.57: Oxygen mole fraction profiles from RSD and theory in microgravity; $Re = 40$ ($Re_T = 10$) and $z/d = 4$	141
Figure 4.3.58: Temperature profiles from RSD and theory in microgravity; $Re = 40$ ($Re_T = 10$) and $z/d = 4$	142
Figure 4.3.59: Oxygen mole fraction profiles from RSD and theory in microgravity; $Re = 40$ ($Re_T = 10$) and $z/d = 8$	143
Figure 4.3.60: Temperature profiles from RSD and theory in microgravity; $Re = 40$ ($Re_T = 10$) and $z/d = 8$	144
Figure 4.3.61: Flame shape from RSD and theory in microgravity; $Re = 40$ ($Re_T = 10$)	145
Figure 4.4.1: Schlieren images of hydrogen gas-jet diffusion flame in normal (a) and microgravity (b); $Re = 1500$ and $d = 0.3$ mm	149
Figure 4.4.2: Contours of angular deflection in units of 10^{-4} radians in normal gravity; $Re = 1300$ and $d = 0.3$ mm	150
Figure 4.4.3: Contours of angular deflection in units of 10^{-4} radians in microgravity; $Re = 1300$ and $d = 0.3$ mm	151

Figure 4.4.4: Contours of angular deflection in units of 10^{-4} radians in normal gravity; $Re = 1500$ and $d = 0.3$ mm	152
Figure 4.4.5: Contours of angular deflection in units of 10^{-4} radians in microgravity; $Re = 1500$ and $d = 0.3$ mm	153
Figure 4.4.6: Contours of angular deflection in units of 10^{-4} radians in normal gravity; $Re = 1700$ and $d = 0.3$ mm	154
Figure 4.4.7: Contours of angular deflection in units of 10^{-4} radians in microgravity; $Re = 1700$ and $d = 0.3$ mm	155
Figure 4.4.8: Transitional height as a function of Reynolds number for the pure hydrogen case; $d = 0.3$ mm	156
Figure 4.4.9: Buoyancy effect on oxygen mole fraction profiles in normal and microgravity; $d = 0.3$ mm, $z/d = 20$ for $Re = 1700$, and $z/d = 15.3$ for $Re = 1300$	157
Figure 4.4.10: Buoyancy effect on temperature profiles in normal and microgravity; $d = 0.3$ mm, $z/d = 20$ for $Re = 1700$, and $z/d = 15.3$ for $Re = 1300$	158
Figure 4.4.11: Contours of angular deflection in units of 10^{-4} radians in normal gravity; $Re = 1700$, $d = 0.3$ mm, and 0.2 He (molar)	159
Figure 4.4.12: Contours of angular deflection in units of 10^{-4} radians in microgravity; $Re = 1700$, $d = 0.3$ mm, and 0.2 He (molar)	160
Figure 4.4.13: Contours of angular deflection in units of 10^{-4} radians in normal gravity; $Re = 1700$, $d = 0.3$ mm, and 0.4 He (molar)	161
Figure 4.4.14: Contours of angular deflection in units of 10^{-4} radians in microgravity; $Re = 1700$, $d = 0.3$ mm, and 0.4 He (molar)	162
Figure 4.4.15: Transitional height as a function of helium mole fraction in hydrogen; $Re = 1700$ and $d = 0.3$ mm	163
Figure 4.4.16: Helium mole fraction profiles; $Re = 1700$, $d = 0.3$ mm, and $z/d = 20$	164
Figure 4.4.17: Helium dilution effect on oxygen mole fraction profiles in normal and microgravity; $Re = 1700$, $d = 0.3$ mm, and $z/d = 20$	165

Figure 4.4.18: Helium dilution effect on temperature profiles in normal and microgravity; $Re = 1700$, $d = 0.3$ mm, and $z/d = 20$	166
Figure B1: Temperature versus mixture fraction as obtained from chemical equilibrium calculation	184
Figure B2: Oxygen mole fraction versus mixture fraction as obtained from chemical equilibrium calculation	185

•

NOMENCLATURE

English Symbols

a a parameter

b a parameter

d burner inner diameter, displacement at the filter plane

D mass diffusivity, a parameter

f focal length of the decollimating lens, mixture fraction

Fr Froude number = $\frac{u_o^2}{g d}$

ID inner diameter

M molecular weight

n refractive index of the medium normalized by that of air

P Pressure

r radial coordinate

Re Jet-exit Reynolds number = $\frac{u_o d}{v_o}$

Re_T Theoretical Reynolds number = $\frac{u_o d}{v_\infty} \sqrt{\frac{\rho_o}{\rho_\infty}}$

R_u universal gas constant

S_c Schmidt number = $\frac{v_\infty}{D}$

T temperature

u axial velocity

v radial velocity
y radial distance
z axial coordinate

Greek Symbols

δ normalized refractive index difference
 Δ uncertainty
 ε angular deflection
 κ Dale-Gladstone constant
 ν kinematic viscosity
 ξ similarity variable

Subscripts

o burner exit condition
st stoichiometric

ABSTRACT

The quantitative Rainbow Schlieren Deflectometry (RSD) technique was used for the first time to measure scalar profiles in laminar and transitional hydrogen gas-jet diffusion flames burning in quiescent air in normal and microgravity. The angular deflection data obtained across the field-of-view by the RSD technique were used with Abel inversion to find the refractive index of the reacting mixture. The refractive index was related to the temperature and oxygen mole using the conserved scalar approach, combined with chemical equilibrium. Probe measurements of temperature and oxygen mole fraction were taken to validate the RSD technique. Good agreement was reached between the probe and RSD measurements in the fuel-lean side of the flame surface. The RSD measurements in the fuel-rich side of the flame were less reliable, in part, because of the measurement uncertainty and the assumption of chemical equilibrium.

Contour plots of angular deflection reveal higher radial gradients in normal gravity compared to those in microgravity. Temperature profiles during transition from normal to microgravity in the drop tower were obtained to determine the extent of steady-state microgravity conditions achieved in experiments. The results show that the high temperature regions e.g., the flame surface, reached steady-state prior to the lower temperature regions e.g., the schlieren boundary. The time to reach steady-state decreased as the jet exit Reynolds number was increased. The schlieren boundary did not reach steady-state at low jet exit Reynolds numbers because of the greater influence of gravity.

Effects of burner diameter and jet exit Reynolds number on flame shape and scalar profiles in normal and microgravity were evaluated. It was confirmed that the flame height varies linearly with Reynolds number in the laminar cases. Further, the flame height was shown to be independent of gravity within the range of jet-exit Reynolds numbers used (40 to 70). At a given jet-exit Reynolds number, the flame shape normalized by the burner diameter was independent of the burner diameter. Scalar profiles in microgravity were found to extend further in the radial direction as compared to those in normal gravity. The radial expansion was greater for flames with higher jet exit Reynolds numbers.

Two pre-existing analytical models for axisymmetric diffusion flames in the far-field of the jet-exit were considered. One model was based on the similarity analysis, while the other model provided a closed-form solution. These models were found to be inapplicable in context of this research, in part, because of the low Reynolds numbers used in experiments. The models, however, predicted correct qualitative trends of the flame shape.

Transitional flames were investigated to show the effect of Reynolds number and fuel dilution by helium. Scalar profiles were obtained in the near burner laminar portion of the transitional flame. Both in normal and microgravity, the axial plane where the laminar flame became transitional moved upstream as the Reynolds number was increased. The transition was delayed in microgravity, and adding helium to the fuel delayed transition in both normal and microgravity.

Chapter 1

INTRODUCTION

1.1 Background

This chapter provides a brief overview of diffusion flames, including their importance and utility in our everyday life, as well as some safety aspects associated with such flames. In order to place the current research in proper perspective, the chapter also includes a review of the past research associated with buoyancy effects on laminar and transitional gas-jet diffusion flames.

1.1.1 Diffusion Flames

Flames can be subdivided into two main categories; premixed flames, also called deflagration wave flames, and nonpremixed or diffusion flames. In a premixed flame, the fuel and oxidizer are mixed prior to combustion and hence, the burning rate is controlled primarily by the chemical kinetics. Premixed flames are propagatory, and move at a definite velocity through the mixture. Further discussion on premixed flames can be found in Linan and Williams (1993).

In diffusion flames, the fuel and oxidizer are brought together in the combustion zone through diffusion and convection and hence, these flames are controlled by the mixing process. An important difference between premixed and diffusion flames is that in premixed flames, the fuel-oxidizer ratio is spatially uniform in the mixture, while the ratio varies in diffusion flames. In addition, diffusion flames are not propagatory, and as such, they are not explosive. Diffusion flames, however,

are important in our everyday life because they occur in fires and most practical combustion systems, such as gas turbine engines, industrial furnaces, diesel engines, domestic appliances, etc. Understanding their driving mechanisms, therefore, can help avoid hostile fire hazards and poor application designs that cause pollution through emissions of toxic products which are harmful to the environment. Realizing their practical importance, combustion researchers, therefore, study diffusion flames to understand their complex driving mechanisms.

In as early as 1928, Burke and Schumann studied diffusion flames analytically and by using photographic techniques and gas-sampling probes. In their analysis, Burke and Schumann considered an axisymmetric fuel jet injected vertically into an oxidizing environment, co-flowing at the same velocity. Assuming constant density and transport properties, they isolated the influence of chemical reactions on the mixing process, allowing them to decouple the energy conservation equation from the other governing equations. Also, by assuming a uniform velocity field, they obtained a closed form solution of the mass diffusion equation. They obtained the flame structure and the radial concentration profiles of the fuel and oxidizer for both the over-ventilated and under-ventilated flames. They compared their results with probe measurements and obtained fairly good agreement, despite the severe assumptions imposed on the governing equations.

Following Burke and Schumann, other investigators developed different models for gas-jet diffusion flames with less restrictive assumptions. For example, Fay (1954) relaxed the uniform velocity and constant density assumptions. He included the axial momentum equation and simplified the analysis by assuming

boundary layer flow and unity Schmidt number. He obtained approximate solutions for the velocity and species concentrations profiles. Haggard and Cochran (1972) relaxed the unity Schmidt number assumption to obtain a closed form solution for the concentration profiles by assuming a small radial velocity. Their model, therefore, was not applicable far from the burner tip, where the radial velocity becomes significant. Following Haggard and Cochran, Spalding (1979) presented a model assuming a uniform jet-exit velocity. He incorporated the concept of Simple Chemically-Reacting System (SCRS) to introduce the mixture fraction (the fraction of the mass originated from the fuel stream) as a conserved scalar. Based on similarity, he obtained a closed-form solution for the mixture fraction. This model allowed for non-unity Schmidt numbers, but assumed constant density and transport properties.

Little analytical advancement occurred after the work of Spalding (1979) because of the complex physio-chemical interactions present in a reacting system that are manifested by highly non-linear terms in the governing equations, which make these equations formidable to solve analytically. For example, Savas and Gollahalli (1986) followed Squire's (1954) analysis to obtain a closed form solution for the species concentration field. Although the analysis included pressure variation and axial diffusion, it was based on constant density and transport properties. Because of such limitations of analytical models, and with advancements in computational power, numerical techniques have been introduced in recent years to aid in the study of diffusion flames.

One of the early works in the numerical modeling of diffusion flames was conducted by Bilger (1976) using the conserved-scalar approach and equilibrium chemistry. In his model, Bilger solves for the mixture fraction, which is related to the temperature and species concentrations using chemical equilibrium. The assumption of equal mass diffusivities in this model resulted, in part, to discrepancies between predictions and measurements in a H_2/N_2 diffusion flame system because hydrogen diffuses considerably faster than nitrogen.

Another numerical work was done by Miller and Kee (1977), who investigated the structure of H_2/N_2 flames burning in air. They included finite rate chemistry and variable transport properties. Due to the high diffusivity of hydrogen, they found that the parabolic flow model was not adequate. They also studied finite chemistry and buoyancy effects and found that the absence of buoyancy resulted in bigger flames. Another numerical work on diffusion flames was done by Laskey et al. (1989), who studied unsteady, laminar hydrogen-nitrogen diffusion flames and successfully predicted the flickering of these flames at a frequency of 12 Hz.

Shenoy et al. (1998) conducted a study to evaluate computations of non-reacting and reacting flows in axisymmetric flames by using the rainbow schlieren deflectometry. By comparing scalar profiles, they showed that the rainbow schlieren deflectometry was effective in evaluating the physical models used in flow computations. Shenoy (1998) also conducted a numerical study on the effect of preferential diffusion and buoyancy in hydrogen gas-jet diffusion flames. He found that the transport properties played an important role in determining the flame structure. He also found considerable deviations between the computational flame

structure when using non-unity and unity Lewis numbers. In particular, he found that the flame temperature at non-unity Lewis numbers to be higher near the base and lower near the flame tip than they were at unity Lewis number. Shenoy (1998) also showed that flames in low gravity were wider and taller than they were in normal gravity.

Examples of past and recent computational studies of gas-jet diffusion flames are too numerous to cover in a short review. However, it is inspiring to say that the Computational Fluid Dynamics (CFD) has become an essential part of the tools needed to study reacting flows.

1.1.2 Buoyancy Effects on Laminar Diffusion Flames

Despite the recent advancements in computational and experimental techniques, combustion researchers still face difficulties in studying the fundamental mechanisms in diffusion flames. The difficulties are caused, in part, by the coupled effects of diffusion and buoyancy in the mixing processes in these flames. Buoyancy-induced acceleration in a reacting system, especially in flows at low Froude numbers, obscures other mixing processes in the system. In addition, buoyancy forces in the governing equations make it difficult to obtain analytical solutions. In fact, all of the theoretical models discussed in the previous section neglected buoyancy. For this reason, many researchers investigated diffusion flames in microgravity to isolate the effects of buoyancy on the mixing mechanisms. Cochran and Masica (1971), for example, conducted microgravity experiments on laminar gas-jet diffusion flames at the NASA Lewis Research Center's 2.2-second drop tower facility. They used

photographic techniques to visualize methane flames. They observed that low Reynolds number (about 50) flames experienced a decrease in length immediately after the drop commenced. Thereafter, the flame continued to expand in both the radial and axial directions until it appeared to extinguish. They observed the flame color changing from yellow at normal gravity to orange in microgravity and dark orange before appearing to extinguish. At higher Reynolds numbers (up to 350), the flames reached a steady-state configuration, radiated more, and appeared more yellow during the drop period, suggesting greater accumulation of hot products near the reaction zone because of the lack of buoyancy driven convective transport. These experiments indicated that certain flow conditions are necessary to establish a steady-state diffusion flame in the microgravity drop tower facility.

Haggard and Cochran (1972) conducted another experimental investigation at the same facility to photographically obtain shapes of laminar ethylene and propylene diffusion flames. They found that flame lengths in microgravity were longer or shorter depending on whether ethylene (lighter than air) or propylene (heavier than air) was used. They obtained a correlation for the flame length that agreed reasonably well with their analytical predictions, despite the simplifying assumptions of constant fluid properties and boundary layer flow. They suggested that combustion in microgravity diffusion flames might not be proceeding at the stoichiometric reaction rate because of the accumulation of soot within the reaction zone, i.e., the reaction zone was of finite volume in microgravity, as opposed to a thin flame sheet in normal gravity.

Edelman et al. (1973) conducted similar experiments to obtain shapes of laminar methane and propylene flames. They compared their experimental results with predictions of a numerical model incorporating diffusion, viscous and gravity forces, and shifting equilibrium chemistry. The model predictions agreed well with normal gravity experiments. However, predictions at low Reynolds numbers in microgravity showed wider flames than experimentally observed, suggesting a lack of steady-state in the experimental flame. Edelman et al. (1973) identified the effects of several important parameters controlling the flame structure, including the variable transport properties and axial diffusion. They reasoned that chemical kinetics effects were responsible for the discrepancy between analytical and experimental results in microgravity.

Haggard (1981) conducted experiments on methane flames in microgravity to determine that air co-flow at a low velocity was adequate to sustain the flame in microgravity. Thereafter, Edelman and Bahadori (1986) assessed the existing data on microgravity diffusion flames. They concluded that the test time limitations and the lack of quantitative data prevent making definitive conclusions on the behavior of diffusion flames in microgravity environment. They explained that longer test times would eliminate the uncertainty in achieving steady-state condition in microgravity. Edelman and Bahadori (1986) also conducted negative gravity experiments using an inverted flame, in which they observed a spread-out of the flame tip resulting in a concave flame surface. They predicted this behavior using the model developed by Edelman et al. (1973), which showed a stagnation point at the centerline causing unattached flow recirculation. In addition, they developed a time-dependent elliptic

numerical model, assuming constant transport properties and neglecting buoyancy to compare with the transient experimental results of Cochran (1972). The model predictions of the flame height compared well with the experimental results in microgravity.

Experimental studies in drop towers have continued despite the uncertainty associated with the limited microgravity time available. For example, Bahadori et al. (1990) investigated ignition and its effects on color and luminosity of laminar diffusion flames of methane and propane in microgravity. Using improved photography and different ignition procedures, they found that flames previously thought to have extinguished in microgravity were still burning. In addition, they found that some of the flames thought to be transient or extinguished in previous microgravity experiments reached steady-state when ignited in microgravity. Also, they found that the flicker in normal gravity flames ceased in microgravity, suggesting that the flicker was caused by buoyancy. Finally, they applied a numerical model to achieve satisfactory agreement between predicted and observed height of flames that reached near steady-state in microgravity.

In 1993, Bahadori et al. obtained point measurements of temperature and species concentrations and investigated the effects of ambient pressure and oxygen concentration on flame characteristics, such as radiation. The experiments were conducted in the 2.2-second and 5.18-second drop towers. They reported that the radiation loss in microgravity laminar flames was up to an order of magnitude higher than that in normal gravity flames. Thus, the temperature in microgravity flames was lower. In addition, they found that the time to reach near steady-state in microgravity

flames was up to an order of magnitude longer than that in normal gravity flames. They also found that the effects of ambient pressure and oxygen concentration were more significant in microgravity than those in normal gravity. For example, a large increase in soot formation occurred in microgravity flames at high oxygen concentration. Bahadori et al. (1993) applied a comprehensive, two-dimensional, steady-state numerical model incorporating inertia, viscosity, multi-component diffusion, gravity, combustion, and radiation. They predicted that the buoyancy effects were negligible at 10^{-4} g, and that the tip of the microgravity flame was almost stagnant because of lack of the buoyant acceleration. A comparison between predicted and measured flame heights resulted in fairly good agreement.

Microgravity experiments on diffusion flames continued with the study of Sunderland et al. (1994), who experimentally and numerically studied soot properties of ethylene and propane laminar microgravity flames at various pressures and fuel flow rates. They used a numerical model assuming steady-state, axisymmetric flow, and unity Lewis to predict residence times for the nonbuoyant flames. They observed that in microgravity, laminar point luminosity lengths varied little with the burner diameter. The microgravity flames were up to four times smaller than the buoyant flames at comparable conditions. In addition, they predicted that laminar smoke point residence times were longer in microgravity flames than those in normal gravity flames because of the differences in soot paths and velocity distributions along soot paths.

In all of the studies reviewed above, the measurements in microgravity were mostly qualitative with the exception of limited point measurements of temperature,

species concentrations, and global flame radiation by Bahadori et al. (1993). Recently, Silver et al. (1995) attempted and successfully measured H₂O concentration profiles at various heights above the burner in a microgravity laminar methane flame using diode-laser wavelength modulation spectroscopy. They found that the flame expanded significantly in size, and appeared to stabilize rapidly upon entering the microgravity condition. They reported that mass diffusion rates in microgravity were small as compared to those in normal gravity, which is consistent with the findings of Hegde et al. (1994).

Tittmann et al. (1996) studied laminar hydrogen gas-jet diffusion flames using the drop tower facility in Bremen, Germany. Because they used a video camera for visualization, they employed sodium chloride to artificially color the flame. In their experiment, flames continued to increase in size throughout the 4.7-second drop, suggesting that steady-state microgravity conditions were not established. They observed a decrease in the brightness of the flame during the drop, which prompted them to suggest a lower flame temperature in microgravity. Tittmann, et al. (1998) continued their experimental study of hydrogen gas-jet diffusion flames using microthermocouples to measure the temperature profiles and solid electrolyte sensors to measure the oxygen concentration profiles. The flame investigated was flickering in normal gravity but not in microgravity. They used the oxygen profiles to obtain flame contours in normal and microgravity. The flame in microgravity was bigger than that in normal gravity. Moreover, the temperature gradients were smaller in microgravity than those in normal gravity.

Sunderland et al. (1999) conducted experiments to measure shapes of methane, ethane, and propane gas-jet diffusion flames burning in quiescent air in normal and microgravity. They included effects of pressure, burner diameter, and fuel flow rate. They found that the flame length was not affected by pressure in microgravity, but it increased slightly with decreasing pressure in normal gravity. They also found that the flame height at low Reynolds numbers was, on average, 40 % larger in microgravity than that in normal gravity. The difference between flame height in normal and microgravity decreased with increasing Reynolds numbers. Finally, they found that the normal gravity flame width correlated with the Froude number. At large Froude numbers, the flame width approached the non-buoyant limit.

Lin et al. (1999) studied laminar gas-jet diffusion flames of ethylene and propane on-board the space shuttle Columbia. They measured flame shapes at various ambient pressures, and observed typical closed-tip and opened-tip configurations at fuel flow rates smaller and larger, respectively, than those at laminar smoke point. Using the simplified theoretical model of Spalding (1979), they obtained good agreement between measured and predicted flame shapes with closed-tip configurations.

Recently, Agrawal et al. (1999) conducted experiments on hydrogen gas-jet diffusion flames in a variable pressure combustion chamber using the rainbow schlieren deflectometry. In addition, they conducted microgravity experiments in the 2.2-s drop tower. They correlated the flame width in normal gravity (at different pressures) with that in microgravity using the normalized Froude number at the fuel

jet exit as a parameter. At low pressures in normal gravity, they obtained nonbuoyant flames that remained parallel to the fuel burner regardless of the orientation of the burner with respect to the gravitational vector.

1.1.3 Buoyancy Effects on Transitional Diffusion Flames

The studies discussed in the previous section concentrated on laminar diffusion flames, with the exception of Bahadori et al. (1993), who extended their investigation to include the transitional and turbulent diffusion flames. These flames are more common in practice than the laminar diffusion flames. Study of the transitional and turbulent flames is complicated because of the simultaneous presence of large scale structures associated with large eddies and Kolmogorov microscale structures. Transitional and turbulent diffusion flames have been investigated extensively for many years (Bray, 1996). Hawthorne et al. (1949) measured the visible length of turbulent gas-jet diffusion flames and identified that turbulent mixing was the controlling process in such flames; a presumption that was later described by Spalding (1971) in his “mixed-is-burned” hypothesis. With recent advances in computational power, numerical simulations have emerged as effective techniques to study of transitional and turbulent diffusion flames. Many flow models, such as the k - ϵ turbulence model and the Reynolds stress model have evolved to simulate turbulent reacting flows. Furthermore, direct numerical simulations (DNS) and large eddy simulations (LES) are now used increasingly for turbulent flow predictions.

The buoyancy present in normal gravity complicates transitional and turbulent flows and hence, microgravity experiments on such flames are of significant interest. However, only a few attempts have been made to conduct experiments on transitional/turbulent flames in microgravity. Bahadori et al. (1993) observed that the transition in microgravity initiated with the appearance of disturbances that formed near the flame base and convected downstream. In contrast, the transition in normal gravity initiated near the flame tip and the transition point moved upstream toward the flame base with increasing Reynolds number. Because the buoyancy-driven acceleration is absent in microgravity, they explained, the transition to turbulence might occur over a wider range of Reynolds numbers. Further, they added, it was possible that the flame might blow off at a Reynolds number higher than that in normal gravity.

Another study on transitional gas-jet diffusion flames in microgravity environment was conducted by Hegde et al. (1994). They observed similar qualitative features using propane, propylene, and methane fuels. The microgravity flames were laminar for Reynolds numbers up to 2000. At Reynolds numbers above 2040, large-scale structures originated at the flame base and convected downstream, with increasing frequency as the Reynolds number was increased. Noting that transition to turbulence in pipes occurs at a Reynolds number of about 2300, they argued that the flame transition in microgravity might be caused by turbulent fluctuations in the fuel line. They observed that the transition in microgravity affected the entire flame, as opposed to the normal gravity transition that affected the tip and upper regions of the flame. They also observed a reduction in the flame tip

opening when the intermittent disturbances arrived, and that the flame tip sustained closing when a continuous train of disturbances was present. In addition, the normal gravity luminous flame height was constant at Reynolds numbers greater than 3500, whereas the microgravity flame height was increasing. The normal gravity flame blew off at a Reynolds number of about 5800, while the microgravity flame was still burning. Finally, Hegde et al. (1994) argued that the diffusion rates in microgravity were three times higher than they are in normal gravity.

Recently, Agrawal et al. (1998) conducted a study on transition in burning and nonburning hydrogen gas jets in normal and microgravity. They found that buoyancy affected the transition in flames but not in cold jets. They explained that the buoyancy-driven acceleration in normal gravity destabilizes the jet flow, which promotes transition to turbulence by fuel jet instabilities.

1.2 Objectives and Scope of the Present Study

The majority of the experimental studies conducted so far on diffusion flames in microgravity involve qualitative measurements using photographic techniques. Only limited quantitative measurements, e.g. by Bahadori et al. (1993) and Silver et al. (1995) have been attempted. Further, mostly hydrocarbon fuels have been used, with the exception of Tittmann et al. (1996, 1998) and Agrawal et al. (1998, 1999). Hydrocarbon fuels exhibit soot formation and associated radiative heat losses, which increase the complexity of analysis. Further, only a limited number of local temperature measurements were obtained which is inadequate to validate predictions by the various theoretical models that have been proposed. Therefore, it is beneficial

to investigate non-sooting hydrogen gas-jet diffusion flames in microgravity, and to obtain temperature and species concentration fields. Such measurements will advance our understanding of the various physio-chemical mechanisms and their interactions in diffusion flames. The measurements will also serve as part of a comprehensive data base on combustion processes that are not dominated by buoyancy effects.

The overall objective of this study, therefore, is to conduct quantitative scalar measurements in hydrogen gas-jet diffusion flames in normal and microgravity, and to analyze the resulting data. The non-intrusive, line-of-sight, quantitative Rainbow Schlieren Deflectometry (RSD) technique was advanced to measure the temperature and species mole fraction profiles in the flame across the field of view. The RSD measurements in normal gravity flame were validated by comparing with probe measurements. Once validated, the RSD technique was used to investigate buoyancy effects in laminar and transitional hydrogen gas-jet diffusion flames. The laminar flame experiments were conducted to study how the jet exit Reynolds number and fuel burner diameter affected the temporal evolution of the flame during transition to microgravity, flame shape, and scalar profiles in normal and microgravity. The collected data were analyzed and used to evaluate predictions by an existing theory of gas-jet diffusion flames. Experiments with transitional diffusion flames were conducted in normal and microgravity to measure scalar profiles in the laminar portion of the flame near the burner exit. In addition, the effect of buoyancy on flame transition was investigated by varying the jet exit Reynolds number and diluent (helium) in the fuel.

Chapter 2

APPLICATION OF EXISTING THEORY

In this chapter, two analytical models for gas-jet diffusion flames in microgravity are presented. The first model (model I), due to Spalding (1979), allows similarity solution, whereas the second model (model II), due to Savas and Gollahalli (1986), has an exact solution. Simple analytical expressions will be given to show linear dependence of the flame height on Reynolds number and burner diameter.

Models I and II will be compared to show their applicability in the context of this research. It should be noted, however, that both models are not expected to hold quantitatively because of the constant-property assumption. Nevertheless, it is helpful to compare theory with the measurements to evaluate the effect of the constant-property assumption on predictions. Further, the theories are expected to be valid qualitatively, so that the effect of Schmidt number, axial diffusion, and Reynolds number on diffusion flames can be investigated. Also, it should be noted that one can curve-fit the experimental data based on theory for a given Reynolds number and apply the resulting equations for prediction at other Reynolds numbers. Lin et al. (1999) used this approach with Spalding's (1979) similarity solution to predict shapes of ethylene and propane gas-jet diffusion flames in microgravity at Reynolds numbers of 45 to 200. Their predictions were in good agreement with measurements except for the open-tip flame configuration. Following Lin et al. (1999), a curve-fit of flame shape based on model II will be obtained in this study, and used to predict the oxygen mole fraction and temperature profiles at a given

Reynolds number. A brief overview of analytical models for gas-jet diffusion flames in normal gravity will also be presented in this chapter.

2.1 Diffusion Flames in Microgravity

In this section, the two models of gas-jet diffusion flames in microgravity are presented.

2.1.1 Model I

Consider an axisymmetric burner with a gas jet discharging into still atmosphere (Fig. 2.1). Assume the following:

1. Steady-state
2. Uniform pressure
3. Negligible buoyancy
4. Boundary layer flow
5. Constant gas properties
6. Uniform jet-exit velocity

The mass and momentum conservation equations are written as follows

(Goldstein, 1938):

$$\frac{\partial u}{\partial z} + \frac{\partial v}{\partial r} + \frac{v}{r} = 0 \quad (2.1)$$

$$u \frac{\partial u}{\partial z} + v \frac{\partial u}{\partial r} = \frac{v}{r} \frac{\partial}{\partial r} \left(r \frac{\partial u}{\partial r} \right) \quad (2.2)$$

with boundary conditions:

$$\begin{aligned}
r = 0 : \quad v &= 0 \\
&\frac{\partial u}{\partial r} = 0
\end{aligned} \tag{2.3a}$$

$$r \rightarrow \infty : \quad u = 0 \tag{2.3b}$$

Goldstein (1938) obtained the following similarity solutions that satisfy equations (2.1) and (2.2) and boundary conditions (equation 2.3):

$$\frac{u}{u_0} = \frac{3}{32} \left(\frac{\text{Re}_T \cdot d}{z} \right) \left(1 + \frac{1}{4} \xi^2 \right)^{-2} \left(\frac{\rho_0}{\rho_\infty} \right)^{\frac{1}{2}} \tag{2.4}$$

$$\frac{v}{u_0} = \frac{\sqrt{3}}{8} \frac{d}{z} \left(\xi - \frac{1}{4} \xi^3 \right) \left(1 + \frac{1}{4} \xi^2 \right)^{-2} \left(\frac{\rho_0}{\rho_\infty} \right)^{\frac{1}{2}} \tag{2.5}$$

where the similarity variable, ξ is given by

$$\xi = \frac{\sqrt{3}}{8} \frac{r}{z} \text{Re}_T$$

and

$$\text{Re}_T = \frac{u_0 d}{\nu_\infty} \sqrt{\frac{\rho_0}{\rho_\infty}}$$

Note that the theoretical Reynolds number, Re_T , is consistent with definitions of Squire (1950) and Savas and Gollahalli (1986). The above solutions do not satisfy the boundary condition at the jet exit i.e., $u = u_0$. Instead, the exit conditions are satisfied in an integral sense through invariance of the axial momentum flux.

Spalding (1979) extended Goldstein's (1938) analysis to the diffusion flame by assuming a Simple Chemically-Reacting System (SCRS). Accordingly, he obtained the following conservation equation for the mixture fraction, f , defined as the fraction of the mass originated from the fuel stream:

$$u \frac{\partial f}{\partial x} + v \frac{\partial f}{\partial r} = \frac{D}{r} \frac{\partial}{\partial r} \left(r \frac{\partial f}{\partial r} \right) \quad (2.6)$$

with boundary conditions:

$$r = 0 : \quad \frac{\partial f}{\partial r} = 0 \quad (2.7a)$$

$$r \rightarrow \infty : \quad f = 0 \quad (2.7b)$$

For unity Schmidt number i.e., $D = \nu$, Spalding (1979) obtained the following similarity solution for the mixture fraction:

$$f = \frac{3}{32} \left(\frac{Re \cdot d}{z} \right) \left(1 + \frac{1}{4} \xi^2 \right)^{-2} \quad (2.8)$$

Here, $Re = \frac{u_o d}{\nu_o}$. Note that Spalding assumed that the jet properties were the

same as those of the surroundings i.e., $Re_T = Re$. Spalding's (1979) analysis is extended (Appendix A) for non-unity Schmidt numbers (Parthasarathy and Emanuel, 1998) to obtain the following similarity solution:

$$f = \frac{2Sc + 1}{32} \left(\frac{Re_T \cdot d}{z} \right) \left(1 + \frac{1}{4} \xi^2 \right)^{-2Sc} \left(\frac{\rho_o}{\rho_\infty} \right)^{\frac{1}{2}} \quad (2.9)$$

Here, the density ratio factor appears because Re_T is used instead of Re . Equation (2.9) is rearranged to obtain the flame surface represented by the stoichiometric mixture fraction.

$$\frac{r_{flame}}{d} = \frac{16}{\sqrt{3}} \frac{z}{Re_T d} \sqrt{\left(\frac{(2Sc + 1) Re_T \cdot d}{32 z f_{st}} \left(\frac{\rho_o}{\rho_\infty} \right)^{\frac{1}{2}} \right)^{\frac{1}{2Sc}} - 1} \quad (2.10)$$

The flame height is obtained by setting the flame width to zero.

$$\frac{z_{\text{flame}}}{d} = \frac{(2Sc + 1)Re_T}{32f_{st}} \left(\frac{\rho_o}{\rho_\infty} \right)^{\frac{1}{2}} \quad (2.11)$$

In agreement with the analysis and experiments in microgravity by Haggard and Cochran (1972), equation (2.11) shows a linear dependence of flame height on Reynolds number. Equation (2.11) also shows that the flame height normalized by the burner diameter is independent of the diameter for a given Reynolds number.

Differentiating equation (2.10) with respect to z , and setting the result to zero, one obtains the maximum flame width

$$\frac{r_{\text{flame, max}}}{d} = \frac{(2Sc + 1)(4Sc - 1)^{2Sc-1/2}}{2\sqrt{3}f_{st}(4Sc)^{2Sc}} \left(\frac{\rho_o}{\rho_\infty} \right)^{\frac{1}{2}} \quad (2.12)$$

Thus, the maximum flame width is independent of the Reynolds number, and when normalized by the burner diameter, it is independent of the diameter for a given Reynolds number.

2.1.2 Model II

Relaxing the axial diffusion and constant pressure assumptions in the above formulation by Goldstein (1938), Squire (1950) obtained a closed-form analytical solution for velocity and temperature fields in spherical and cylindrical coordinates. Savas and Gollahalli (1986) used Squire's analysis to obtain a closed-form analytical solution for the molar concentration field created by a point source. Note that Squire assume that the momentum is introduced into the flow field with no mass flux.

Following Squire (1950) and Savas and Gollahalli (1986), and using Spalding's SCRS model, it can be shown that the closed-form analytical solution for the mixture fraction is given as follows:

$$f = \frac{\text{Re}_T d}{32\sqrt{r^2 + z^2}} \frac{b}{\left(1 + a - \frac{z}{\sqrt{r^2 + z^2}}\right)^{2\text{Sc}}} \left(\frac{\rho_o}{\rho_\infty}\right)^{\frac{1}{2}} \quad (2.13)$$

where a and b are given, respectively by

$$\text{Re}_T^2 = 32 \left[\frac{8(a+1)}{3a(a+2)} + (a+1)^2 \ln\left(\frac{a}{a+2}\right) + 2(a+1) \right] \quad (2.14)$$

and

$$b = \frac{4\text{Sc}^2 - 1}{(2\text{Sc} + a + 1)(a + 2)^{-2\text{Sc}} + (2\text{Sc} - a - 1)a^{-2\text{Sc}}} \quad (2.15)$$

Again, the flame height is given by setting $r = 0$ in equation (2.13). Hence,

$$\frac{z_{\text{flame}}}{d} = \frac{\text{Re}_T b}{32a^{2\text{Sc}} f_{\text{st}}} \left(\frac{\rho_o}{\rho_\infty}\right)^{\frac{1}{2}} \quad (2.16)$$

In part, it is the assumption of negligible axial diffusion in the axial momentum and species conservation equations that allows the similarity solution. At a large Reynolds number, the axial diffusion is negligible and hence, the similarity solution (model I) must approach the exact solution (model II) regardless of the location above the burner. Nevertheless, both theories are invalid near the burner because of the singularity at the burner exit. Note that equation (2.16) breaks down for small Re_T because the coefficient $\frac{b}{a^{2\text{Sc}}}$ (flame height coefficient) in equation (2.16) varies significantly with Re_T , as shown in Fig. 2.2. The flame height

coefficient must be constant to obtain the known linear dependence of flame height on Reynolds number. Figure 2.2 shows that this condition is satisfied at Re_T greater than 100 for $Sc = 0.2$.

Fig. 2.3 compares the radial distribution of the mixture fraction from model I and model II at $z/d = 10$ for $d = 1.19$ mm, $Re_T = 500$, and $Sc = 0.7$. The two profiles are practically identical. Fig. 2.4 shows the mixture fraction profiles for $Re_T = 100$. The two profiles are still practically the same. For hydrogen, however, the Schmidt number is 0.2 (Savas and Gollahalli, 1986), so that the mass diffusion is considerably larger than the momentum diffusion. Figure 2.5 compares the radial distribution of the mixture fraction from model I and model II at $z/d = 10$ for $d = 1.19$ mm, $Re = 500$, and $Sc = 0.2$. Here, the two profiles are still matching. Note that the profiles have diffused further in the radial direction compared to the case with $Sc = 0.7$. At $Re = 100$, the difference between the two profiles becomes evident as shown in Fig. 2.6. Model I underestimated the mixture fraction at and near the center because of the assumption of negligible axial diffusion. However, the conservation of mass requires that the radial integral of the mixture fraction be the same for both models, which is satisfied for sufficiently large r/d . Strictly speaking, however, both models are not applicable in the context of this research because the jet-exit Reynolds numbers used in experiments (40 and 70) are small. For curve-fitting purposes, nevertheless, it is reasonable to use a model as a guide. Model II was chosen in this study to account for the high diffusivity of hydrogen.

2.2 Diffusion Flames in Normal Gravity

Because of the complex nature of the governing equations that result with the addition of buoyancy, few theoretical models providing closed form solution of gas-jet diffusion flames in normal gravity exist. For example, Hegde and Bahadori (1992) developed a simplified analytical model of the Burke-Schumann flame including buoyancy. The model assumed steady-state, unity Lewis number, constant properties, one-step chemical reactions, and negligible viscous effects. The model predicted that the flame height was independent of gravity. Such an independence was shown analytically by Roper (1977) and experimentally by Stoker (1990). Roper (1977) modified the Burke and Schumann theory by including the effects of gravity. He found a linear dependence of flame height on Reynolds number in normal gravity, as was shown experimentally by Cochran and Masica (1971).

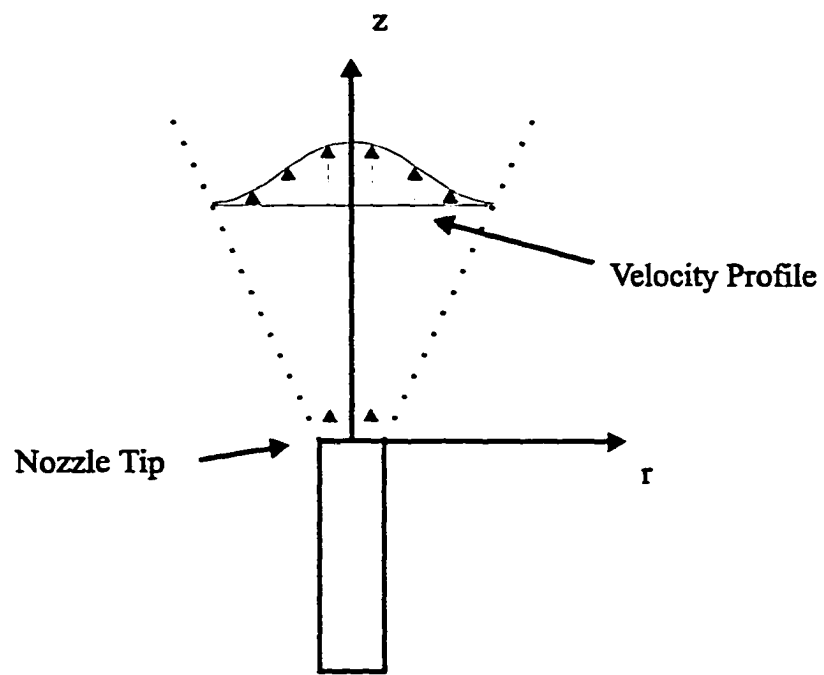


Figure 2.1: An axisymmetric jet

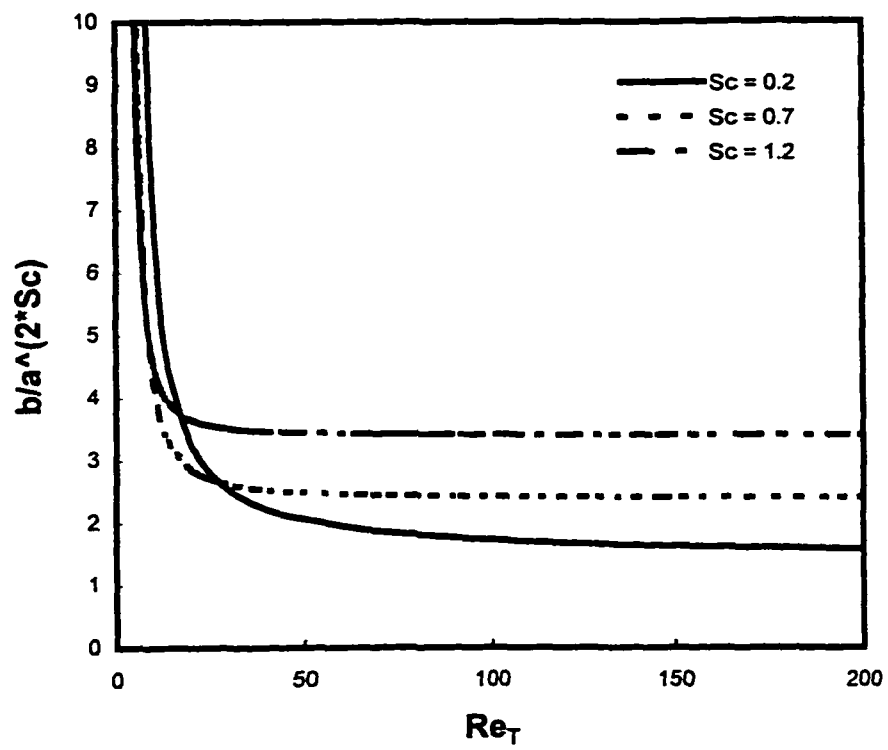


Figure 2.2: Flame height coefficient as a function of Reynolds number

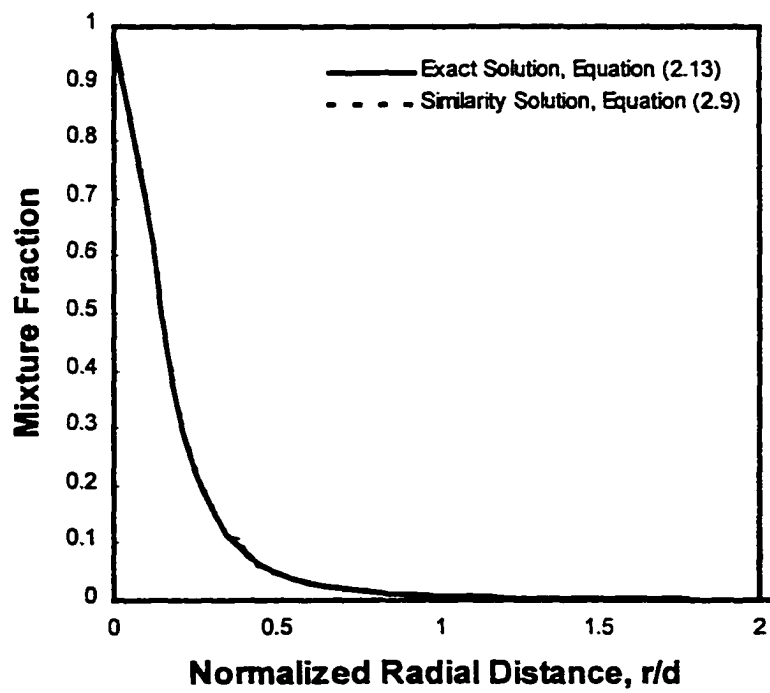


Figure 2.3: Mixture fraction distribution: $Re_T = 500$, $Sc = 0.7$, $d = 1.19$ mm, and $z/d = 10$

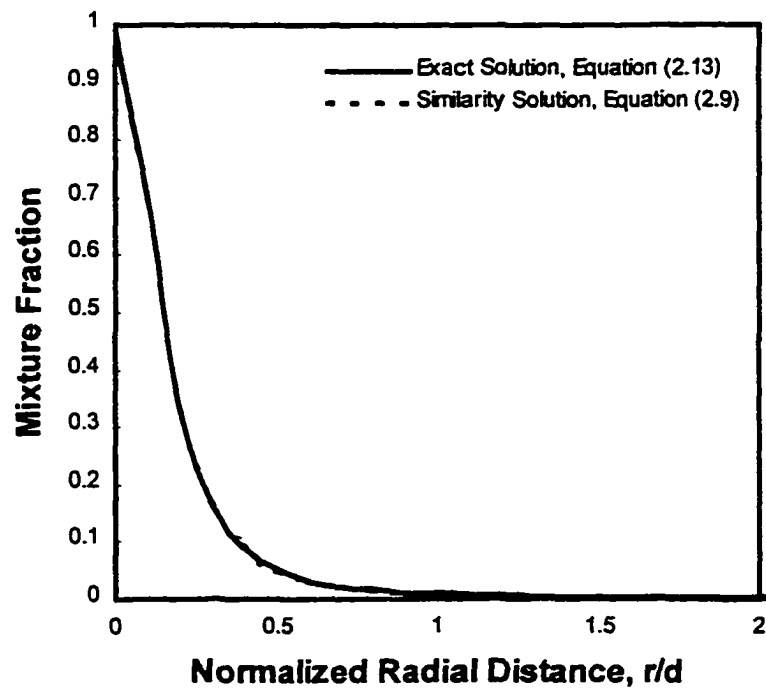


Figure 2.4: Mixture fraction distribution: $Re_T = 100$, $Sc = 0.7$, $d = 1.19$ mm, and $z/d = 2$

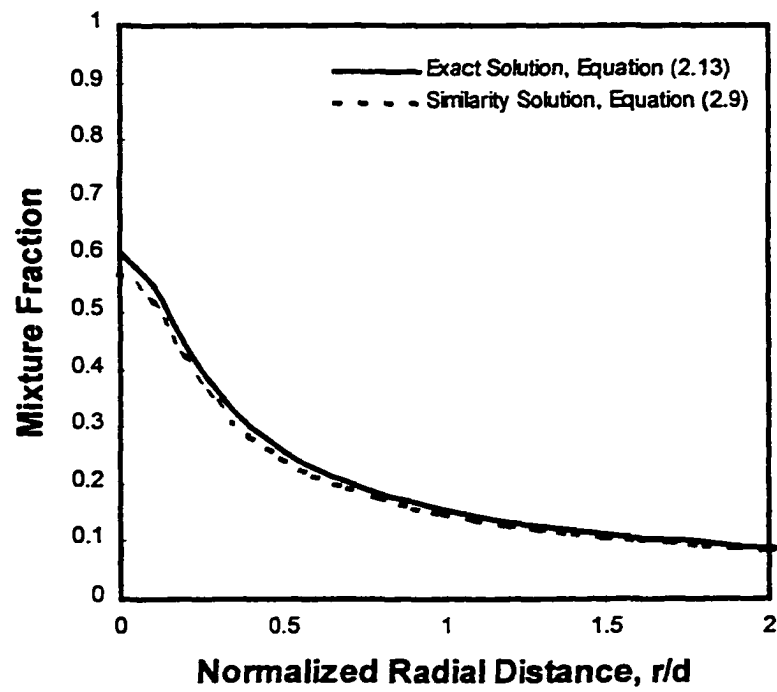


Figure 2.5: Mixture fraction distribution: $Re_T = 500$, $Sc = 0.2$, $d = 1.19$ mm, and $z/d = 10$

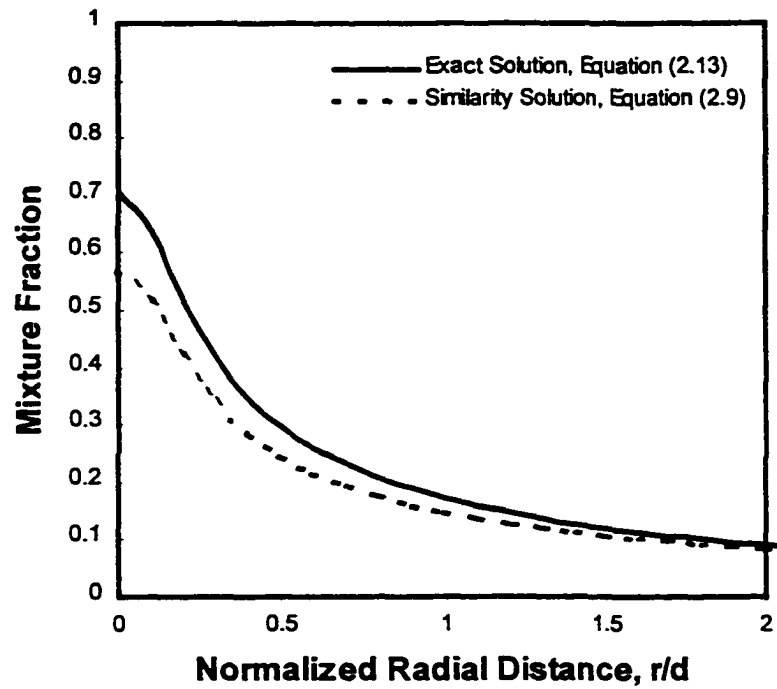


Figure 2.6: Mixture fraction distribution: $Re_T=100$, $Sc=0.2$, $d = 1.19$ mm, and $z/d=2$

Chapter 3

EXPERIMENTAL SETUP AND PROCEDURE

In this chapter, the experimental setup and procedure are described, starting with details of the drop test rig, and continuing on to discuss the probe measurements and drop procedure.

3.1 Drop Test Rig

A drop test rig was designed and fabricated to conduct microgravity experiments at the NASA Lewis Research Center's 2.2-second drop tower. The drop test rig, Fig. 3.1, consisted of a standard aluminum frame, 840-mm high, 960-mm long, and 400-mm wide (Lekan et al., 1996). The frame housed the experimental setup, including the RSD apparatus, fuel supply and ignition systems, an electrical power system, data acquisition and control systems, a ruggedized computer. The experiment was integrated and controlled by an onboard computer. Thus, all switching and control commands during and after the drop were performed automatically.

In this section, the drop test rig components i.e., the RSD apparatus, fuel supply and ignition systems, data acquisition and control systems, and the power supply system are described.

3.1.1 Rainbow Schlieren Deflectometry

Combustion diagnostics range from the conventional thermocouple and gas sampling probes to high resolution, optics-based techniques (Fristrom, 1995 and Eckbreth, 1996). Thermocouples and gas sampling probes are intrusive, and therefore, they introduce flow disturbances that are difficult to quantify. In addition, they have poor spatial and temporal resolutions compared to the optics-based techniques, which are non-intrusive. The optics-based techniques may be classified as either local or line-of-sight. Local measurement techniques include laser Doppler velocimetry (LDV), particle image velocimetry (PIV), Rayleigh scattering and laser-induced fluorescence (LIF). These techniques often require powerful lasers and highly stable environment to ensure optical alignment. Line-of-sight techniques include methods based on changes in the refractive index of the medium. Such techniques include shadowgraphy, schlieren deflectometry, and interferometry (Goldstein and Kuehn, 1996).

The Rainbow Schlieren Deflectometry (Howes, 1984) is a line-of-sight technique to measure refractive index of the medium, which is related to other scalar flow properties. Recently, a quantitative RSD technique utilizing digital imaging was developed by Greenberg et al. (1995). This technique was successfully applied by Al Ammar et al. (1998) to measure oxygen mole fraction in a laminar, isothermal helium jet discharged vertically into air, and by Agrawal et al. (1998) to measure temperature distribution in an asymmetric heated air jet.

One of the objectives of this research is to obtain quantitative scalar measurements in hydrogen gas-jet diffusion flames. This was accomplished by

advancing and validating the quantitative RSD technique. The technique was applied to a reacting flow by relating the refractive index to other scalar properties of the flow field. Next, the RSD apparatus, analysis procedure, and state relationships to obtain the temperature and species mole fractions are described.

3.1.1.1 RSD Apparatus

The optical layout of the rainbow schlieren apparatus, mounted on a stainless steel breadboard, is shown in Fig. 3.2. A 5- μm wide, 3-mm high laser-machined source aperture is placed at the focal plane of a 80-mm diameter, 310-mm focal length achromatic lens. A 600- μm diameter fiber optic cable connected to a 150-W halogen light source provides the light input to the aperture. The collimated light rays pass through the test-section before decollimation by an 80-mm diameter, 1000-mm focal length achromatic lens. Because of the space constraints, a pair of 100-mm diameter, aluminum coated flat surface mirrors are used to fold the light rays by 180 degrees. The folded light rays form a displaced image of the source at the 2.5-mm wide, computer-generated, symmetric color filter placed at the focal plane of the decollimating lens. The filter was printed on a 35-mm color slide with a resolution of 115 pixels/mm, providing a total of 290 independent hues. A photograph of the filter is shown in Fig. 3.3. Note that the filter colors vary only in the transverse direction and hence, the filter is sensitive only to the transverse ray displacement. A 75-mm focal length camera lens is used to image the test section onto the CCD array of a digital camera. The real time images from the camera are acquired at 30 Hz by a 24-bit PCI bus frame grabber, installed in a Pentium 166 MHz computer.

3.1.1.2 Abel Inversion

The angular deflection of a light ray passing through an axisymmetric refractive index field (Fig. 3.4) is given for small deflections by the following relationship (Rubinstein and Greenberg, 1994):

$$\varepsilon(y) = 2y \int_y^{\infty} \frac{d\delta}{dr} \cdot \frac{dr}{\sqrt{(r^2 - y^2)}} \quad (3.1)$$

where $\delta = (n - 1)$ is the normalized refractive index difference and n is the refractive index normalized by that of the surroundings.

The angular ray deflection is transformed by the decollimating lens to a transverse displacement at the filter plane given by (Goldstein and Kuehn, 1996)

$$d(y) = \varepsilon(y) \cdot f \quad (3.2)$$

where f is the focal length of the decollimating lens (Fig. 3.5). The ray displacement is found from the filter transmissivity function given by the filter calibration curve shown in Fig. 3.6, where the hue at a traverse location was obtained by averaging hue in the corresponding color schlieren image without the test medium. Figure 3.6 also shows the standard deviation of hue at each transverse location. Note that the standard deviation is maximum at average hue of about 150 degrees. This hue value corresponded to the fuel-rich region in the RSD image. It will be shown later that the scalar measurements in the fuel-rich region are very sensitive to the measurement errors. Hence, a large standard deviation of hue in this region leads to large measurement uncertainties. One way to reduce the standard deviation of hue and hence, the measurement error is to employ a wider filter. However, this will reduce the sensitivity of the RSD system, resulting in poor signal-to-noise ratio everywhere.

Another way is to use reflective rather than refractive optics to avoid chromatic aberration. Chromatic aberration in the decollimating lens causes its focal length to vary slightly with wave length of the light rays. Hence, the source image does not focus exactly at the filter plane. The deviation is largest at a hue of about 150 degrees, where high standard deviation and non-linearity in the otherwise linear filter transmissivity function are observed (Fig. 3.6).

After calculating the angular deflections from Equation (3.2), the refractive index field is found by inverting Equation (3.1) using the Abel transformation (Rubinstein and Greenberg, 1994):

$$\delta(r) = -\frac{1}{\pi} \int_r^{\infty} \varepsilon(y) \cdot \frac{dy}{\sqrt{(y^2 - r^2)}} \quad (3.3)$$

Following Vasil'ev (1971), the integral in Equation (3.3) is split into a sum of integrals, factoring out the deflection angle. Thus,

$$\delta(r_i) = -\frac{1}{2\pi} \sum_{j=i}^N [\varepsilon_j + \varepsilon_{j+1}] \cdot \int_{r_j}^{r_{j+1}} \frac{dy}{\sqrt{(y^2 - r_i^2)}} \quad (3.4)$$

where $r_i = i\Delta r$ is the radial distance from the centerline, Δr is the sampling interval, and N is the total number of samples. Note that $\varepsilon(y)$ was approximated by linear interpolation although other schemes such as three-point Abel inversion (Dasch, 1992) have been used in the literature. The integration in Equation (3.4) is performed analytically. After some algebraic manipulation, the result is expressed as follows:

$$\delta(r_i) = \sum_{j=i}^N D_{ij} \cdot \varepsilon_j \quad (3.5)$$

where

$$\begin{aligned} D_{ij} &= J_{ij} & \text{if } j = i \\ &= J_{ij} + J_{i,j-1} & \text{if } j > i \end{aligned}$$

with

$$J_{ij} = -\frac{1}{2\pi} \cdot \ln \left[\frac{j+1 + [(j+1)^2 - i^2]^{1/2}}{j + (j^2 - i^2)^{1/2}} \right]$$

Equation (3.5) has the form similar to that of Dasch (1992) to invert path-integrated data from interferometric or absorption measurements. In this form, coefficients D_{ij} are independent of the sampling interval.

3.1.1.3 State Relationships

In a fast-reacting diffusion flame, the mixing process is described by a single conserved scalar, and the thermodynamic state can be described using the chemical equilibrium (Bilger, 1976). Assuming fast chemistry, the adiabatic flame temperature and species concentrations in a hydrogen-air reaction system are found from a single variable, namely, the mixture fraction, or the fraction of mass originated in the fuel stream. At chemical equilibrium, the temperature and species concentrations for a given mixture fraction can be found by minimizing the Gibb's free energy. The conditions at chemical equilibrium are stated as follows (Kuo, 1986):

$$\mu_j + \sum_{i=1}^I \lambda_i a_{ij} = 0, \quad j = 1, \dots, N \quad (3.6)$$

and

$$b_i - b_i^0 = 0, \quad i = 1, \dots, L \quad (3.7)$$

Here, μ_j is the chemical potential per kilogram-mole of species j , λ_i are Lagrange multipliers, a_{ij} is the number of kilogram-atoms of element i per kilogram-mole of species j , b_i is the number of kilogram-atoms of element i per kilogram of mixture, b_i^* is the assigned number of kilogram-atoms of element i per kilogram of total reactants, N is the number of chemical species, and L is the number of elements.

Assuming the ideal gas model, the chemical potential is written as follows (Kuo, 1986):

$$\mu_j = \mu_j^\circ + R_u T \ln\left(\frac{n_j^*}{n^*}\right) + R_u T \ln(p) \quad j = 1, \dots, N \quad (3.8)$$

where μ_j° is the chemical potential in the standard state, n_j^* is the number of kilogram-moles of species j per kilogram of mixture, R_u is the universal gas constant, T is the temperature, and p is the pressure in atmosphere.

By assigning the operative pressure and initial temperature of reactants, equations (3.6) and (3.7) are solved for a given mixture fraction to determine the equilibrium temperature and species concentrations. The equilibrium calculations were done by a computer code (Kee et al., 1993) with H_2 , H_2O , O_2 , N_2 , H , HO_2 , H_2O_2 , O , and OH taken as the combustion species.

Given the temperature and species concentrations at different mixture fractions, a table of normalized refractive index difference versus scalar variables was created using the following relation (Yates, 1993) :

$$n = 1 + \frac{P}{R_u T} \sum_i \kappa_i X_i M_i = \delta + 1 \quad (3.9)$$

where κ_i is the Dale-Gladstone constant of the i^{th} species, X_i is the species mole fraction, and M_i is the molecular weight of the species.

Figure 3.7 compares the temperature versus mixture fraction plot measured in the fuel-rich region in a counter flow arrangement at a strain rate of 490 s^{-1} (Wehrmeyer, et al., 1996) to that obtained from computation using chemical equilibrium. The chemical equilibrium calculations of temperature match with measurements, except at equivalence ratios between 6 and 28, where a discrepancy of up to 150 K is observed. Similar observations were made by Faeth, et al. (1986), who found that state relations for species concentrations follow chemical equilibrium in pure hydrogen/air diffusion flames, and that the temperature agrees with chemical equilibrium in the fuel-lean region. These results suggested that differential/preferential diffusion effects are absent in the fuel-lean region of a pure hydrogen /air diffusion flame, and that the preferential diffusion and/or incomplete chemical reactions may be important in some parts of the fuel-rich region. In flames where chemical equilibrium calculations do not approximate the state relations, experimentally obtained state relations (Sivathanu, et al., 1990, Wehrmeyer, et al., 1996, or Brown, et al., 1997) can be used to obtain scalar properties from schlieren measurements of the refractive index.

Fig. 3.8 shows a plot of equilibrium temperature versus normalized refractive index difference. Notice the steep gradient of temperature near the flame, which makes this region very sensitive to errors in measurement of the refractive index. The equilibrium oxygen mole fraction versus normalized refractive index difference is shown in Fig. 3.9. Again, the gradient of oxygen mole fraction near the flame is

steep. Thus, a small error in measurement of the refractive index in this region will cause large uncertainties in the temperature and oxygen mole fraction measurements.

3.1.1.4 Error Analysis

The spatial uncertainty in the RSD measurement is approximated as half of the least count, which depends on the image size and resolution. In the present system, it was calculated as 0.06 mm. From equation (3.5), the uncertainty in the normalized refractive index difference is given by (Dasch, 1992)

$$\Delta\delta_i = \sqrt{\sum_{j=i}^N (D_{ij} \cdot \Delta\varepsilon_j)^2} \quad (3.10)$$

where $\Delta\varepsilon_j$ is the local uncertainty in the angular deflection obtained from equation (3.3) as

$$\Delta\varepsilon_j = \frac{\Delta d_j}{f} \quad (3.11)$$

and Δd_j is the local uncertainty in the transverse ray displacement at the filter plane. The Δd_j for a given hue in the schlieren image is found from the standard deviation in the filter calibration curve (see Fig. 3.6). Finally, uncertainties in temperature and species mole fractions are obtained by evaluating the variables at δ and $\delta + \Delta\delta$ from equation (3.9).

A plot of the integrated error coefficient, $\sqrt{\sum_{j=i}^N D_{ij}^2}$ (see equation (3.10)) as a function of the radial location is shown in Fig. 3.10. This plot is shown to gain an understanding of how the measurement error propagates into error in the refractive index. Clearly, the error coefficient is largest near the center, which signifies that a

small measurement error in that region causes large error in the reconstructed normalized refractive index difference, and hence in the temperature and oxygen mole fraction.

3.1.2 Fuel Supply and Ignition Systems

A schematic of the fuel supply system is shown in Fig. 3.11. It consists of a 1000-ml storage vessel, a pressure regulator, 6.35 mm diameter stainless steel delivery tubes, a relief valve, shut-off valves, a mass flow meter, a solenoid valve, and a stainless steel burner tube. A small plenum was provided upstream of the fuel tube to damp out the flow fluctuations. The fuel was ignited by a custom built spark-ignition system with TTL input. A tubular solenoid was used to traverse the igniter.

3.1.3 Data Acquisition and Control Systems

A ruggedized industrial Pentium 166 MHz computer with 192 MB of RAM in a compact card cage (350x180x230 mm) operating under Windows 95 is used for data acquisition and control. The computer has an interface card (Strawberry Tree Model DyanaRes 16) for data acquisition and control of the experiment on a continuous basis. The real time images from the camera are acquired at 30 Hz with a 24-bit PCI bus frame grabber (Matrox Meteor/RGB). The system RAM is used to store about 6 seconds of color images in TIFF format at a resolution of 640x480. An ethernet adapter is used to transfer the digital images from the computer memory to an external disk storage media.

3.1.4 Power Distribution System

The power distribution system is shown in Fig. 3.12. There are nine on/off independent switches; 6 are in use and 3 are auxiliary. Two test switches are used to manually test the ignition solenoid and the fuel solenoid valve. Two charging ports, protected by a diode, are provided to charge the two 12-V, 17.5-Amp-hour batteries connected in series. A double-type DC/DC converter is used to supply power at +/- 15 volts to the mass flow meter.

3.2 Normal Gravity Probe Measurements

Probe measurements in the hydrogen gas-jet diffusion flame in normal gravity were used to validate the RSD technique. Details of these measurements, including the error analysis are given next.

3.2.1 Oxygen Mole Fraction

The setup to measure oxygen mole fraction consisted of a 3-mm ID, 0.5-mm thick quartz tube (Fig. 3.13) bent 90 degrees and reduced gradually to 0.76-mm OD and 0.4-mm ID, a 50-W diaphragm vacuum pump, on-line dehydrators, a calibrated diffusion based oxygen analyzer, and a 3-D traversing system with stepper motors. A computerized data acquisition and control system with icon-based software was used to digitize the analyzer output and to automate the probe movement. Probe measurements were made at axial planes 5 and 10 mm above the jet exit. The measurements were based on continuous sampling, while moving the probe across the flame in increments of 0.635 mm and allowing 30 seconds to reach steady-state at

each point. The average mole fraction at each point was computed from 100 samples taken at 10Hz. The oxygen concentration analyzer had measurement accuracy of 1 % of the reading. Care was taken to extract the sample at a rate to minimize the difference between the flow and suction velocities. The sampling probe size error is expected to be small because the probe was thin (ID=0.4 mm). The averaging error is expected to cancel because the oxygen mole fraction varied monotonically in the radial direction. Random error because of the flow drift was negligible since the flame was stable during the measurements.

3.1.2 Temperature Measurement

The setup to measure temperature consisted of an R-type (Pt-Pt 13% Rh) thermocouple made with wires of 0.127-mm diameter to form a 0.7-mm diameter bead, which was coated with silicon. The probe was traversed across the flame in increments of 0.635 mm at axial planes 5 and 10 mm above the jet exit. The thermocouple readings were corrected for radiation, while accounting for variations in the thermocouple emissivity and gas (assumed air) transport properties with temperature (Holman, 1989). The conductive heat transfer through the wires was neglected. The temperature fixed errors were primarily because of the radiation, conduction, and spatial averaging. The maximum radiation correction was about 250 K at a measured temperature of 1750 K. Based on the analysis, the radiation errors were negligible at temperatures below 1000 K. The averaging and conduction errors were not corrected for although the conduction error is expected to be small because of the small diameter (0.127 mm) of the wire used. The averaging error is expected

to cancel out in the outer regions where the temperature varies monotonically. However, the average error will be maximum at extreme locations i.e., at the center and at the flame sheet where the temperature is maximum.

3.3 Test Procedure

In this section, the drop tower used at NASA Lewis Research Center, including the drop procedure is briefly described.

3.3.1 Drop Tower

The microgravity experiments were performed at the 2.2-s drop tower facility of NASA Lewis Research Center in Cleveland, Ohio. The drop tower operates under normal atmospheric conditions. To reduce drag, the drop test rig (frame) is placed in a drag shield (Fig. 3.14) before the package is allowed to free-fall 79 ft. The gravitational acceleration attained is on the order of 10^{-6} g for a period of 2.2 s. The drag shield impacts on an airbag at the bottom of the tower, introducing a peak deceleration level of about 15 g's for a period of 0.2 seconds. For further details on the drop tower facility, the reader is referred to Lekan et al. (1996).

3.3.2 Drop Procedure

A 600- μm diameter fiber optic cable connected to an external light source provides the light input to the source aperture of the schlieren apparatus. Another fiber optic cable (62.5 μm) is used to transmit the camera signal to an external S-VHS recorder. Before the drop is initiated, the computer fans are turned off to minimize

the air circulation. The fuel is turned on, and then ignited using the spark ignition system. The igniter is then retracted and locked in place using a tubular solenoid. Once the flame is stabilized, acquisition of the schlieren images begins and the drop is initiated. Upon impact, the computer fans are turned back on and the fuel supply is shut-off. This overall sequence of events is automated by the data acquisition and control system. Data transfer begins after recovering the drop rig.

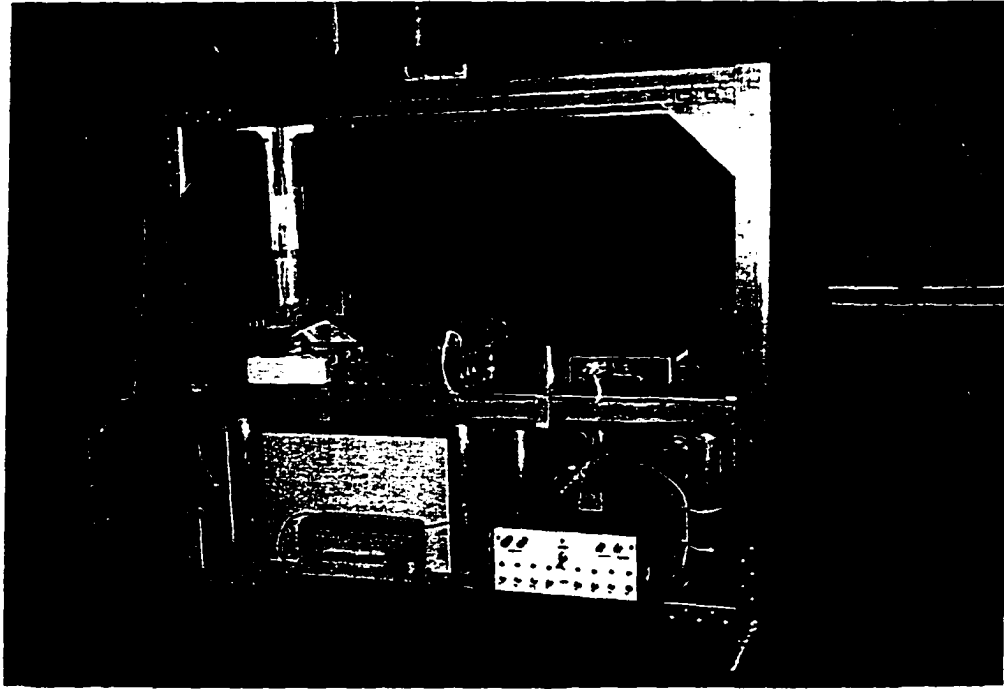
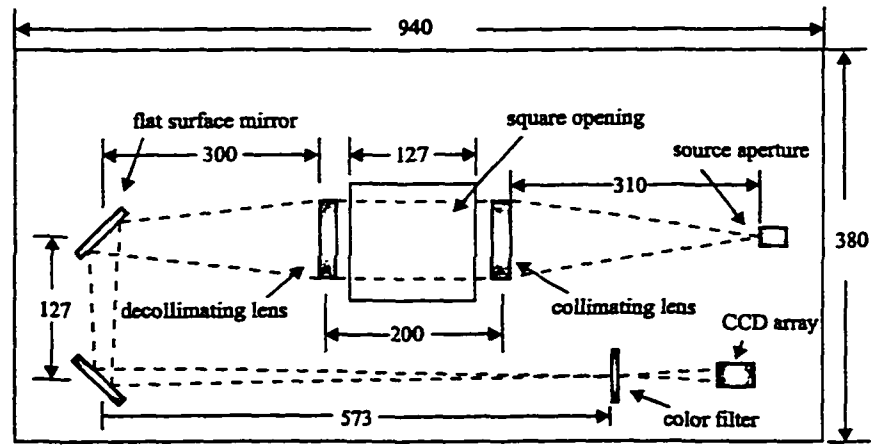


Figure 3.1: A photograph of the drop rig



all dimensions are in mm

Figure 3.2: Optical layout of the rainbow schlieren



Figure 3.3: A photograph of the symmetric color filter

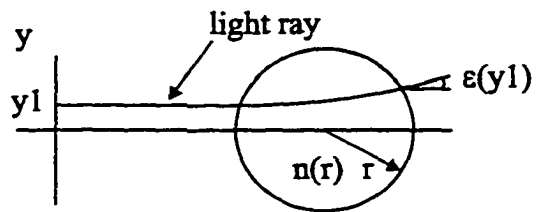
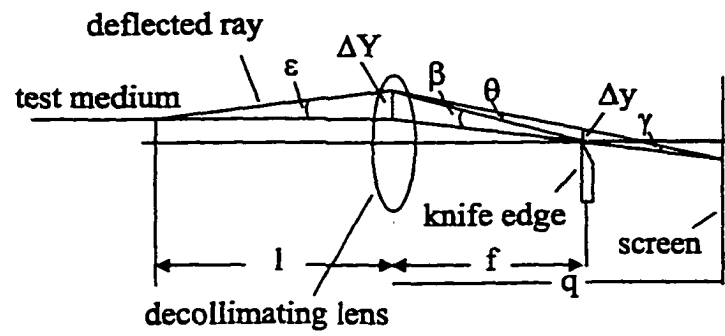


Figure 3.4: Light ray traversing a non-uniform refractive index field



for small ϵ :

$$\epsilon = \Delta Y/l$$

$$\beta = \Delta Y/f$$

$$\gamma = \Delta Y/q$$

$$\theta = \beta - \gamma$$

$$= \Delta Y(1/f - 1/q) = \Delta Y/l = \epsilon$$

$$\therefore \Delta y = \epsilon f$$

Figure 3.5: Ray displacement at the knife-edge for a given angular deflection

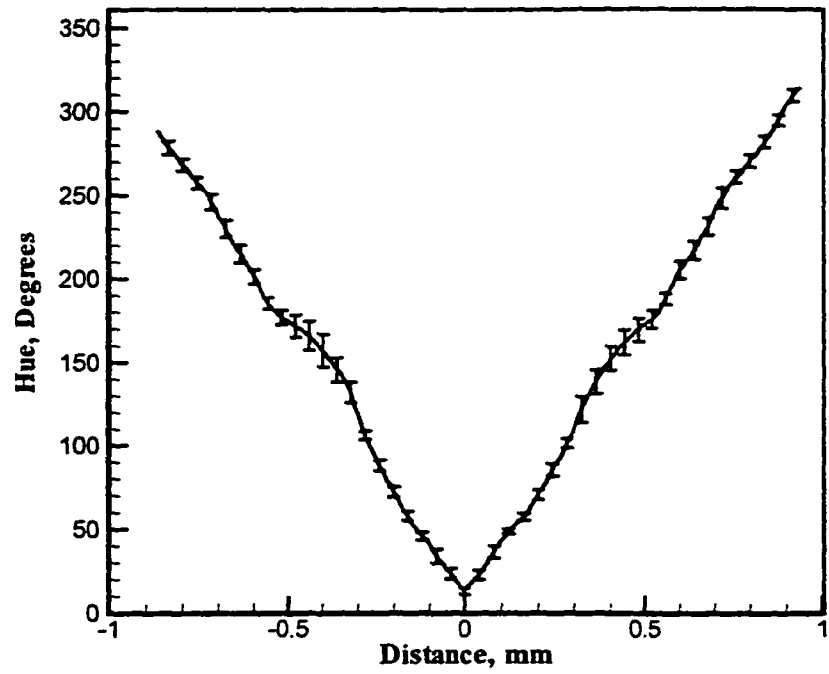


Figure 3.6: Filter calibration curve

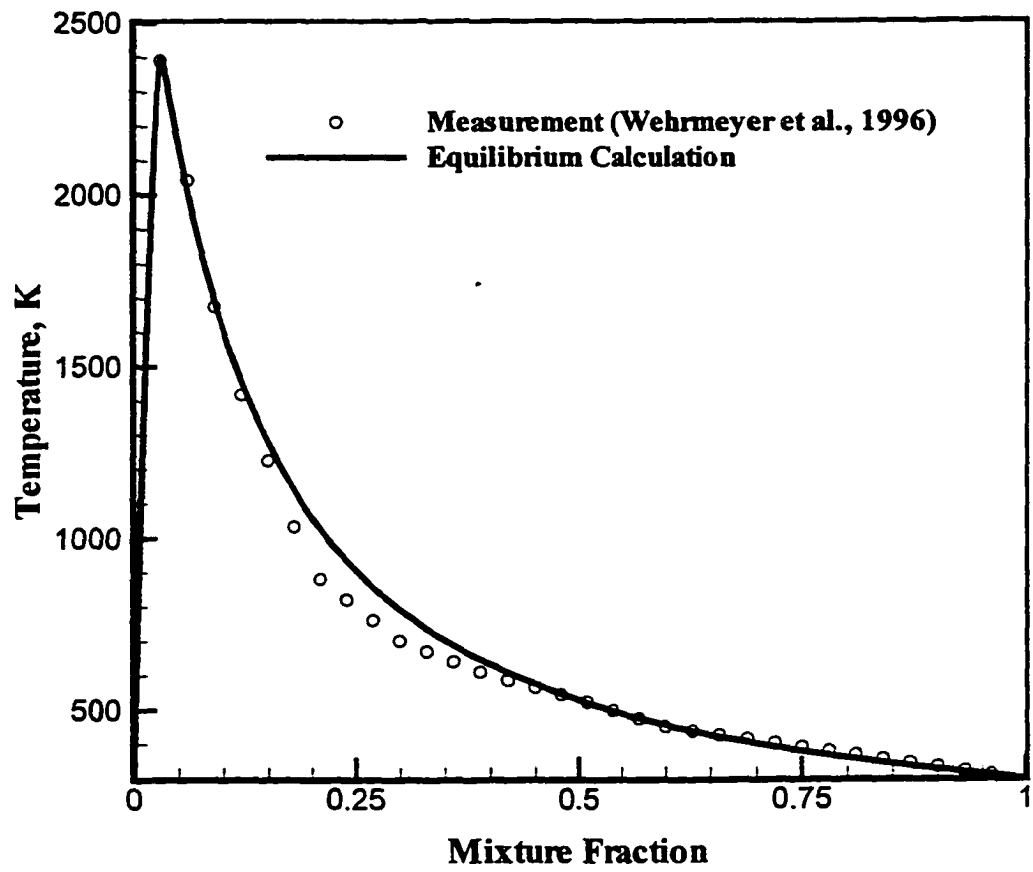


Figure 3.7: Measured and computed profiles of temperature versus mixture fraction

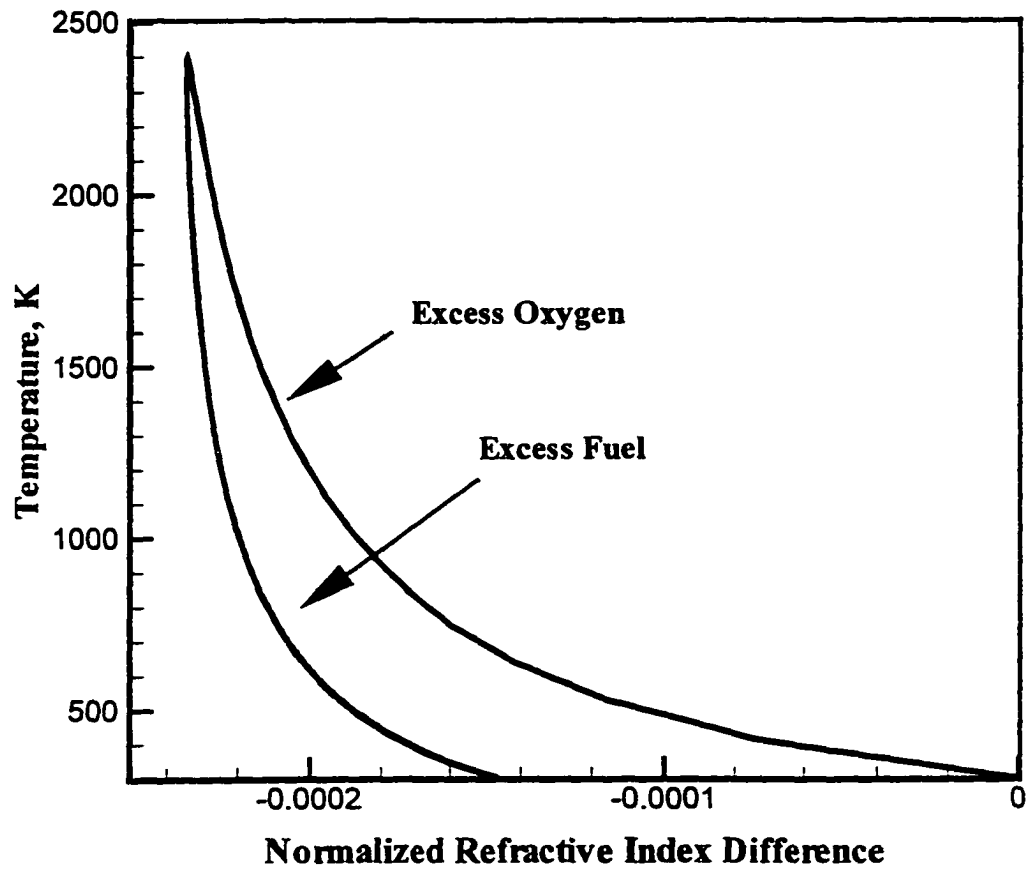


Figure 3.8: Temperature versus normalized refractive index difference at chemical equilibrium

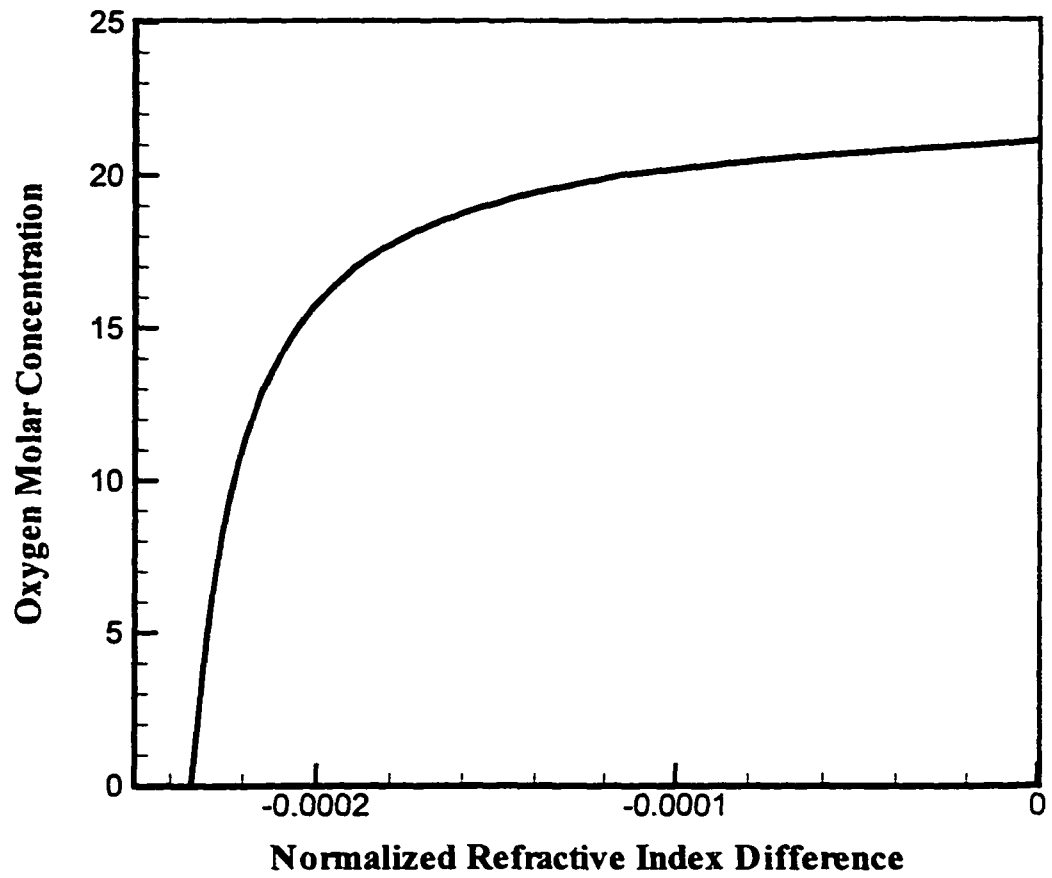


Figure 3.9: Oxygen mole fraction versus normalized refractive index difference at chemical equilibrium

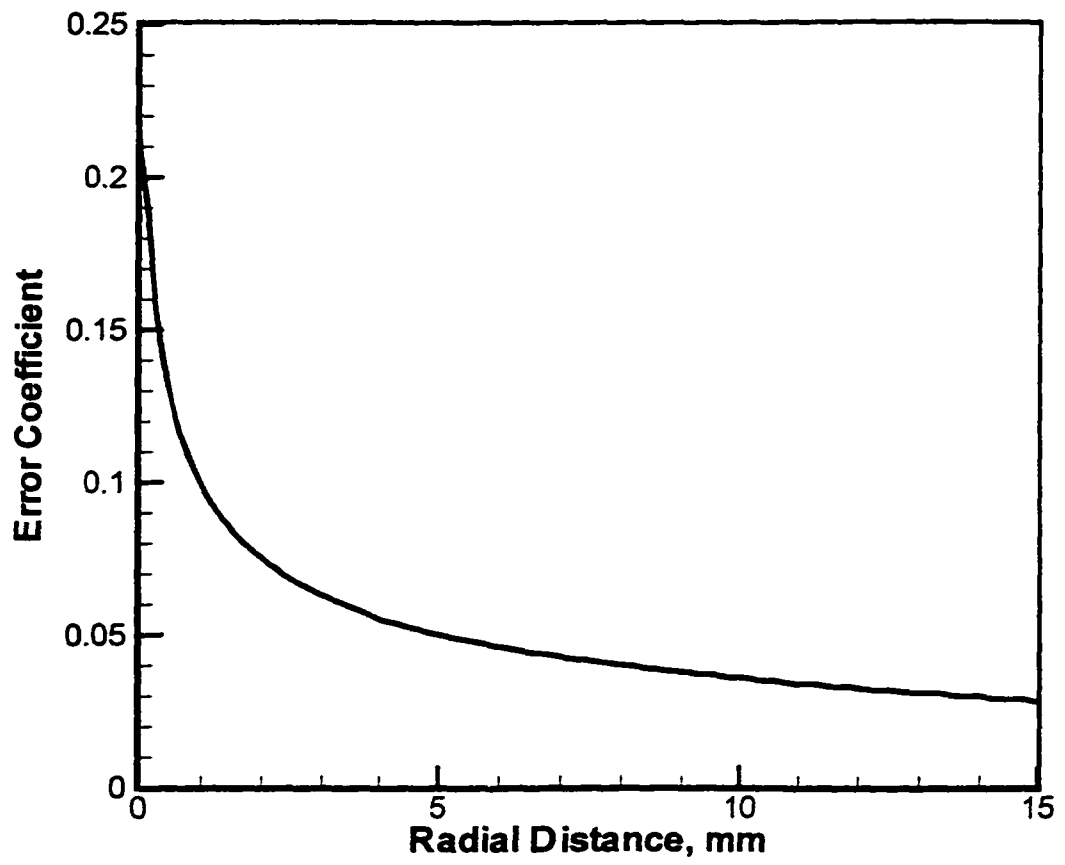


Figure 3.10: Error coefficient versus radial location

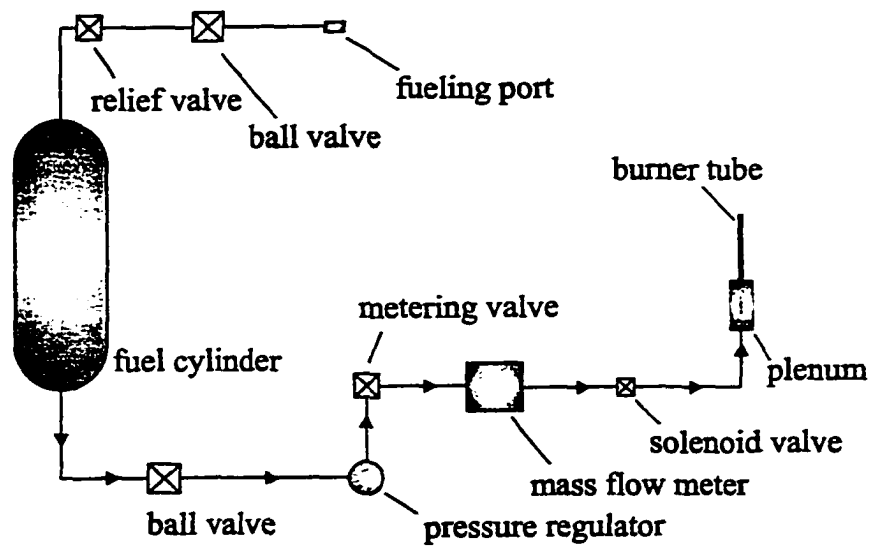


Figure 3.11: Schematic of the fuel supply system

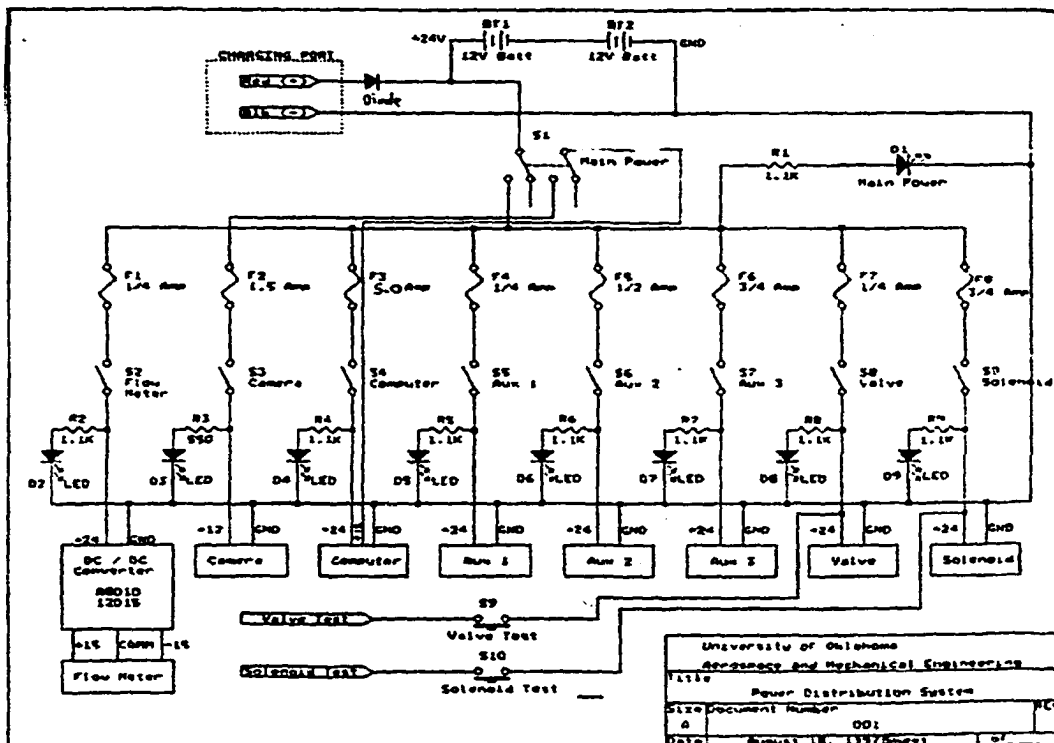


Figure 3.12: Power distribution system

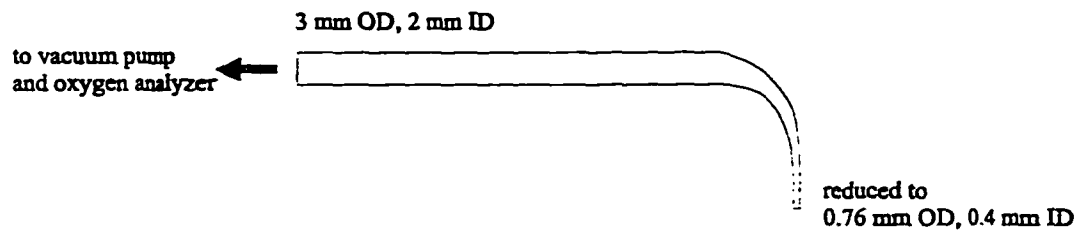


Figure 3.13: Sampling probe

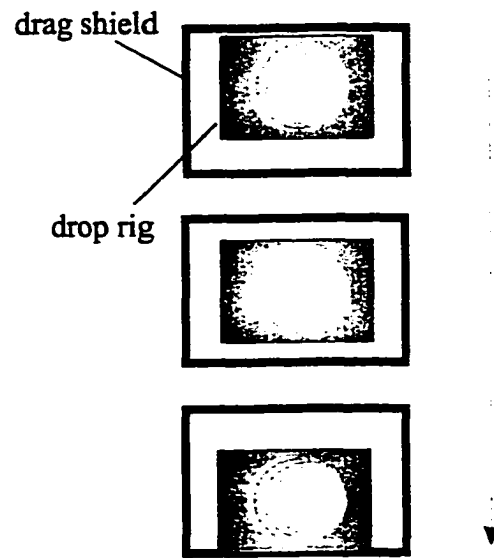


Figure 3.14: Drop rig inside the drag shield during the drop

Chapter 4

RESULTS AND DISCUSSION

In this chapter, the results are discussed, including validation of the RSD technique in a hydrogen-air reaction system, and buoyancy effects on laminar and transitional hydrogen gas-jet diffusion flames. The experimental data are also compared with theoretical predictions.

4.1 Probe Measurements and Chemical Equilibrium

Because probe measurements of temperature and oxygen mole fraction profiles were obtained independently, it is helpful to compare these measurements with chemical equilibrium predictions prior to validation of the RSD technique. Comparison of chemical equilibrium calculation with probe measurements of temperature (corrected for radiation losses) and oxygen mole fraction at $z/d = 4$ is shown in Fig. 4.1.1. The data were taken in a hydrogen-air diffusion flame with $Re = 70$ and $d = 1.19$ -mm. The two profiles of the probe measurements account for the two sides of the axisymmetric flame. As shown, the measurements agree reasonably well with chemical equilibrium calculations for temperatures of up to 1750 K, which is the highest temperature recorded by the thermocouple. The discrepancy above 1750 K is attributed to the thermocouple limitations, e.g., averaging effects, heat conduction, and possibly uncorrected radiation losses. Although a thermocouple is not suitable for measurements at high temperatures, it was the only choice available to us at the time. The probe measurements at $z/d = 8.4$ are compared with chemical

equilibrium calculations in Fig. 4.1.2, where we still see a reasonably good agreement for temperatures below 1750 K.

4.2 RSD Measurements

A color schlieren image of the hydrogen-air jet diffusion flame is shown in Fig. 4.2.1. The axial diffusion upstream of the burner exit is apparent in this image. Also, the flow symmetry is clearly evident from the image. This image was used to obtain the hue distribution at $z/d = 4.2$ shown in Fig. 4.2.2. Here, we observe that the hue at the center is slightly different from that in the background. In a perfectly symmetric flame, the refractive index gradient at the center is zero and hence, the hue is the same as that in the background. However, a slight flow asymmetry combined with high filter sensitivity increase the hue at the center. Also, non-linearity in the filter transmissivity function has introduced inflection points at a radial location between 4 and 6 mm. As mentioned before in Chapter 3, the filter non-linearity is attributed to the chromatic aberration in the decollimating lens.

Figure 4.2.2 together with the filter calibration curve (Fig. 3.5) were used to obtain the angular deflection distribution (dotted profile) shown in Fig. 4.2.3. Because the hue at the center was slightly higher than the background hue, the angular deflection has attained a non-zero value at the center. It was anticipated that the inflection points, evident in the hue distribution, will be absent in the angular deflection profile. However, the inflection points persisted because of the uncertainty in the filter calibration curve. One possible way to avoid uncertainty in the filter calibration curve is to calibrate the filter using a lens of specific refractive index

characteristics. Such a lens, however, is hard to manufacture. In this research, polynomials, with orders between 1.2 and 1.3 depending on the case, are used to remove the inflection points near the center introduced by the non-linear filter transmissivity function. The polynomials were constrained to provide zero angular deflection at the center point. The solid line in Fig. 4.2.3 shows the smoothed angular deflection distribution.

Figure 4.2.4 shows profiles of the normalized refractive index difference obtained using the raw (unsmoothed) and modified (smoothed) distributions of the angular deflection. The unsmoothed profile has resulted in an unrealistic distribution near the center. The smoothing has affected the region within 4 mm from the center. Moreover, the normalized refractive index difference profile has attained a shape typical of that in a diffusion flame. The oxygen mole fraction profiles resulting from the smoothed normalized refractive index profile in Fig. 4.2.4 together with the probe measurements are shown in Fig. 4.2.5. An excellent agreement between the RSD and probe measurements is evident. A minor discrepancy in the fuel-rich region is attributed primarily to the probe limitations. The RSD measurements show large uncertainty near the center because of the high uncertainty in the filter calibration curve in that region. In addition, the reconstruction error is highest near the center (see Fig. 3.9) and the oxygen mole fraction is most sensitive to the refractive index near the flame (see Fig. 3.8).

The probe and RSD temperature measurements at $z/d = 4.2$ are shown in Fig. 4.2.6. The agreement between the two techniques is good in the fuel-lean side of the flame for temperatures of up to about 1750 K. The discrepancy at temperatures

higher than 1750 K is attributed to thermocouple limitations. The RSD temperature profile in the fuel-rich region is qualitatively reasonable although the measurement uncertainty is large because of the uncertainty in the filter calibration, reconstruction errors, and sensitivity of temperature to the refractive index (see Fig. 3.7). In addition, preferential diffusion and/or incomplete chemical reaction may affect the RSD measurements in that region.

The profiles of the oxygen mole fraction at $z/d = 8.4$ are shown in Fig. 4.2.7. Again, good agreement between the two measurement techniques is obtained. Finally, measurements of temperature at $z/d = 8.4$ by RSD and probe techniques are compared in Fig. 4.2.8. Again, good agreement between the two techniques is reached in the fuel-lean side of the flame, while the RSD measurements in the fuel-rich side suffer from the limitations discussed previously.

4.3 Buoyancy Effects on Laminar Diffusion Flames

In this section, the temporal evolution of diffusion flames in the drop tower is investigated. In addition, the scalar profiles and flame shapes in normal and microgravity for different burners and Reynolds numbers are presented. Finally, comparison of the RSD measurements with theoretical predictions in microgravity is made.

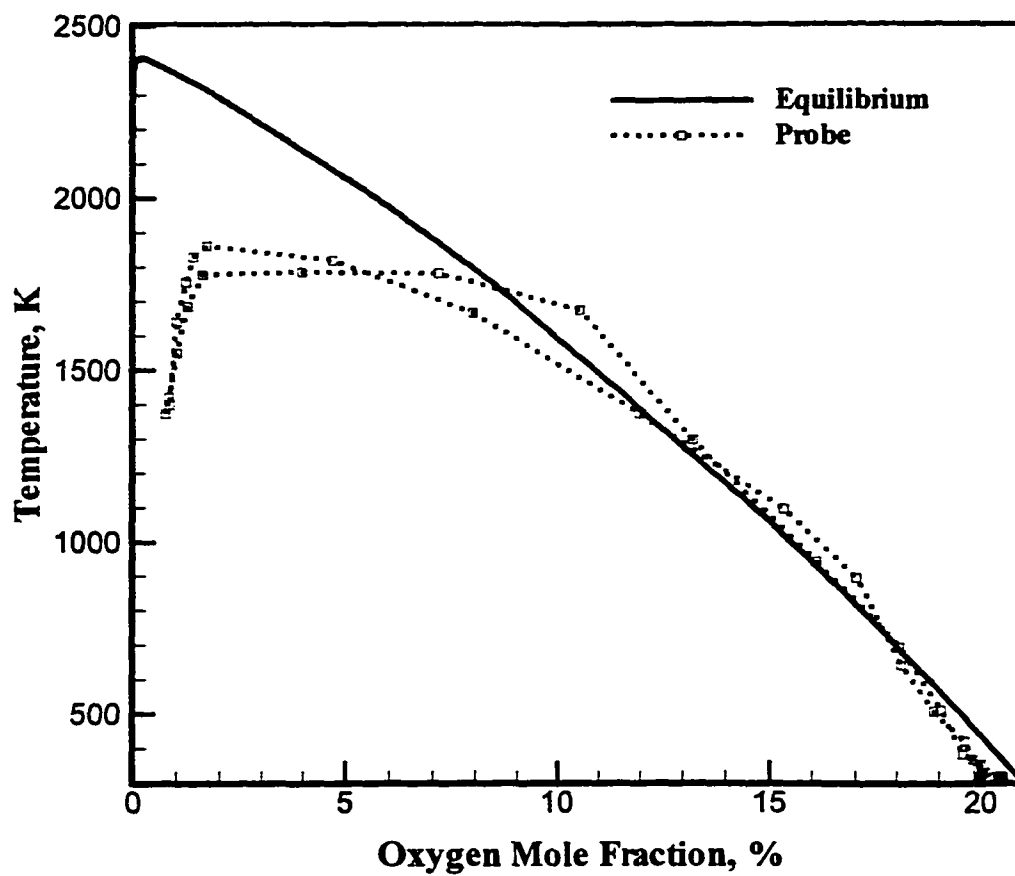


Figure 4.1.1: Temperature versus oxygen mole fraction; $Re = 70$, $d = 1.19$ mm, and $z/d = 4.2$

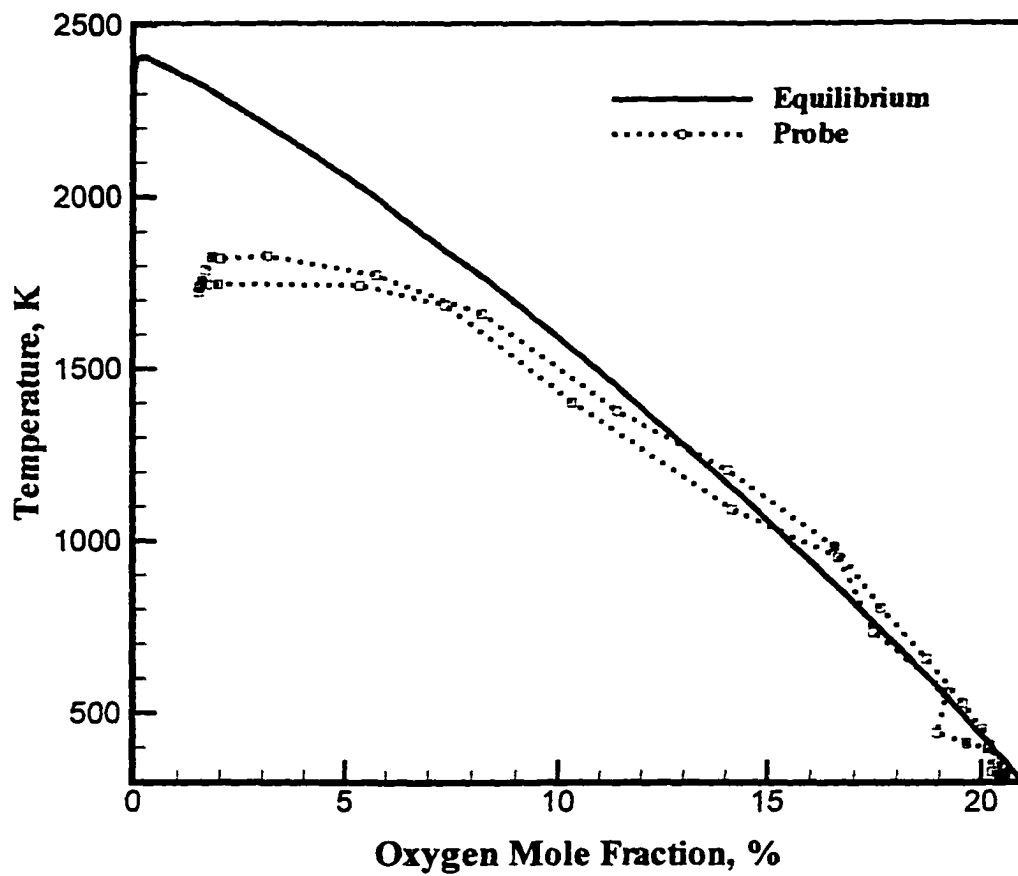


Figure 4.1.2: Temperature versus oxygen mole fraction; $Re = 70$, $d = 1.19$ mm, and $z/d = 8.4$

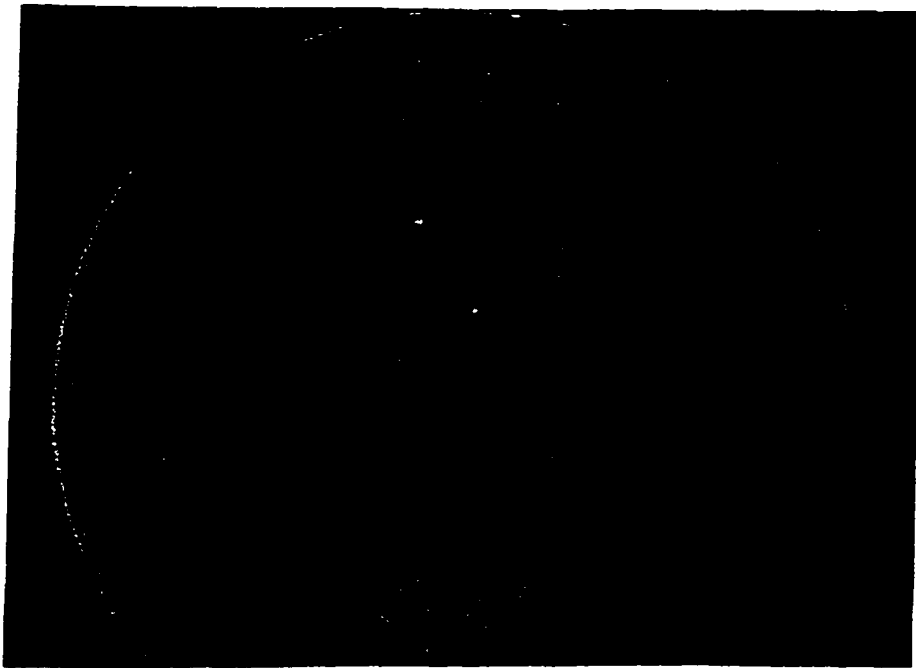


Figure 4.2.1: Schlieren image of hydrogen gas-jet diffusion flame in normal gravity;
 $Re = 70$ and $d = 1.19$ mm

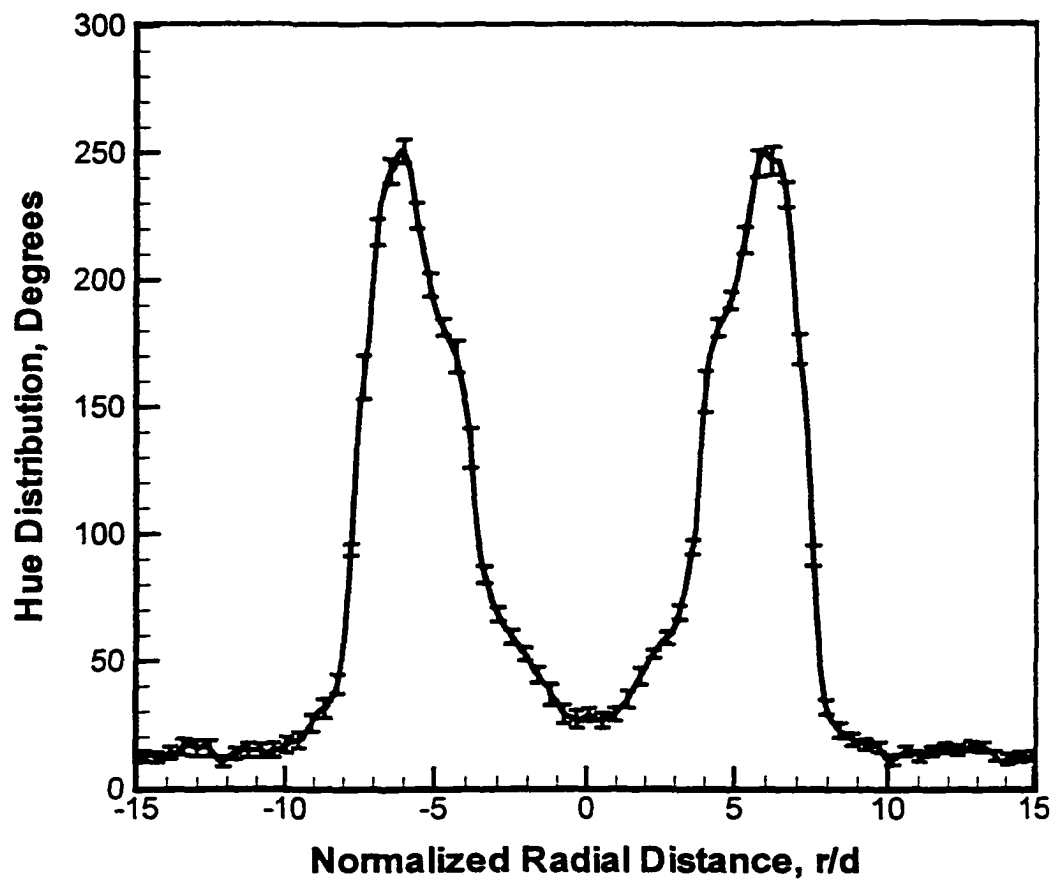


Figure 4.2.2: Hue distribution; $Re = 70$, $d = 1.19$ mm, and $z/d = 4.2$

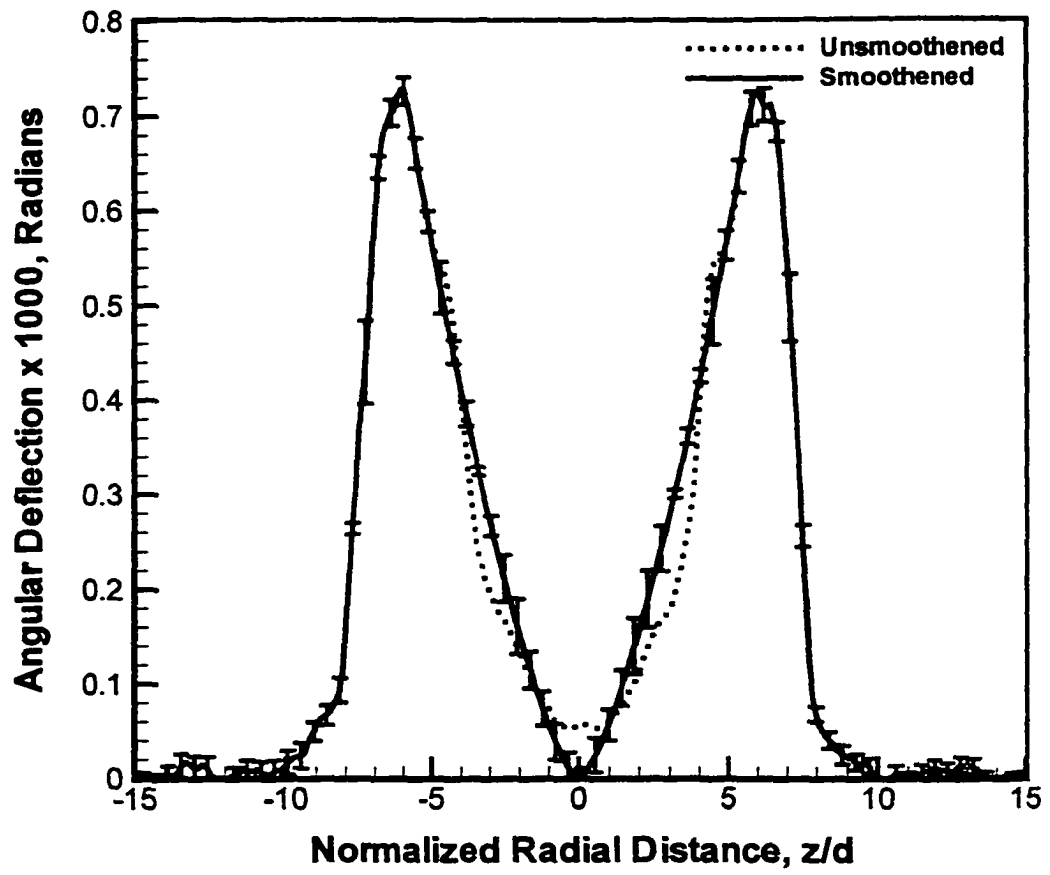


Figure 4.2.3: Angular deflection distribution; $Re = 70$, $d = 1.19$ mm, and $z/d = 4.2$

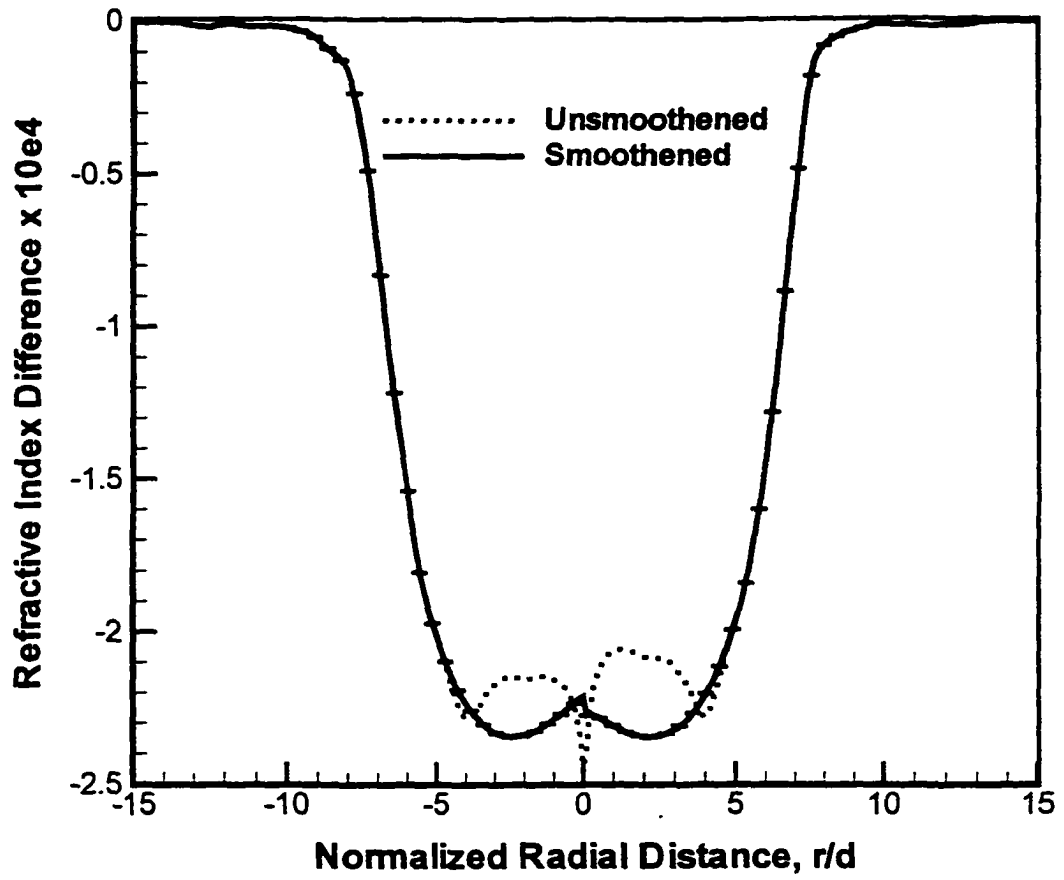


Figure 4.2.4: Normalized refractive index distribution; $Re = 70$, $d = 1.19$ mm, and $z/d = 4.2$

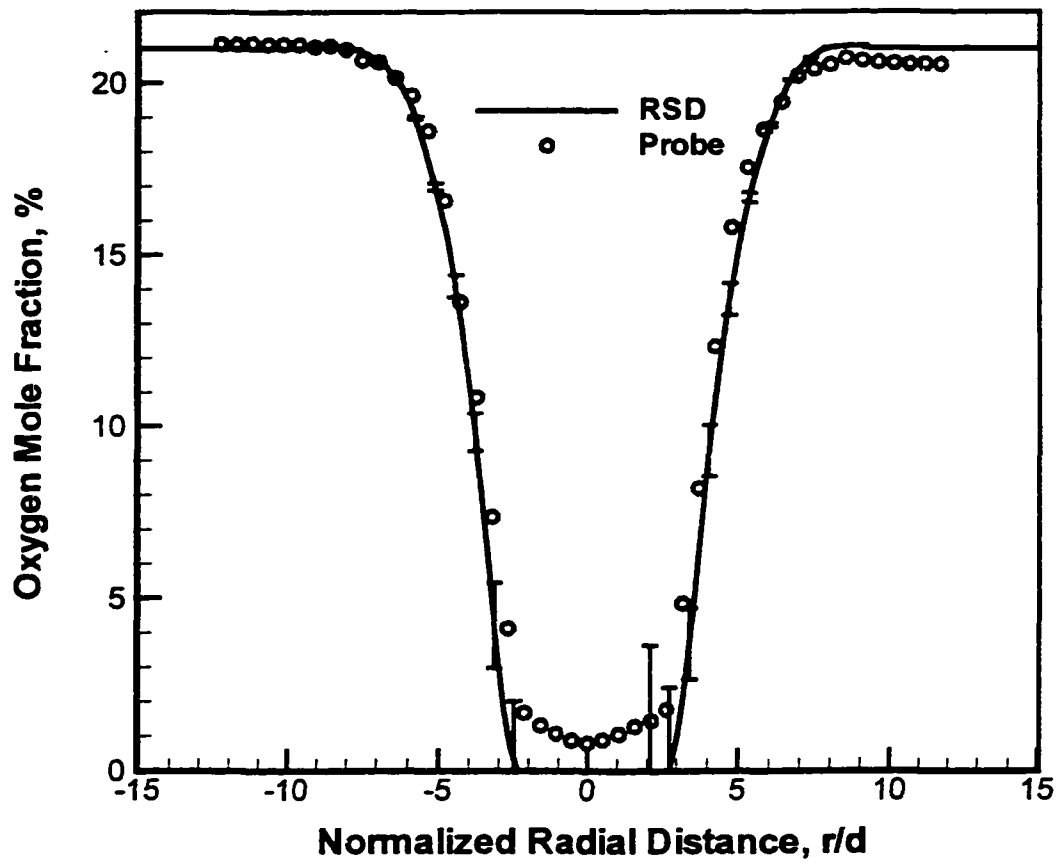


Figure 4.2.5: Oxygen mole fraction; $Re = 70$, $d = 1.19$ mm, and $z/d = 4.2$

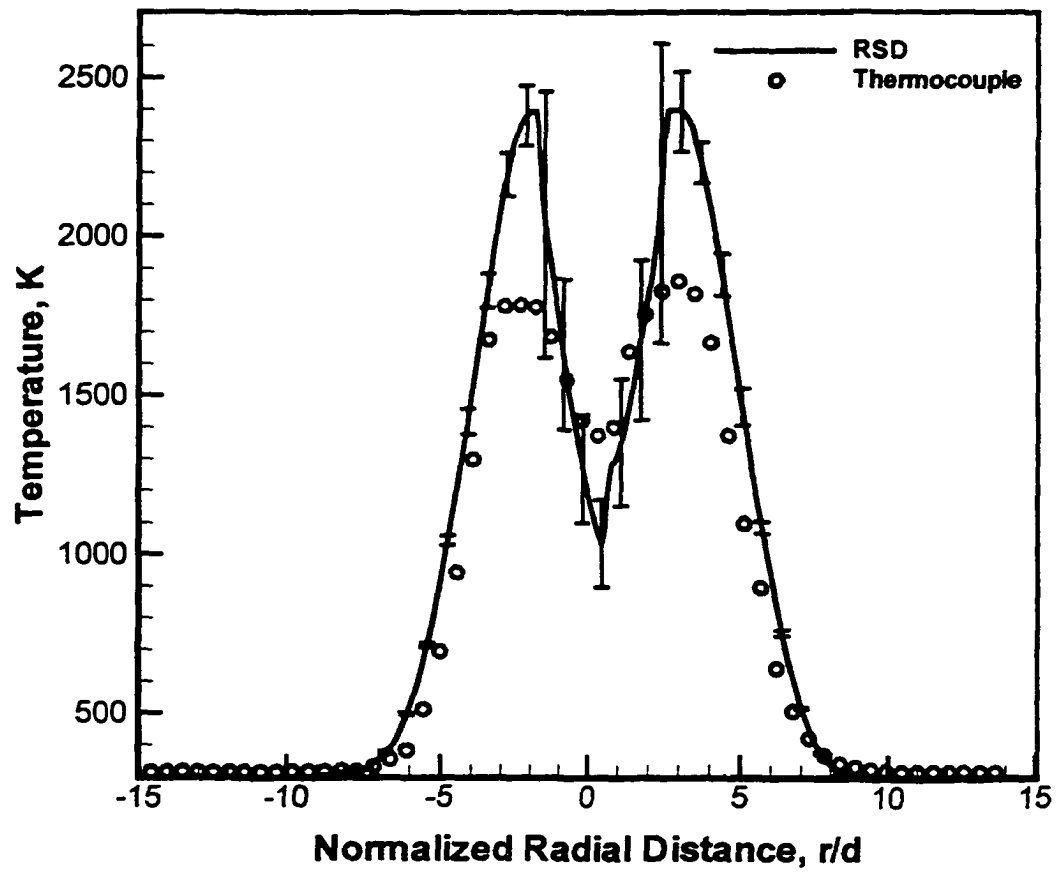


Figure 4.2.6: Temperature distribution; $Re = 70$, $d = 1.19$ mm, and $z/d = 4.2$

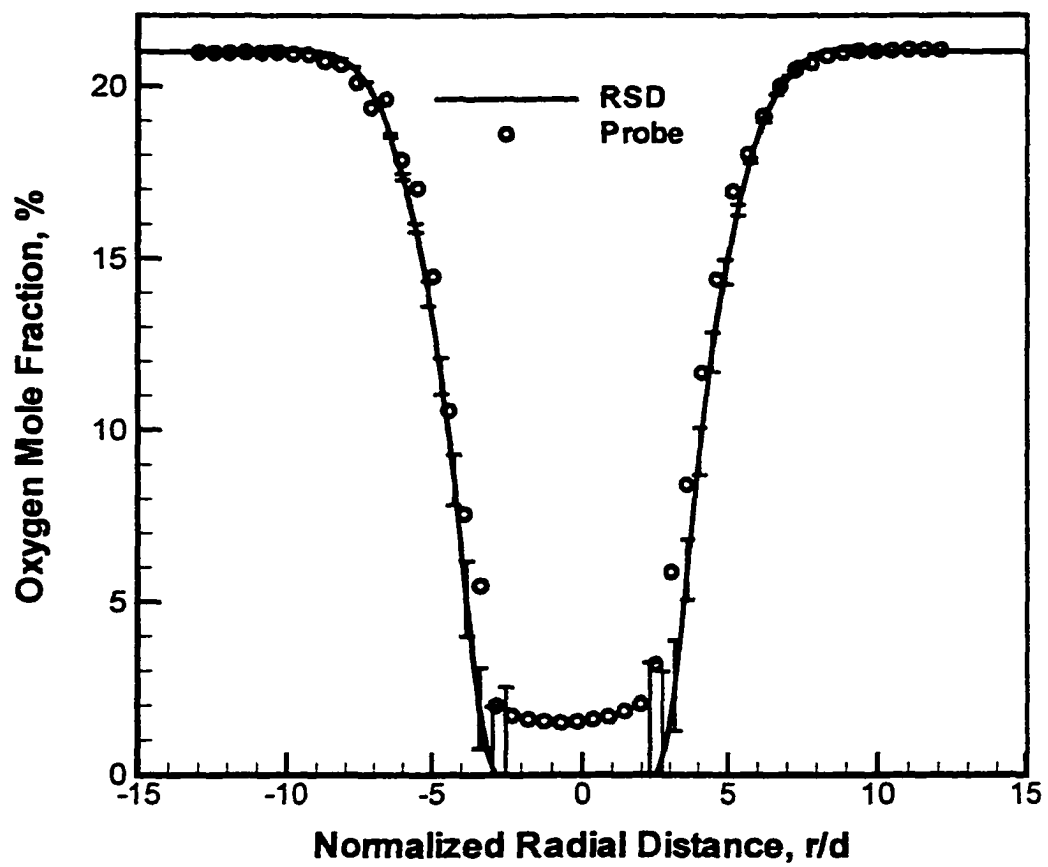


Figure 4.2.7: Oxygen mole fraction; for $Re = 70$, $d = 1.19$ mm, and $z/d = 8.4$

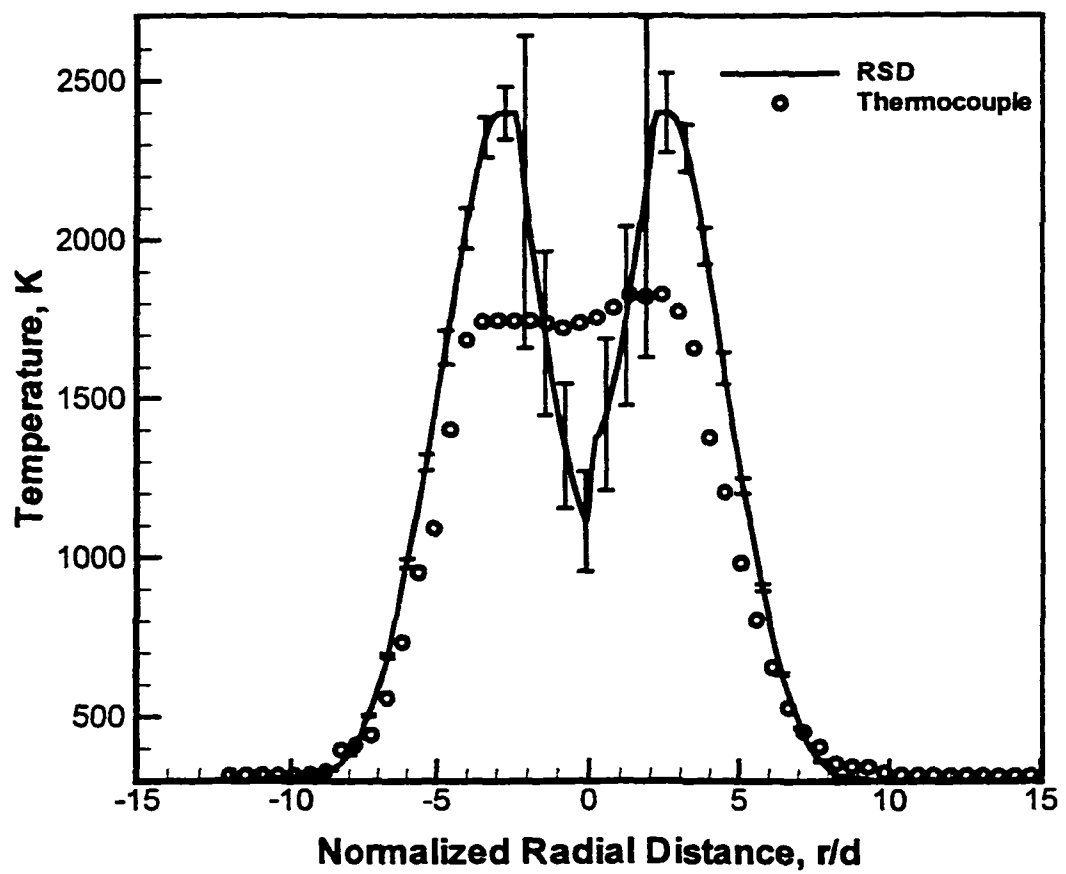


Figure 4.2.8: Temperature distribution for $Re = 70$, $d = 1.19$ mm, and $z/d = 8.4$

4.3.1 Base-Line Case

In this sub-section, the temporal evolution of the temperature profiles in the drop tower is presented. Also, scalar profiles and flame shape for the base-line case i.e., $Re = 70$ and $d = 1.19$ mm are discussed.

4.3.1.1 Temporal Evolution of Flame in the Drop Tower

Previous experiments have shown that the flame may not reach steady-state conditions in the limited microgravity duration obtained in the drop tower. This issue was examined to determine the extent of steady-state conditions in the present hydrogen-air diffusion flame.

Schlieren images of the hydrogen gas-jet diffusion flame in normal and microgravity are shown in Fig. 4.3.1. The schlieren boundary in microgravity is clearly wider than that in normal gravity. Also, the axial diffusion upstream of the burner exit is more significant in microgravity than that in normal gravity. Hydrogen is lighter than air, which makes hydrogen diffuse further into air upon entering microgravity. If, for example, the fuel were propane, which is heavier than air, the diffusion would have been in the opposite direction i.e., air would diffuse into propane, which would make the schlieren boundary narrower upon entering microgravity. To gain understanding of the temporal evolution of flame in the drop tower, the color schlieren images were used to create contours of angular deflections shown in Figs. 4.3.2 to 4.3.13. Note the symmetry of the angular deflection field in Fig. 4.2.2, which marks the beginning of the drop. The curvature near the burner in contours of the angular deflection reveals large axial gradients that decrease in the

axial direction, becoming negligible at $z/d > 15$ when the contours are parallel to each other. The initial jet momentum and buoyancy driven acceleration enhance axial mixing at downstream locations. Thus, the axial variation in temperature or density and hence, in angular deflection becomes small. A small spacing between contours indicates large radial gradient of the deflection angle. Large radial gradients in the outer region mark the thermal boundary layer between the flame surface and the surrounding cold air.

The contour plot in Fig. 4.3.3 corresponds to 0.2 s after the drop commenced. Considering the short time interval in microgravity, the change in flame characteristics is substantial. Note that the greatest change in microgravity occurs in the near-burner region. Evidently, the buoyancy driven acceleration in normal gravity flame is significant in that region where the jet momentum is relatively small. The radial gradients of the deflection angle here are qualitatively similar to those in normal gravity, although the magnitude is smaller, suggesting smaller radial diffusion rate in microgravity. Smaller diffusion rates in microgravity are responsible for small variations in deflection angle contours after approximately 0.5 s, as discussed next. Lower radial diffusion rates in microgravity were also reported by Silver et al. (1995).

The angular deflection contours at $t = 0.41$ s are shown in Fig. 4.3.4. Here, the radial expansion since $t = 0.2$ s is still significant, suggesting that the flame has not reached steady-state conditions. Subsequently at $t = 0.61$ s, the change in the flow field is small but noticeable (see Fig. 4.3.5). The next contour plot at $t = 0.78$ s is shown in Fig. 4.3.6. The plot suggests that the flow field has reached near steady-state. Later, it will be shown that at certain flow conditions, the flow field in the outer

region varies throughout the drop period, even though the flame surface reaches steady-state condition. Slow diffusion in the outer regions of the flame is evident in Figs. 4.3.7 to 4.3.13 for the remaining of the 2.2-s drop. The last figure in this sequence at $t = 2.14$ s (Fig. 4.3.13) represents the flame in microgravity. The curvature of the contours indicates that the axial gradient is significant throughout the flow field. A larger spacing between contours indicates small radial gradients in the microgravity flame. The axial diffusion upstream of the burner is significant in microgravity compared to that in normal gravity.

Although contours of the angular deflection shown above provide qualitative and quantitative description of the flow field, the temperature profiles are presented next to gain an understanding of the local flame characteristics during the drop. The temperature profiles at different axial locations and different times were obtained from schlieren images using the analysis as discussed in section 4.2.

Figure 4.3.14 shows the temperature profiles at $z/d=4$ during the drop. These profiles are shown only for the oxidizer side of the flame. The 300-K profile represents the schlieren boundary and 2400-K profile corresponds to the flame surface. Here, it is shown that the flame surface reaches steady-state earlier than the schlieren boundary. The time to achieve near steady-state was about 0.3 s and 1.0 s for the flame surface and schlieren boundary, respectively. However, note that a minor increase in the schlieren boundary continued throughout the drop. The temperature profiles at $z/d = 8$ are shown in Fig. 4.3.15. The profiles show similar trends as discussed previously for $z/d = 4$. These results suggest that a microgravity flame at near steady-state conditions was achieved in present experiments using the

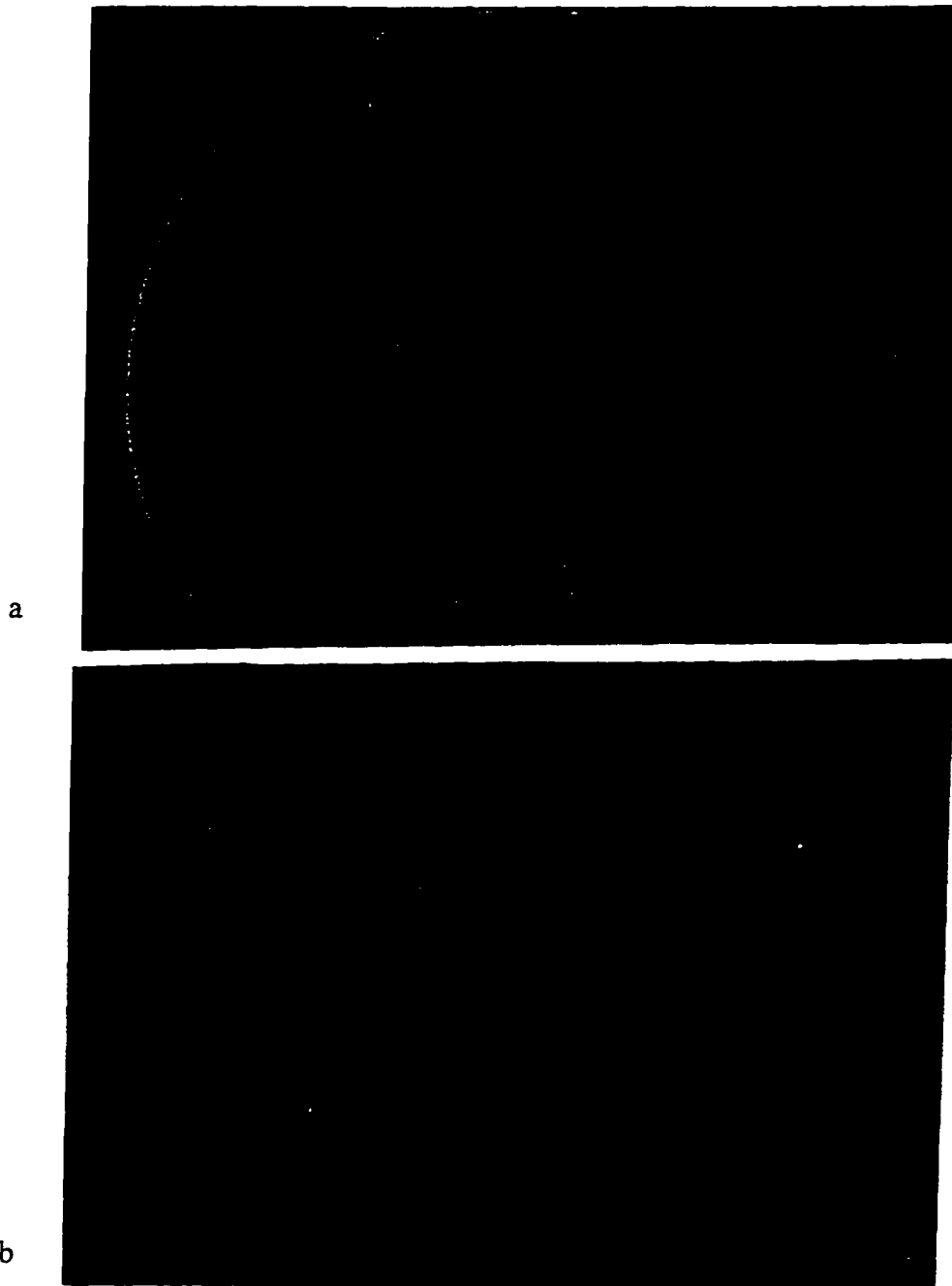


Figure 4.3.1: Schlieren images of hydrogen gas-jet diffusion flame in normal (a) and microgravity (b); $Re = 70$ and $d = 1.19$ mm

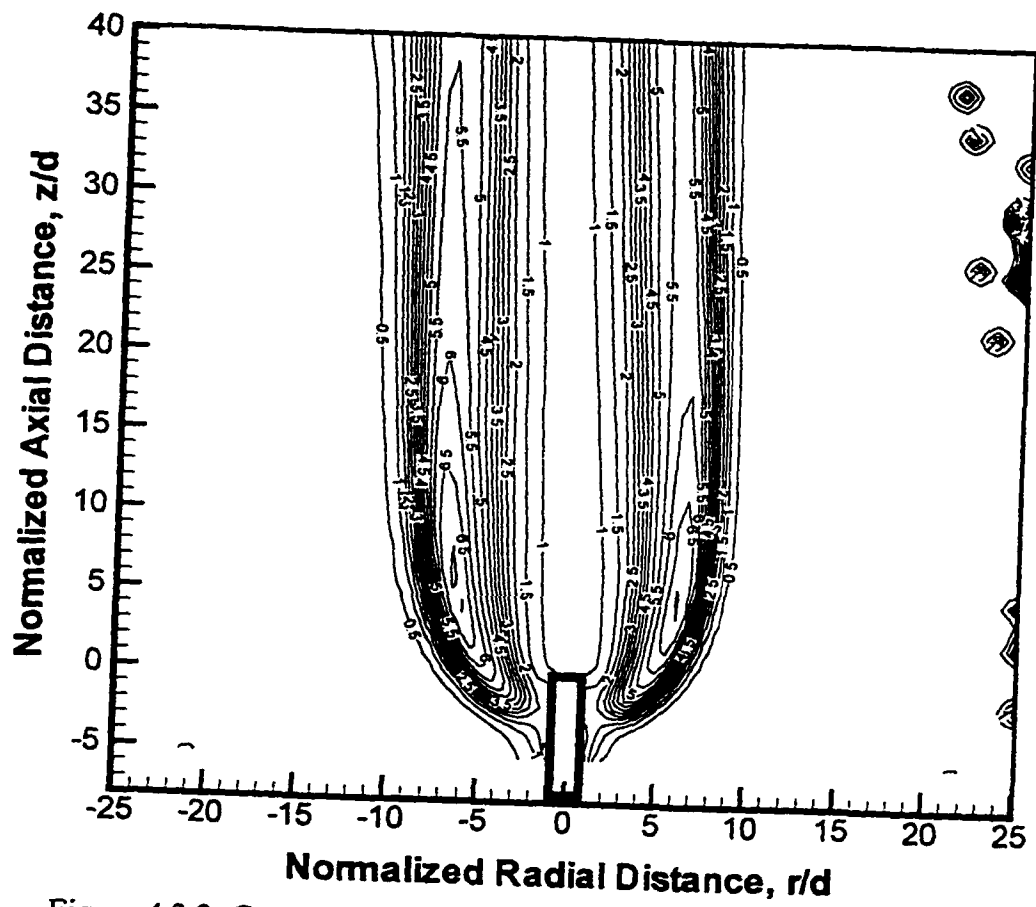


Figure 4.3.2: Contours of angular deflection in units of 10^{-4} radians; $Re = 70$, $d = 1.19$ mm, and $t = 0$ s

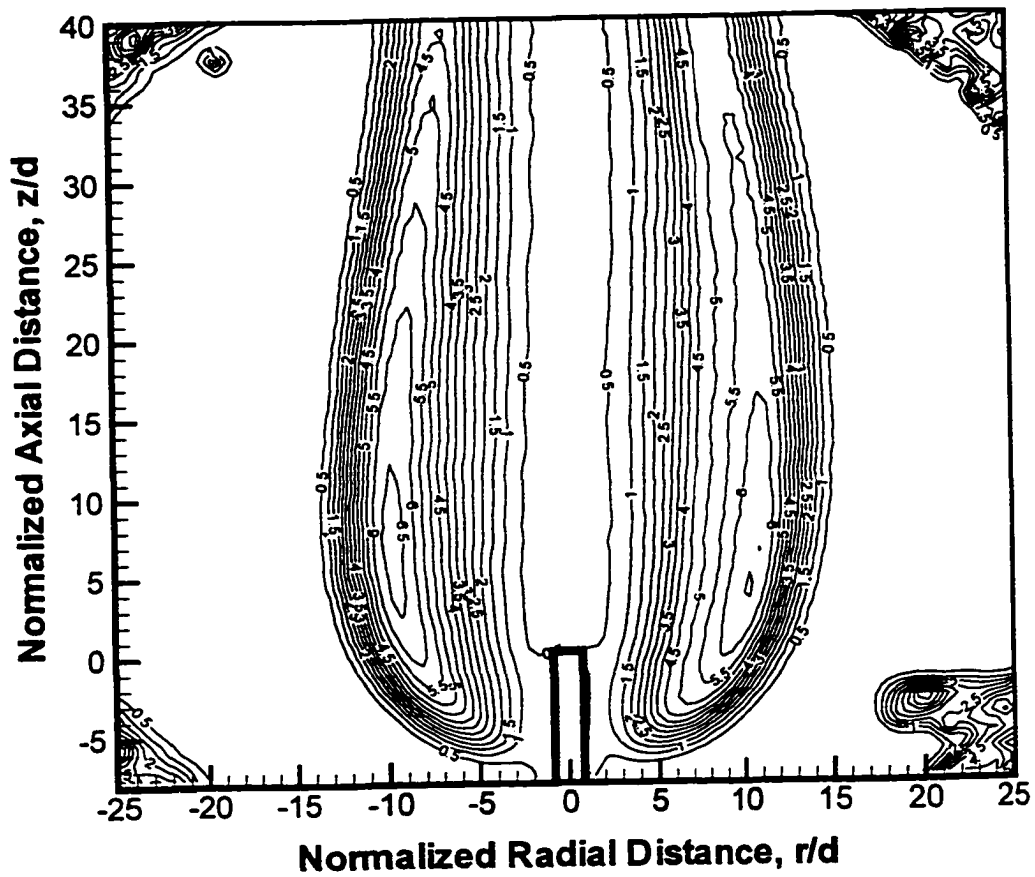


Figure 4.3.3: Contours of angular deflection in units of 10^{-4} radians;
 $Re = 70$, $d = 1.19$ mm, and $t = 0.2$ s

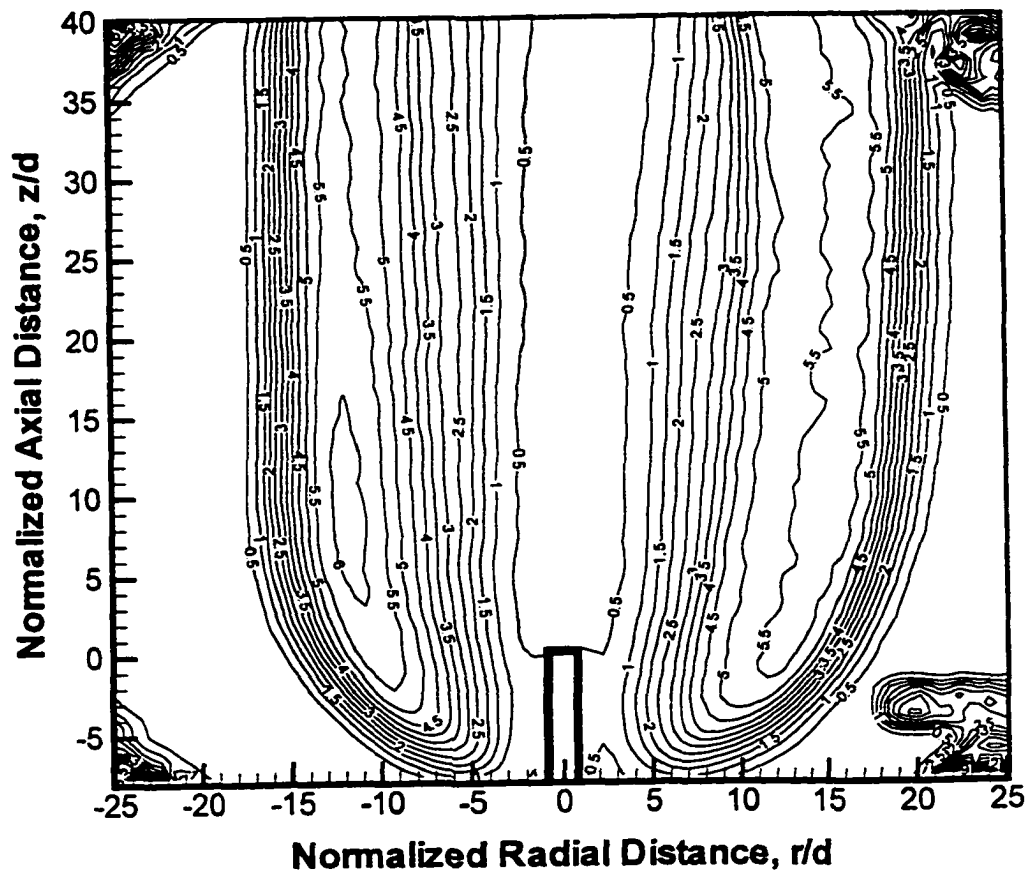


Figure 4.3.4: Contours of angular deflection in units of 10^{-4} radians;
 $Re = 70$, $d = 1.19$ mm, and $t = 0.41$ s

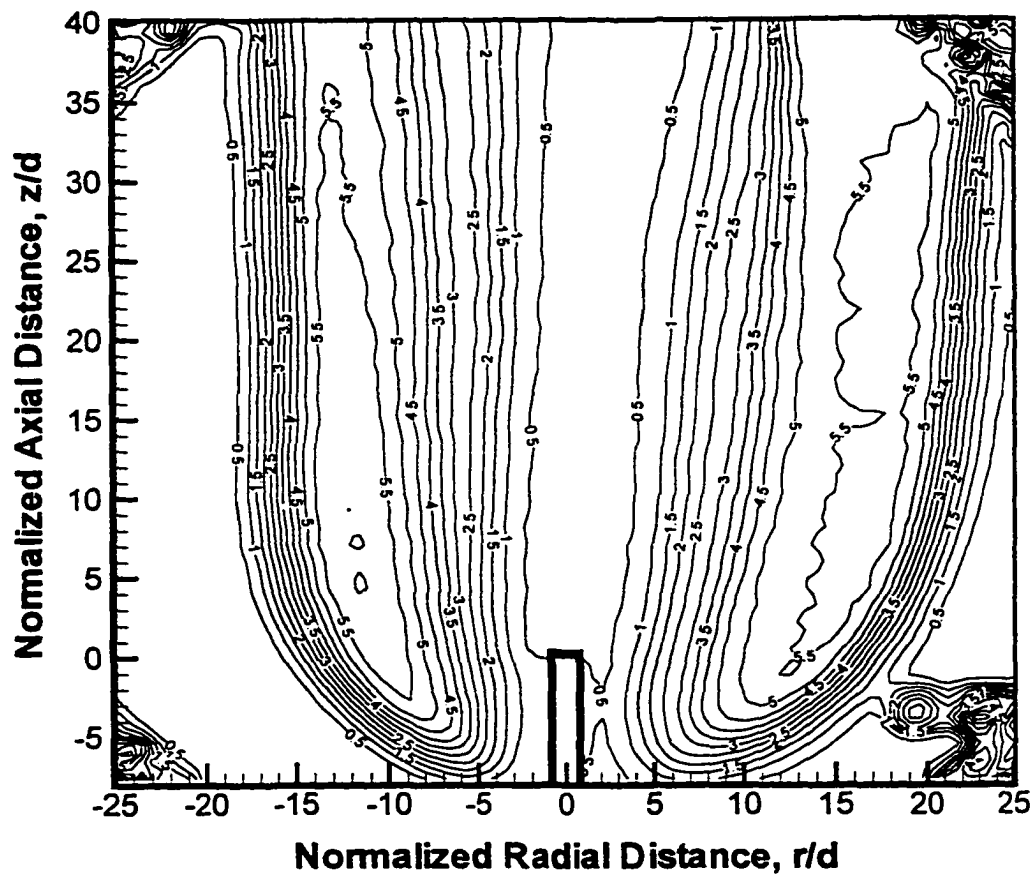


Figure 4.3.5: Contours of angular deflection in units of 10^{-4} radians;
 $Re = 70$, $d = 1.19$ mm, and $t = 0.61$ s

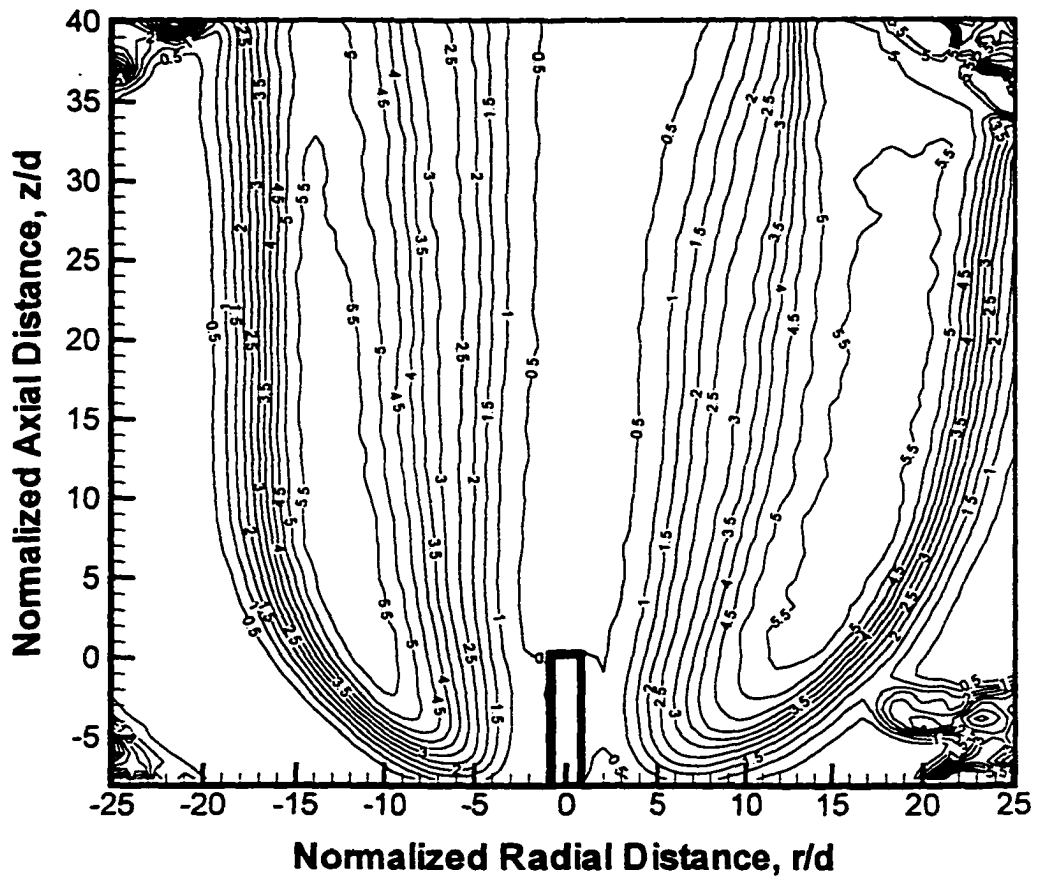


Figure 4.3.6: Contours of angular deflection in units of 10^{-4} radians;
 $Re = 70$, $d = 1.19$ mm, and $t = 0.78$ s

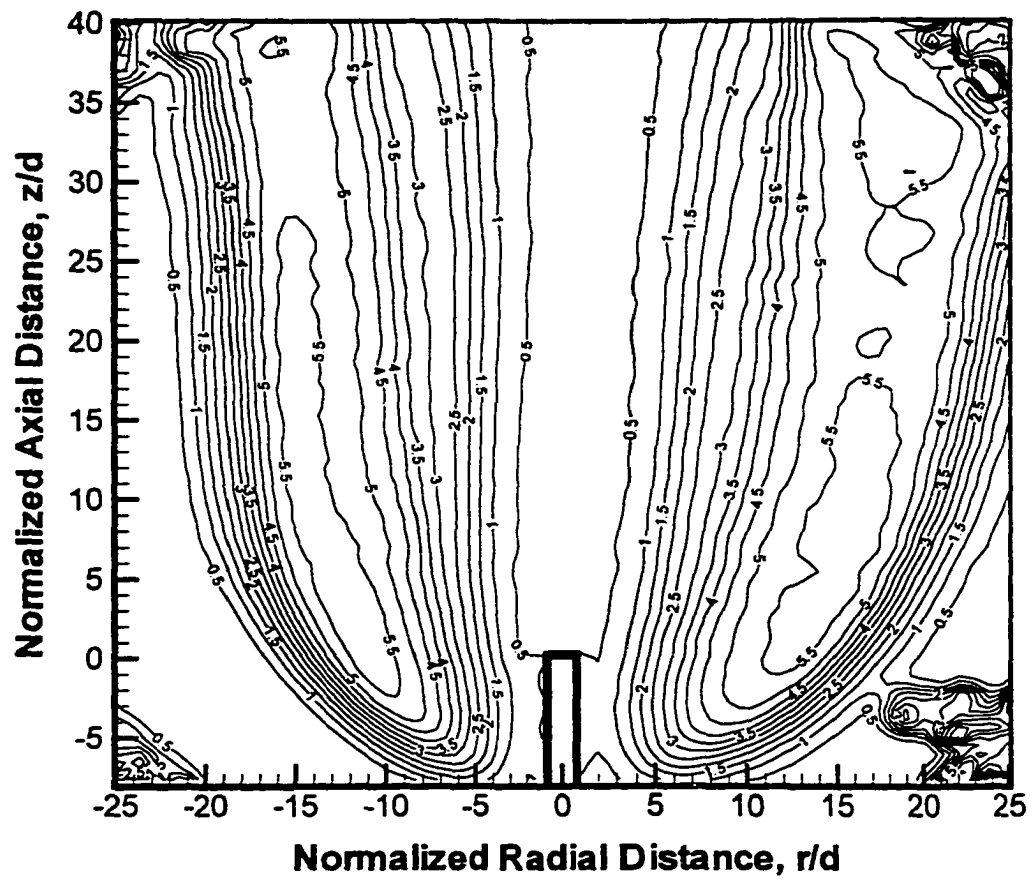


Figure 4.3.7: Contours of angular deflection in units of 10^{-4} radians;
 $Re = 70$, $d = 1.19$ mm, and $t = 1.01$ s

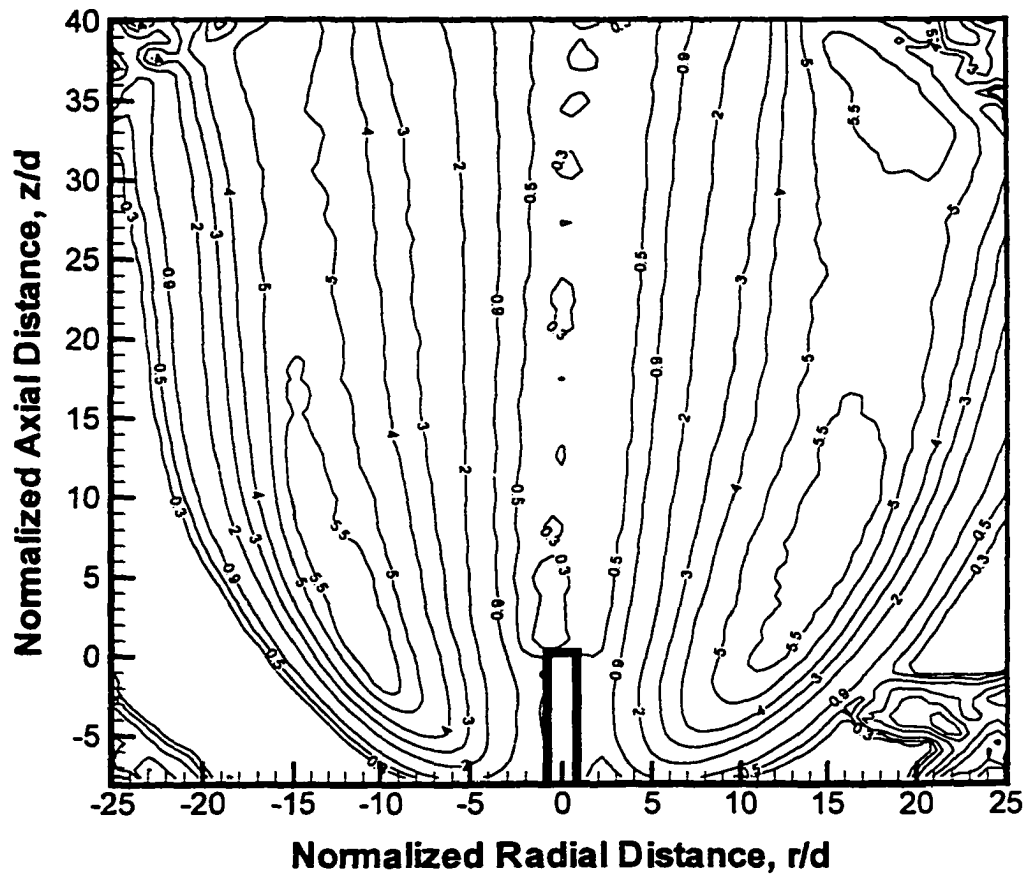


Figure 4.3.8: Contours of angular deflection in units of 10^{-4} radians;
 $Re = 70$, $d = 1.19$ mm, and $t = 1.25$ s

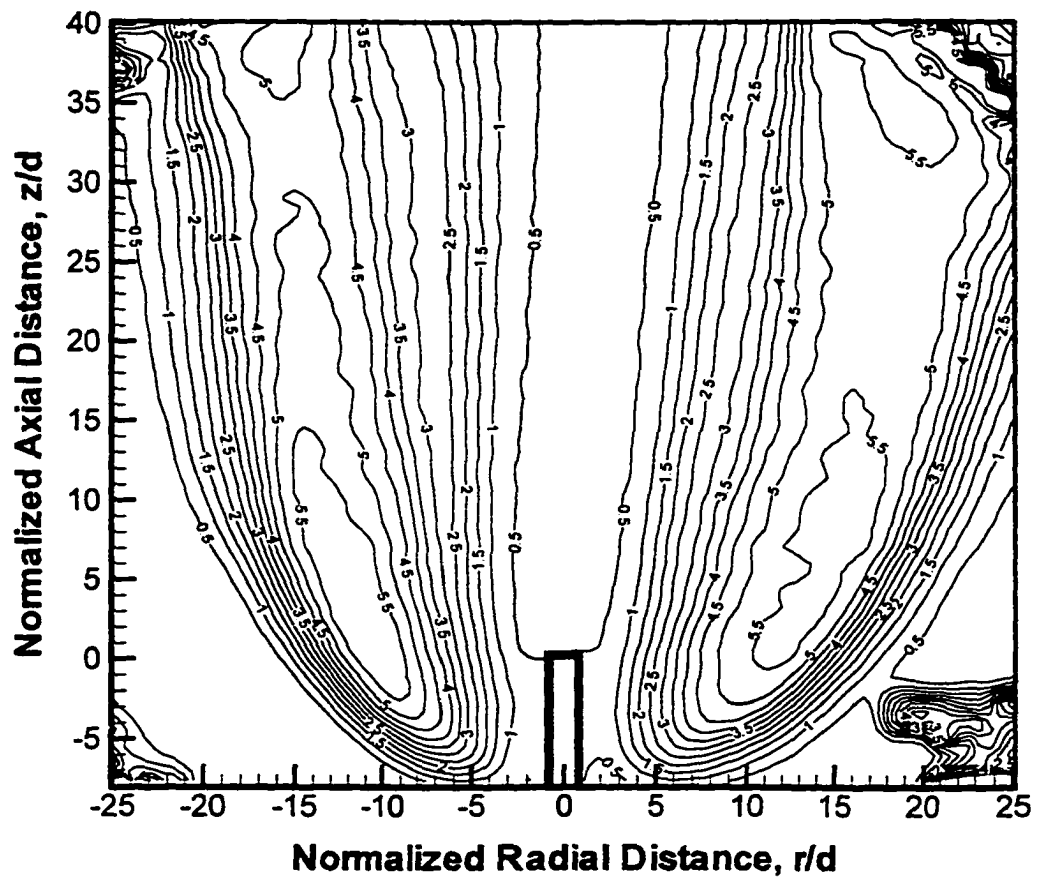


Figure 4.3.9: Contours of angular deflection in units of 10^{-4} radians;
 $Re = 70$, $d = 1.19$ mm, and $t = 1.47$ s

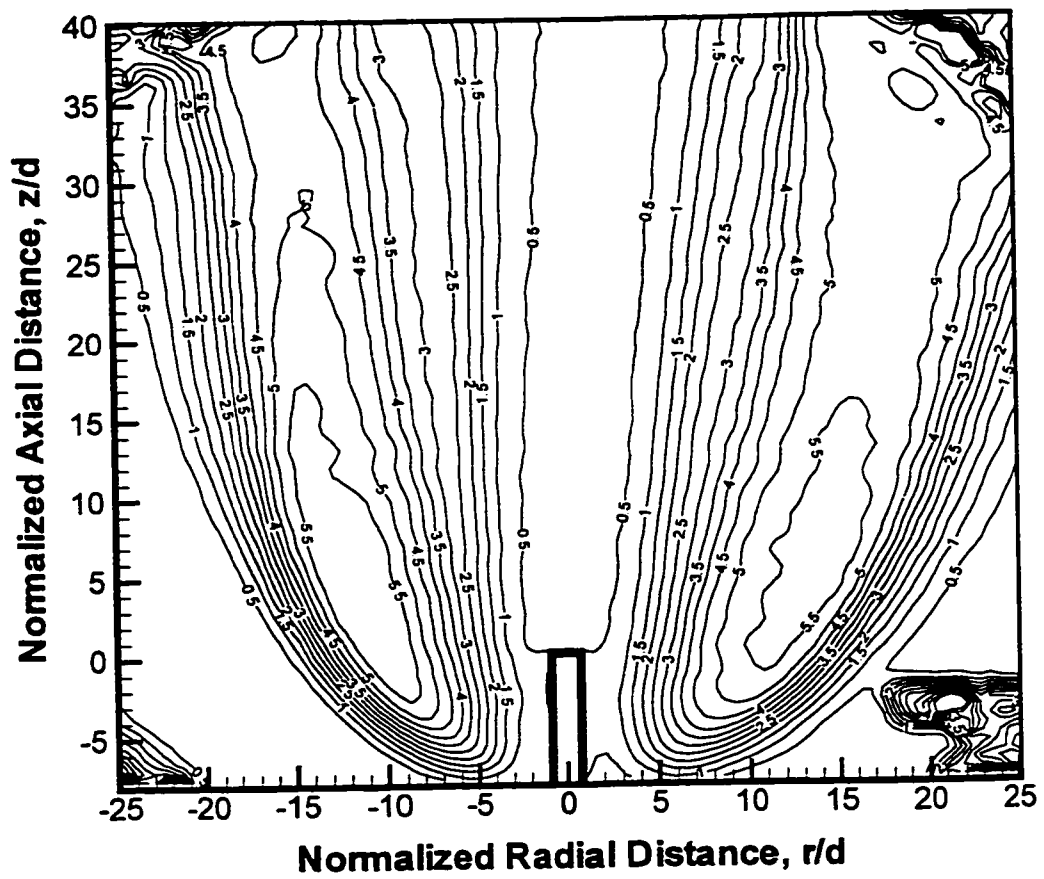


Figure 4.3.10: Contours of angular deflection in units of 10^{-4} radians;
 $Re = 70$, $d = 1.19$ mm, and $t = 1.62$ s

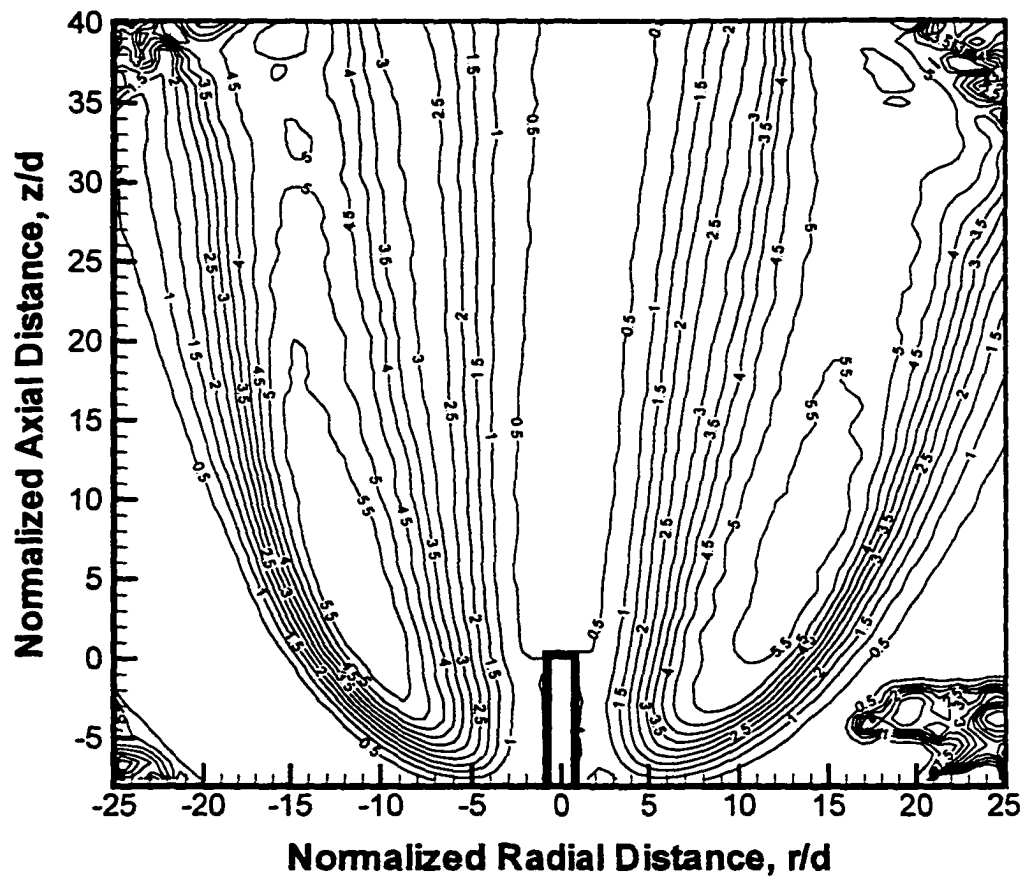


Figure 4.3.11: Contours of angular deflection in units of 10^{-4} radians;
 $Re = 70$, $d = 1.19$ mm, and $t = 1.82$ s

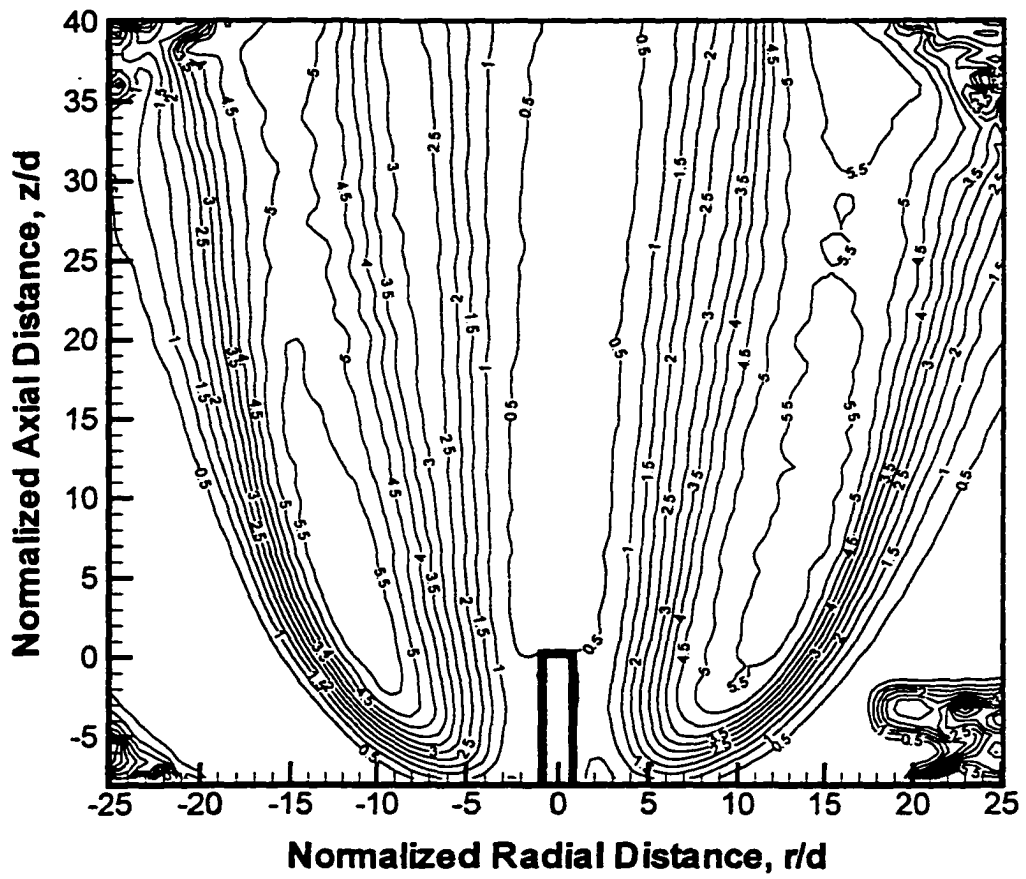


Figure 4.3.12: Contours of angular deflection in units of 10^{-4} radians;
 $Re = 70$, $d = 1.19$ mm, and $t = 1.95$ s

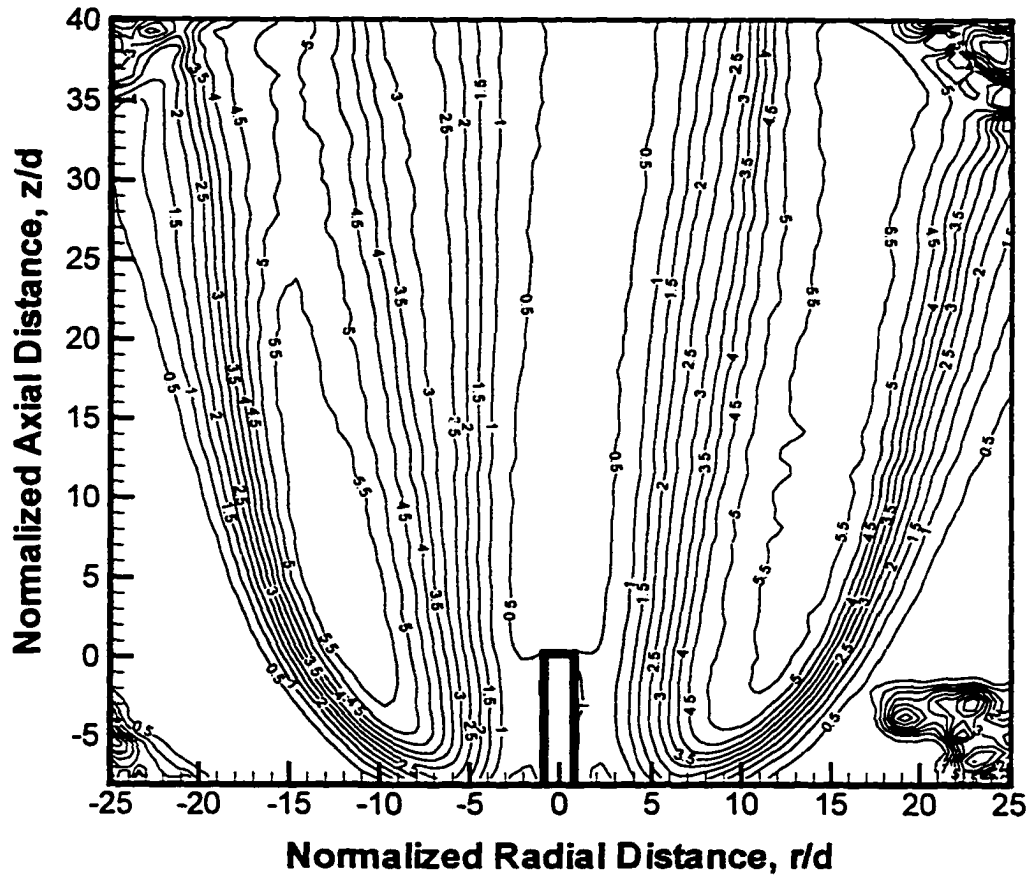


Figure 4.3.13: Contours of angular deflection in units of 10^{-4} radians;
 $Re = 70$, $d = 1.19$ mm, and $t = 2.14$ s

2.2-s drop tower. The analysis in the next sub-section utilized the schlieren image acquired at the end of the drop to represent microgravity conditions.

4.3.1.2 Scalar Profiles

The normalized refractive index difference at $z/d = 4$ in normal and microgravity flames is shown in Fig. 4.3.16. The radial extent of the refractive index profile in microgravity is about twice of that in normal gravity. Note that the minimum refractive index corresponds to the flame surface. The corresponding profile of oxygen mole fraction in Fig. 4.2.17 shows a similar relative radial expansion. Note that oxygen concentration is equal to zero in the fuel-rich region, which is consistent with the complete-reaction assumption in chemical equilibrium. The temperature profiles in Fig. 4.3.18 show that the flame temperature is the same in normal and microgravity. Again, smaller temperature gradient is evident in the outer regions of the microgravity flame. The oxygen mole fraction and temperature profiles at $z/d = 8$ are shown, respectively, in Figs. 4.3.19 and 4.3.20. Here, the overall trends are similar to those in Figs. 4.3.17 and 4.3.18. However, the radial extent of the flame has increased compared to that at $z/d = 4$. The profiles in microgravity are about twice as wide as they are in normal gravity.

4.3.1.3 Flame Shape

Although the scalar profiles presented above provide details for comparison with theoretical and computational models, most studies in microgravity has focused on the overall flame characteristics, e.g., the flame shape. In this sub-section, the flame

shape is compared in normal and microgravity. At an axial plane, the flame boundary was marked by the location of the minimum refractive index (maximum temperature). The flame shape in normal and microgravity is shown in Fig. 4.3.21. The flame shape was obtained using RSD data at several axial planes. Note the maximum flame width in microgravity is nearly twice of that in normal gravity. However, the flame height shows no measurable change with gravity. This observation agrees with theoretical predictions by Hegde and Bahadori (1992) and Roper (1977), and with experimental observations of Stoker (1990). Figure 4.3.21 also reveals that the flame diffuses further upstream of the burner in microgravity as compared to that in normal gravity. In microgravity, a lack of buoyancy induced acceleration near the jet exit allows hydrogen to diffuse further upstream.

4.3.2 Burner Diameter Effect

One of the objectives of this research was to study burner diameter effect on flame shape and scalar profiles in normal and microgravity. In this sub-section, the burner diameter effect on oxygen mole fraction and temperature profiles and on flame shape in normal and microgravity will be investigated.

A contour plot of angular deflection angle in normal gravity for a smaller burner ($d = 0.3$ mm) is shown in Fig. 4.3.22 for $Re = 70$. Note that the radial extent is twice of that in Fig. 4.3.2 for $d = 1.19$ mm. With a smaller diameter burner, the initial jet velocity increases, which enhances entrainment, resulting in relatively wider flow field. The corresponding angular deflection contour plot in microgravity is shown in

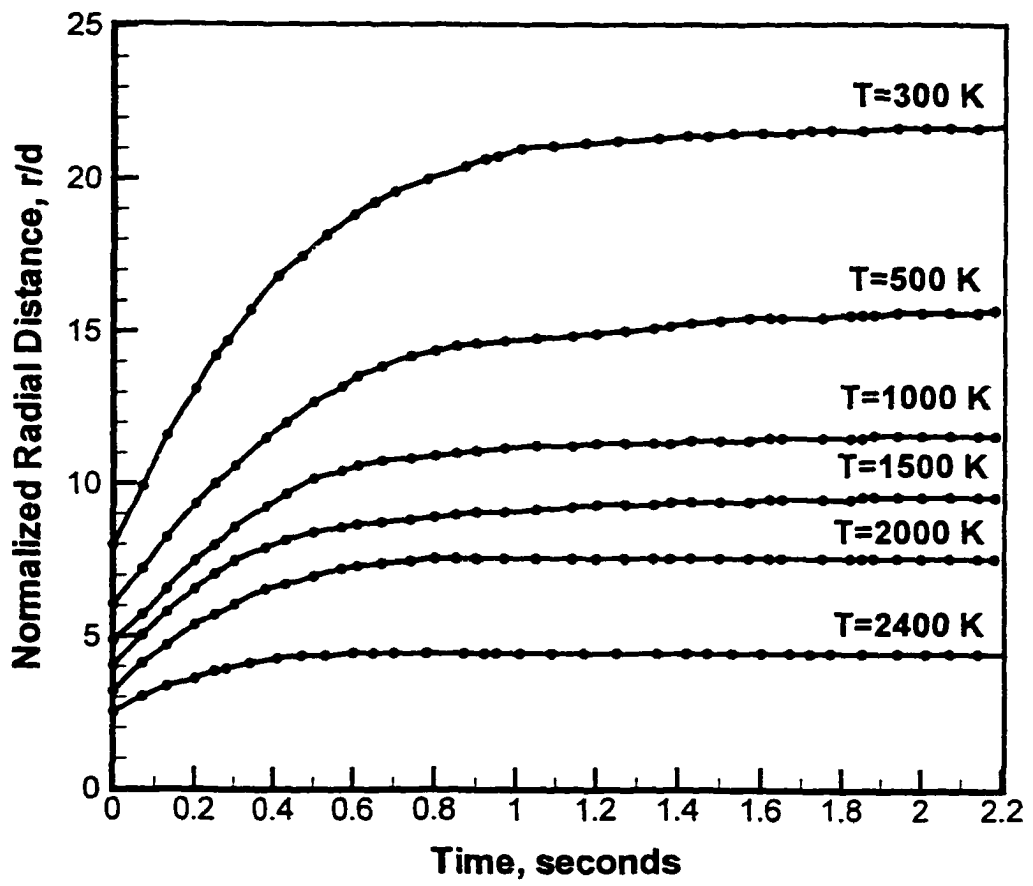


Figure 4.3.14: Temperature profiles during the drop; $z/d = 4$, $Re = 70$, and $d = 1.19$ mm

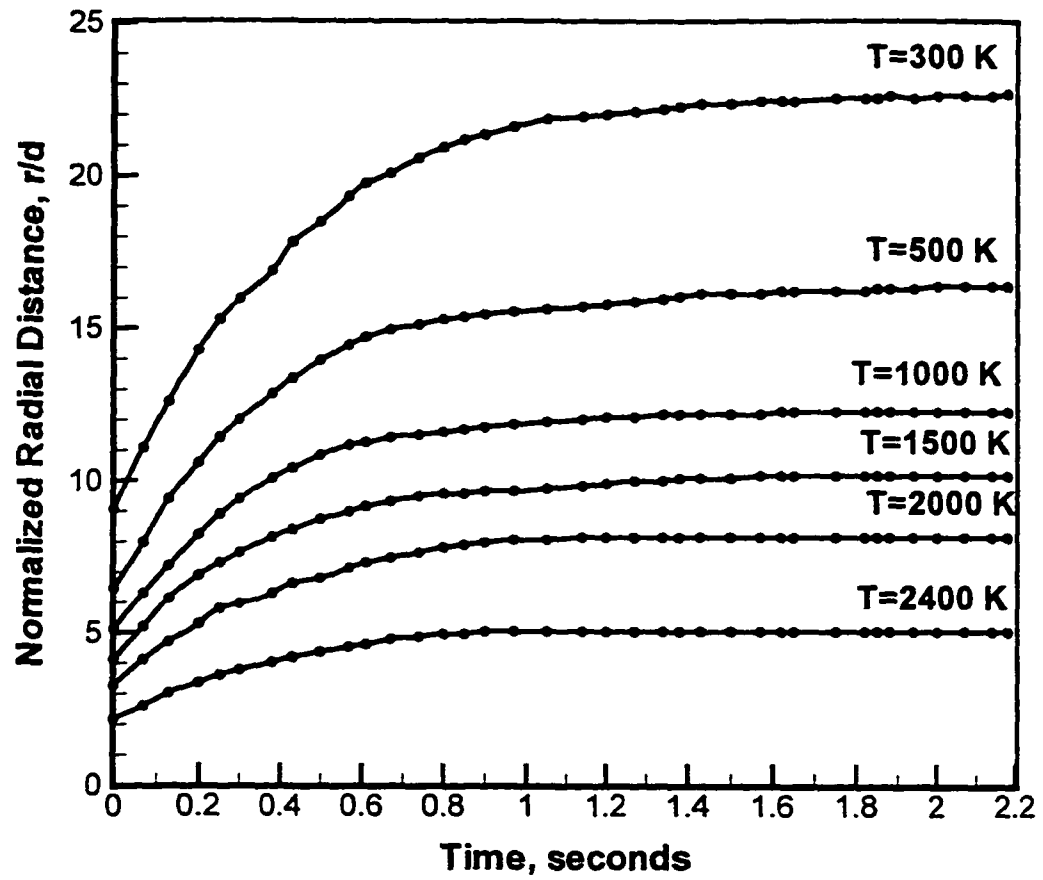


Figure 4.3.15: Temperature profiles during the drop; $z/d = 8$, $Re = 70$, and $d = 1.19$ mm

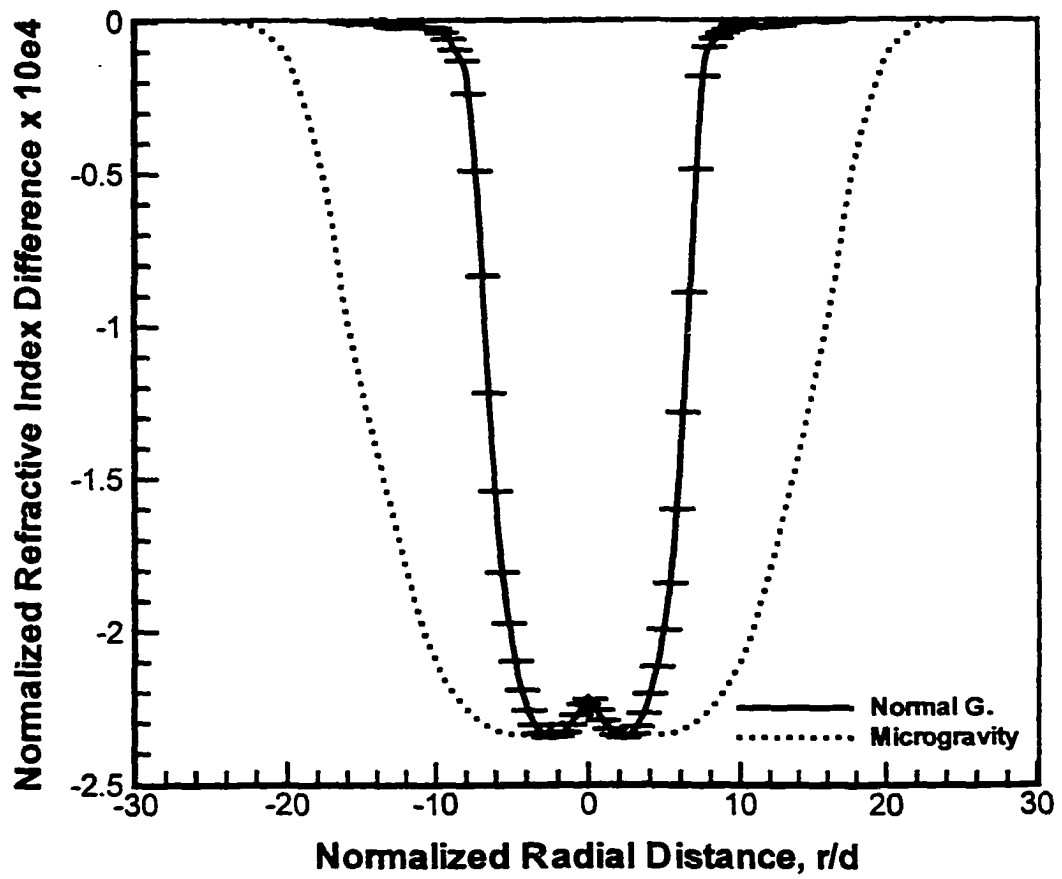


Figure 4.3.16: Buoyancy effects on normalized refractive index difference profiles; $Re = 70$, $d = 1.19$ mm, and $z/d = 4$

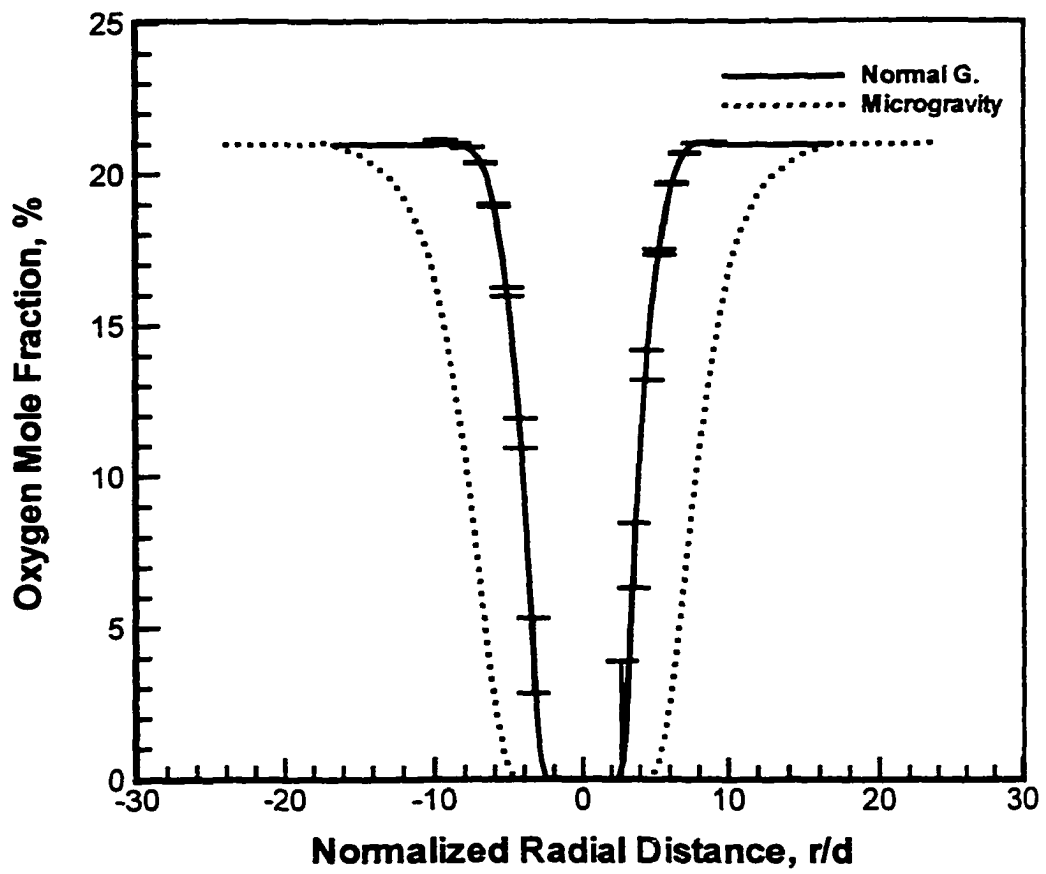


Figure 4.3.17: Buoyancy effects on oxygen mole fraction profiles;
 $Re = 70$, $d = 1.19$ mm, and $z/d = 4$

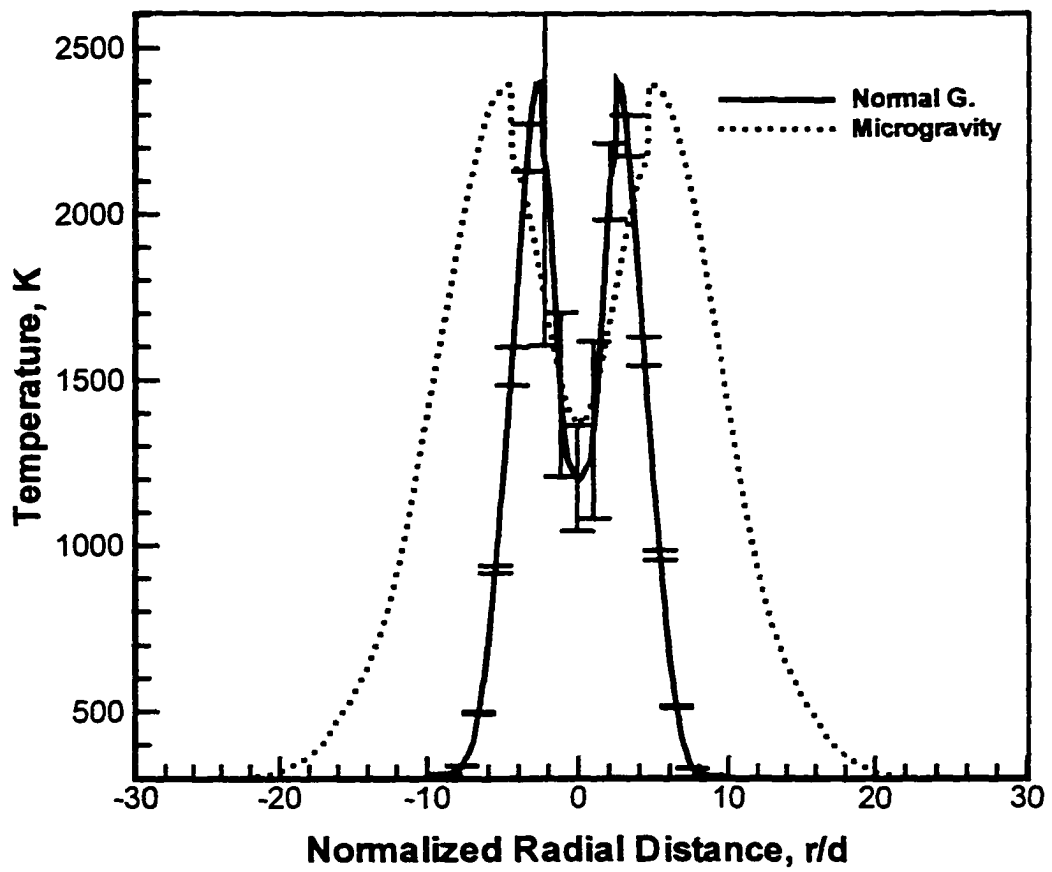


Figure 4.3.18: Buoyancy effects on temperature profiles; $Re = 70$, $d = 1.19$ mm, and $z/d = 4$

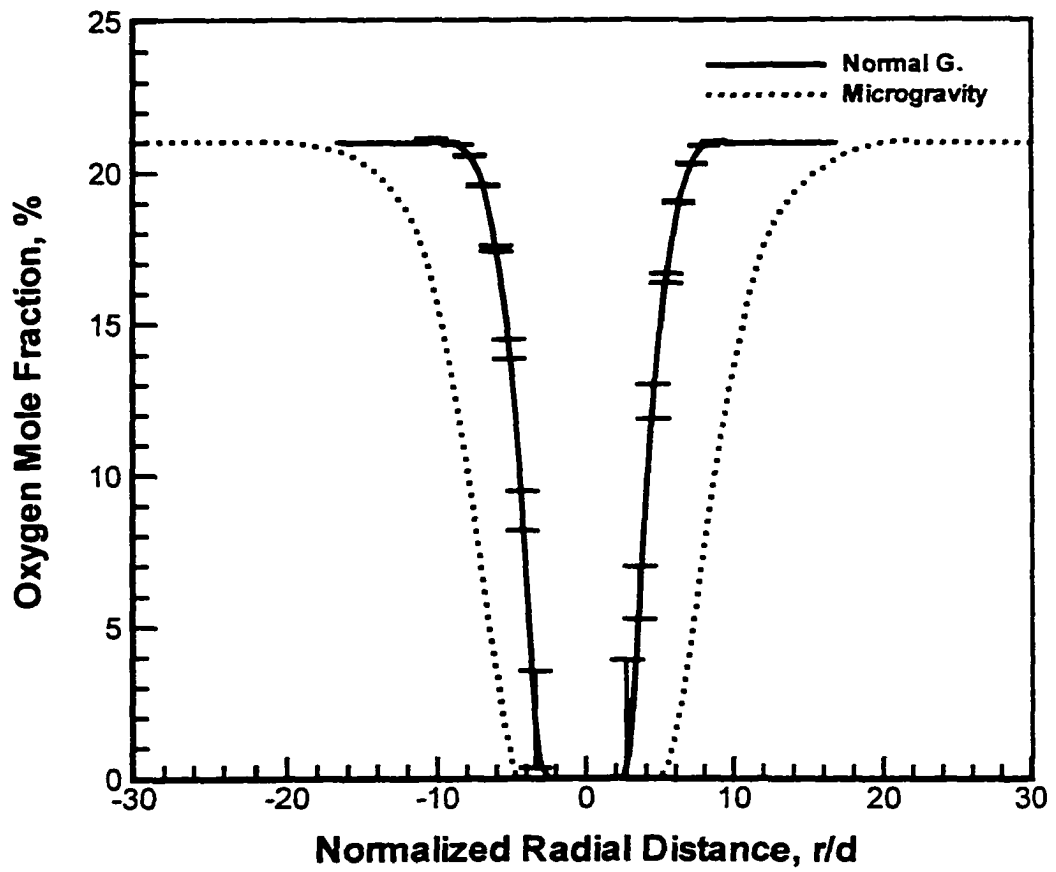


Figure 4.3.19: Buoyancy effects on oxygen mole fraction profiles;
 $Re = 70$, $d = 1.19$ mm, and $z/d = 8$

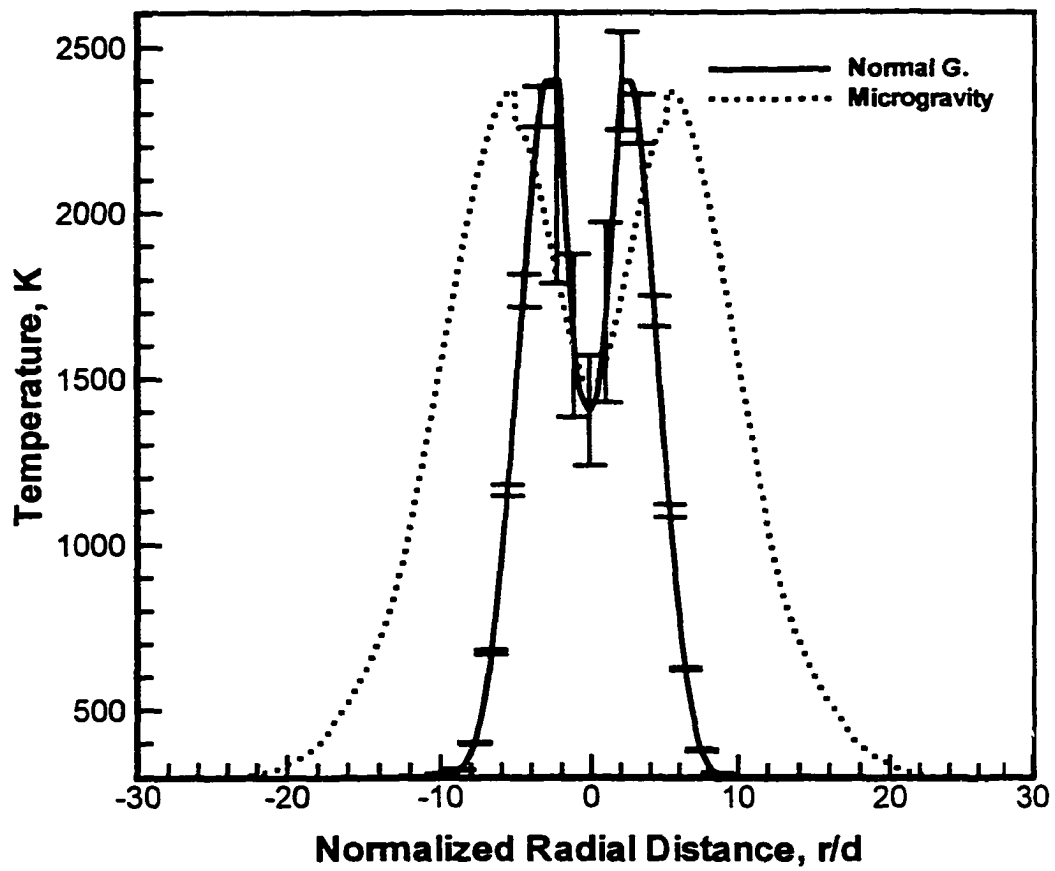


Figure 4.3.20: Buoyancy effects on temperature profiles; $Re = 70$, $d = 1.19$ mm, and $z/d = 8$

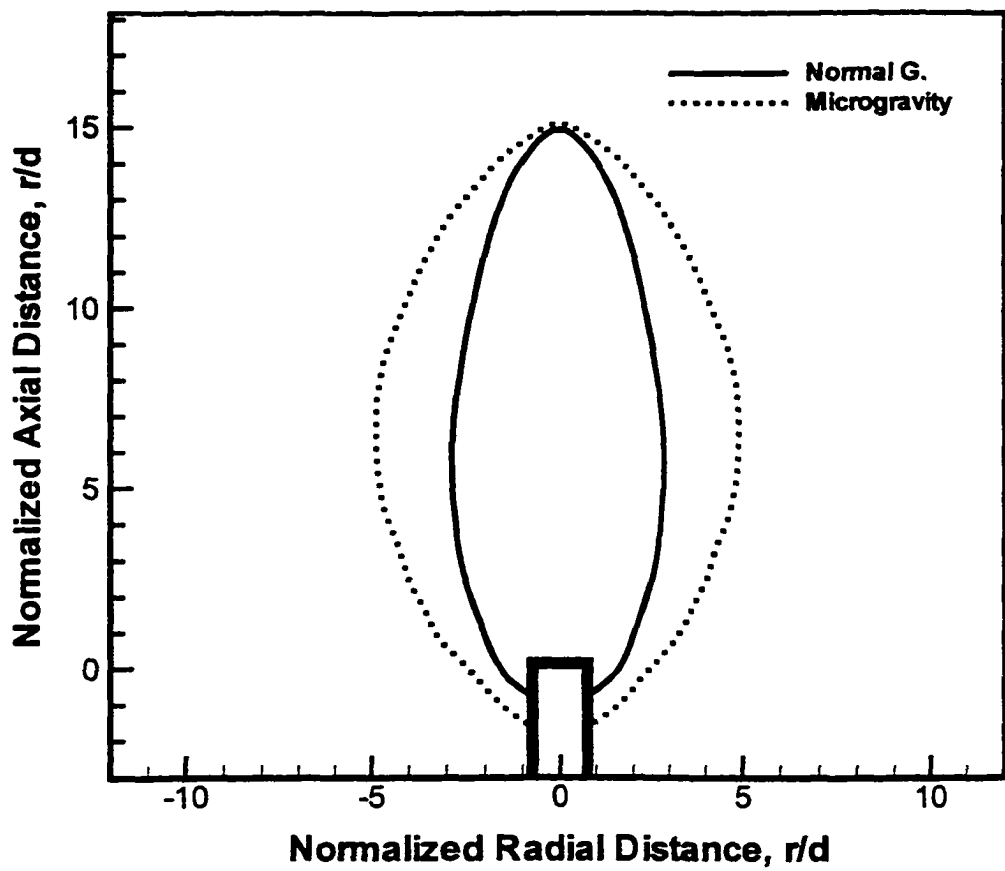


Figure 4.3.21: Buoyancy effect on flame shape; $Re = 70$ and $d = 1.19$ mm

Fig. 4.3.23. Again, in microgravity, the radial gradients are smaller and diffusion upstream of the burner exit is more significant.

The temperature profiles at $z/d = 4$ for the duration of the drop is shown in Fig. 4.3.24. Here, both the flame surface and schlieren boundary have reached near steady-state within 0.6 seconds in microgravity. Again, the time to reach steady-state is shorter for the flame surface than it is for the schlieren boundary. Note that the jet exit velocity in the smaller diameter burner ($d = 0.3$ mm) is 4 times higher than that in the larger diameter burner ($d = 1.19$ mm). Higher jet exit velocity results in larger Froude number (ratio of the jet inertia and buoyancy force) and hence, less buoyancy effects. This is why the temperature profiles with the smaller burner reached near steady-state condition faster than the ones with the larger burner. The observation that flames with higher jet exit velocity reach steady-state earlier than those with lower velocity jets agrees with the experimental results of Cochran and Masica (1971). Similar trends are observed in Fig. 4.3.25, which shows the temperature profiles at $z/d = 8$. The primary difference is that the profiles have diffused further in the radial direction. This is expected because the flame widens at the downstream location.

The effect of burner diameter on oxygen mole fraction profiles in normal and microgravity is shown in Fig.4.3.26. The Froude number in normal gravity for $d = 1.19$ mm is roughly 3.9, and for $d = 0.3$ mm, it is about 61. The ratio of the two Froude numbers is about 16. In microgravity, the Froude number is very large because the gravitational acceleration is on the order of 10^{-6} g. In Fig. 4.3.26, it is shown that the oxygen mole fraction profiles in microgravity are within experimental

uncertainty from each other. Because the Froude number is large in microgravity, the flame characteristics are determined only by the Reynolds number, which is the same for the profiles in Fig. 4.3.26. In contrast, the Reynolds number does not uniquely characterize the oxygen mole fraction profiles in normal gravity and hence, profiles are different for the two burners. Similar conclusions are drawn from the temperature profiles shown in Fig. 4.3.27. These conclusions are reinforced by the oxygen mole fraction and temperature profiles at $z/d = 8$ shown in Figs. 4.3.28 and 4.3.29.

The flame shape at $Re = 70$ in normal and microgravity is shown in Fig. 4.3.30. Again, because the Froude number is large, the normalized flame surface in microgravity is independent of the burner diameter. This observation was predicted theoretically by equation (2.10) in Chapter 2. In contrast, the normalized flame surface in normal gravity is affected by the burner diameter because of the Froude number effects.

Next, the burner diameter effect on flame characteristics is described for a smaller Reynolds number of 40. Again, measurements of deflection angle, temporal evolution in the drop tower, oxygen mole fraction, temperature, and flame shape are presented for $d = 0.3$ mm and 1.19 mm.

Figure 4.3.31 shows the deflection angle contours in normal gravity for $d = 1.19$ mm. Evidently, the radial extent of the angular deflection is smaller than that at the higher Reynolds number (Fig. 4.3.2). This is because of the higher jet exit velocity at higher Reynolds number, increases the entrainment. Similar trends are observed in microgravity (Fig. 4.3.32), although some flow asymmetry because of disturbance during the drop is apparent. Figures 4.3.33 and 4.3.34 show angular

deflection contours for $d = 0.3$ mm. Note that the radial extent of angular deflection contours has increased because of the higher jet exit velocity compared to that for $d = 1.19$ mm.

Figures 4.3.35 and 4.3.36 show the temporal evolution of temperature profiles, respectively, at $z/d = 4$ and 8 for $d = 1.19$ mm. The flame surface and higher temperature regions are shown to reach steady-state earlier than the lower temperature regions. The schlieren boundary ($T = 300$ K) does not appear to have reached steady-state in the 2.2-s drop period. Also, the radial extent is less than that in the larger Reynolds number case (Fig.'s 4.3.14 and 4.3.15). This difference is caused by the increased jet exit velocity and hence, high entrainment at the larger Reynolds number. The temporal evolution of temperature profiles in microgravity for $d = 0.3$ mm is depicted in Figs. 4.3.37 and 4.3.38. These profiles show that steady-state condition was reached during the drop. In this case, the radial extent of temperature profiles above 1000 K is smaller at $z/d = 8$ compared to that at $z/d = 4$. This is because the axial plane, $z/d = 8$ is close to the flame tip, where the flame converges toward the axis of symmetry. In fact, $z/d = 8$ is slightly above the flame tip. This explains why the profile at the flame temperature of 2400 K is not shown in Fig. 4.3.38.

Next, the oxygen mole fraction and temperature profiles in normal and microgravity at $z/d = 4$ and $Re = 40$ are shown, respectively, in Figs. 4.3.39 and 4.3.40. In microgravity, the profiles are independent of the burner diameter when normalized by the diameter. However, the effect of burner diameter is apparent in normal gravity. Similar conclusion is reached from Figs. 4.3.41 and 4.3.42, which

show, respectively, the oxygen mole fraction and temperature profiles at $z/d = 8$. Because $z/d = 8$ is slightly above the flame tip, some oxygen is present near the centerline. The temperature distribution at this axial plane shows a parabolic profile typical of the post-flame region.

Effect of burner diameter on flame shape in normal and microgravity at $Re = 40$ is shown in Fig. 4.3.43. As shown previously in Fig. 4.3.30, the normalized flame shape in microgravity is independent of the burner diameter. In normal gravity, the flame shape depends on the burner diameter. Moreover, the flame height is independent of the gravity.

4.3.3 Scaling with Reynolds Number

Theoretical predictions by Cochran and Masica (1971), Roper (1977), Spalding (1979), and others have shown that the flame height varies linearly with jet exit Reynolds number. In this sub-section, analysis of the results presented earlier by scaling the streamwise coordinate with the flame height is presented.

The scaled profiles of oxygen mole fraction and temperature are shown, respectively, in Figs. 4.3.44 and 4.3.45 for $d = 1.19$ mm. The profiles for $Re = 70$ are shown at $z/d = 4$ and for $Re = 40$ at $z/d = 2.3$ or $4 \cdot \frac{40}{70}$. Evidently, the profiles in normal and microgravity are independent of the Reynolds number when normalized in the manner shown, i.e., by scaling the axial distance with Reynolds number. A similar conclusion is drawn from Figs. 4.3.46 and 4.3.47, where the scalar profiles are shown for $d = 0.3$ mm. In this case, however, the normal and microgravity profiles

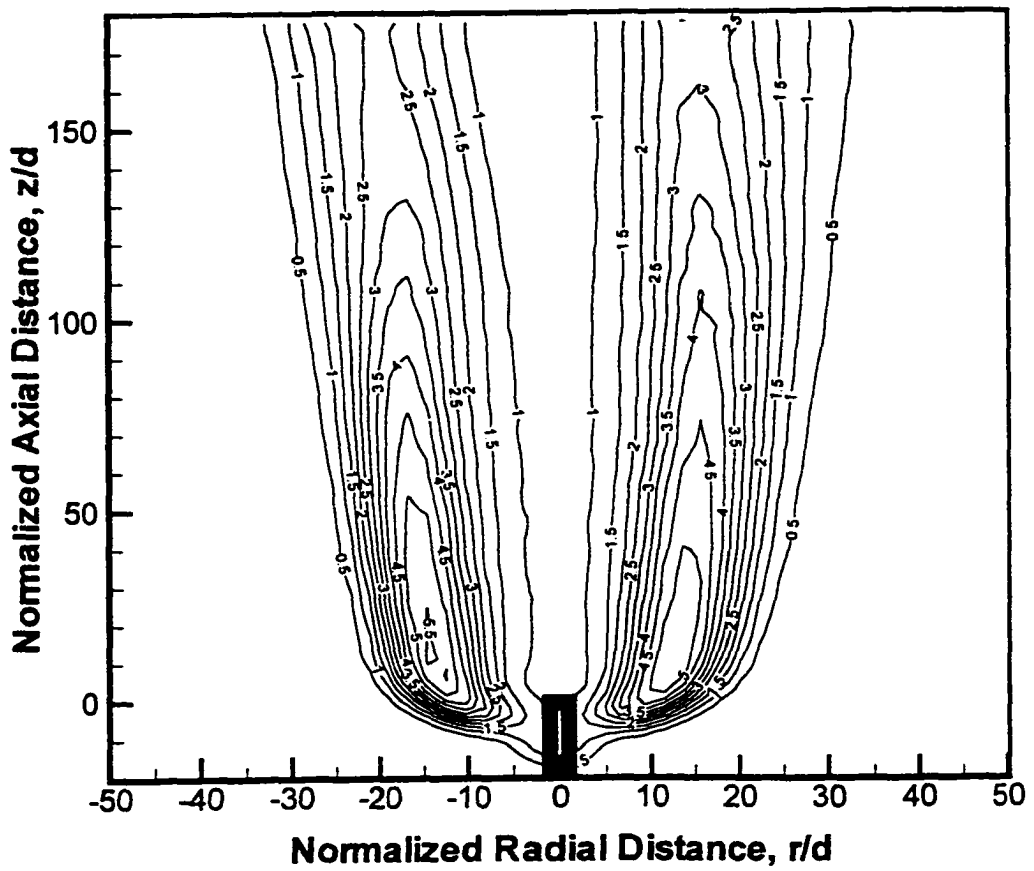


Figure 4.3.22: Contours of angular deflection in units of 10^{-4} radians in normal gravity; $Re = 70$ and $d = 0.3$ mm

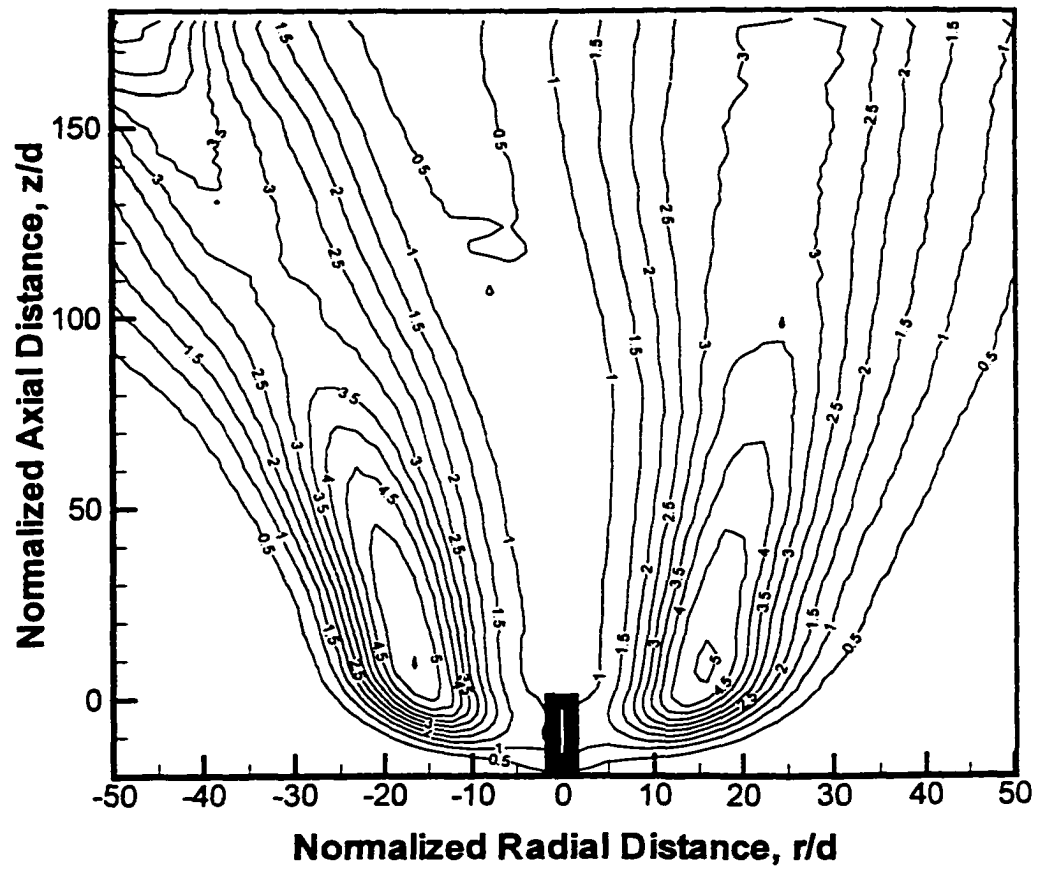


Figure 4.3.23: Contours of angular deflection in units of 10^{-4} radians in microgravity; $Re = 70$ and $d = 0.3$ mm

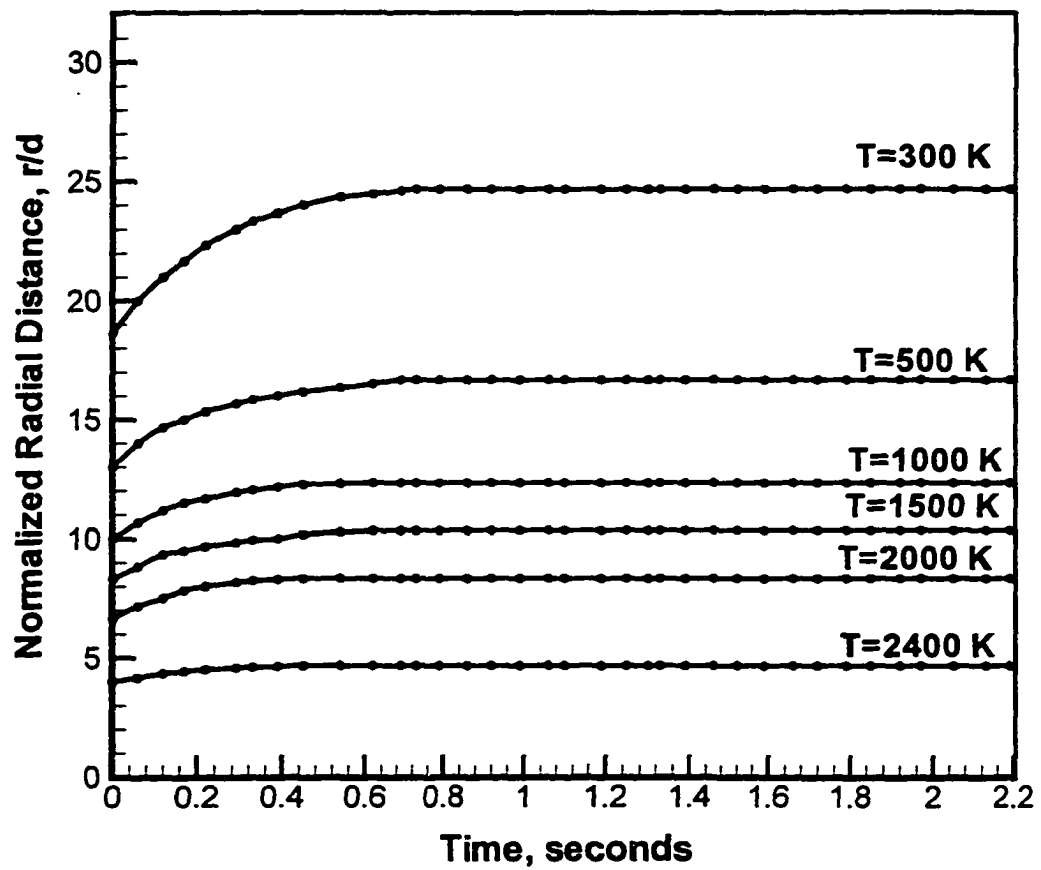


Figure 4.3.24: Temperature profiles during the drop; $z/d = 4$, $Re = 70$, and $d = 0.3$ mm

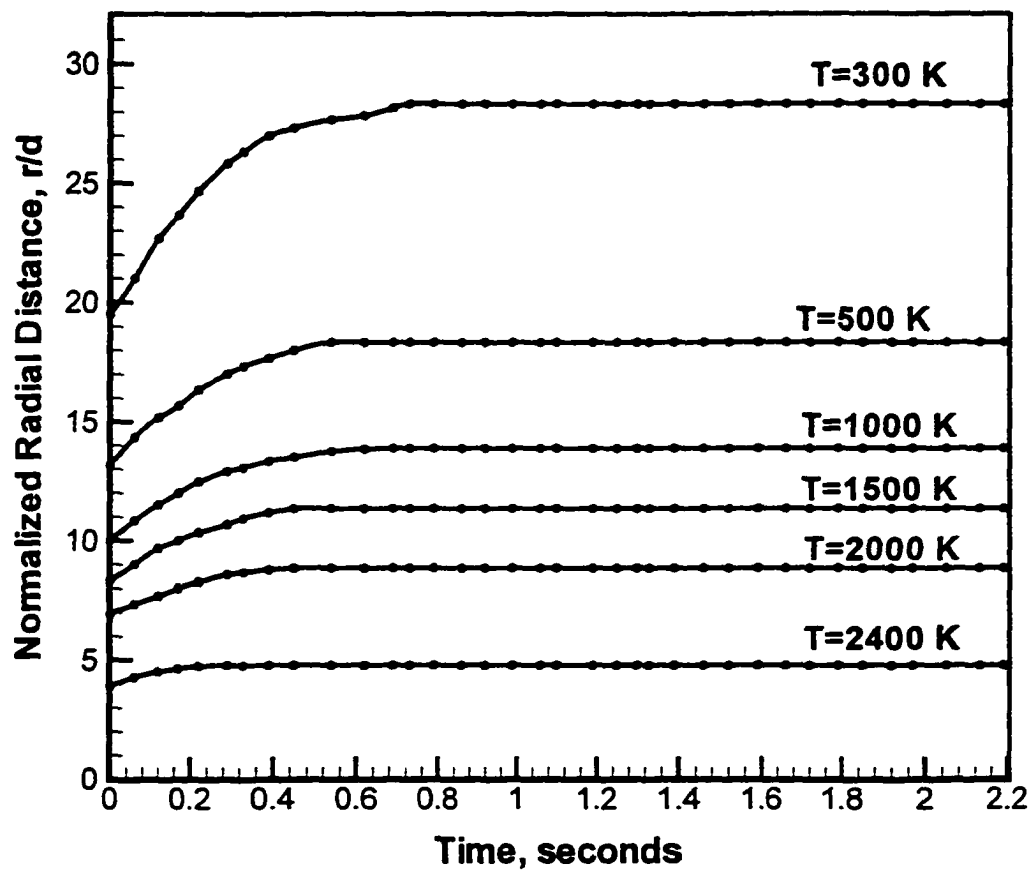


Figure 4.3.25: Temperature profiles during the drop; $z/d = 8$, $Re = 70$, and $d = 0.3$ mm

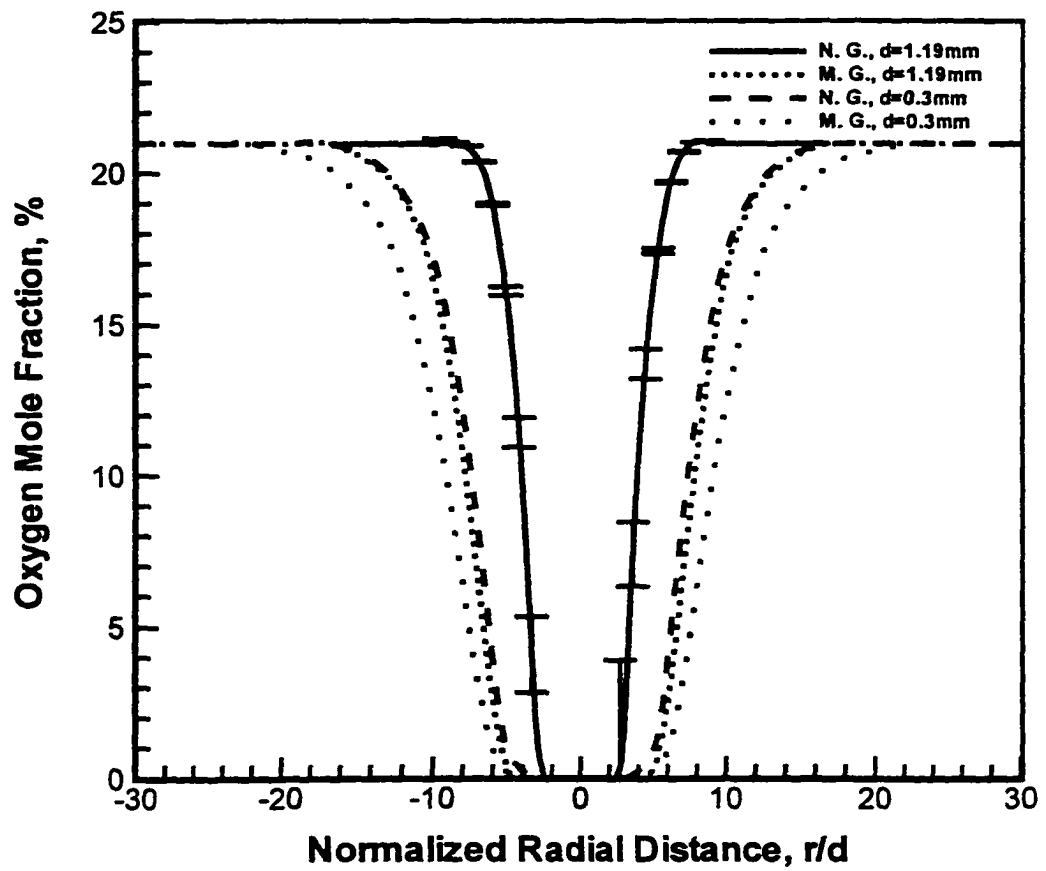


Figure 4.3.26: Burner diameter effect on oxygen mole fraction profiles in normal and microgravity; $Re = 70$ and $z/d = 4$

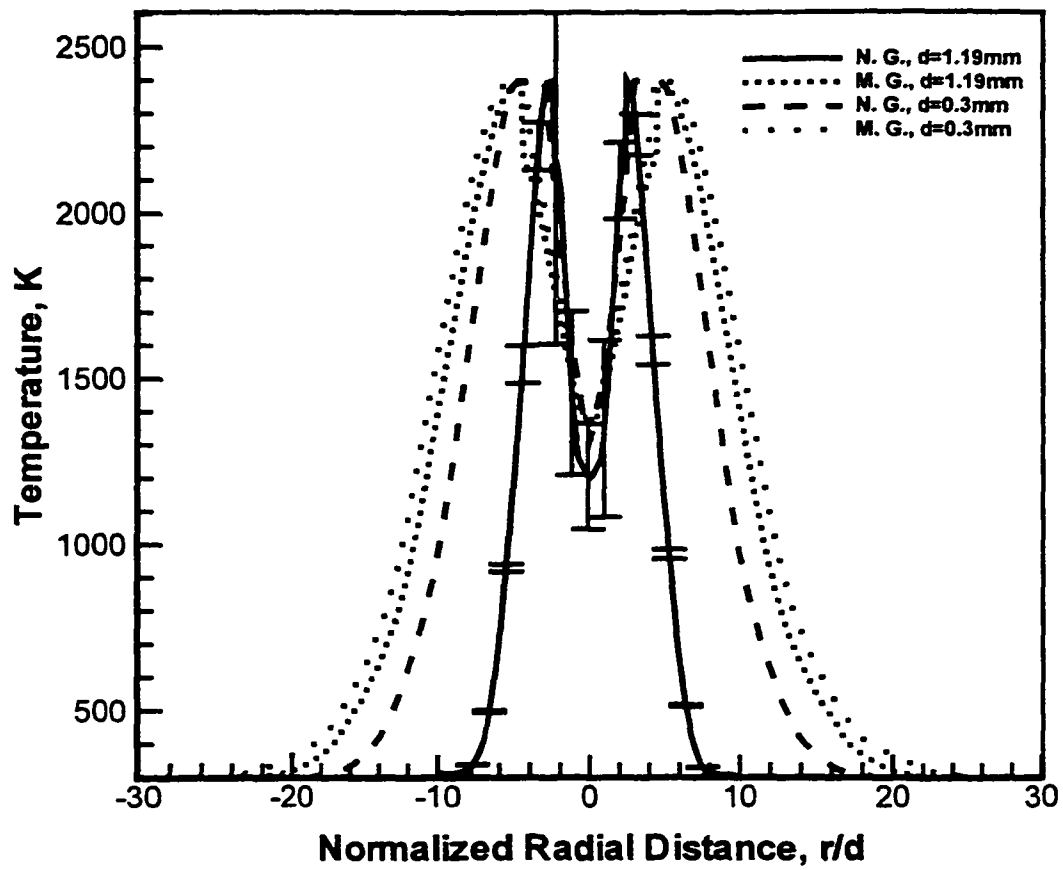


Figure 4.3.27: Burner diameter effect on temperature profiles in normal and microgravity; $Re = 70$ and $z/d = 4$

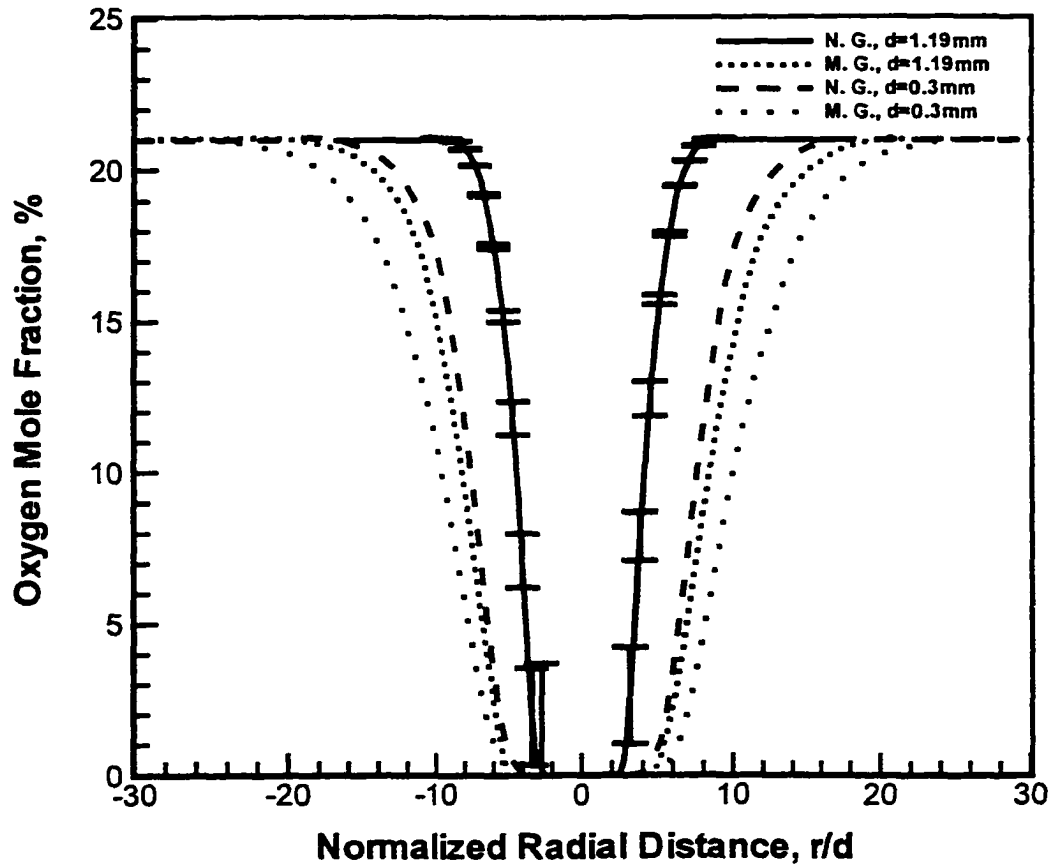


Figure 4.3.28: Burner diameter effect on oxygen mole fraction profiles in normal and microgravity; $Re = 70$ and $z/d = 8$

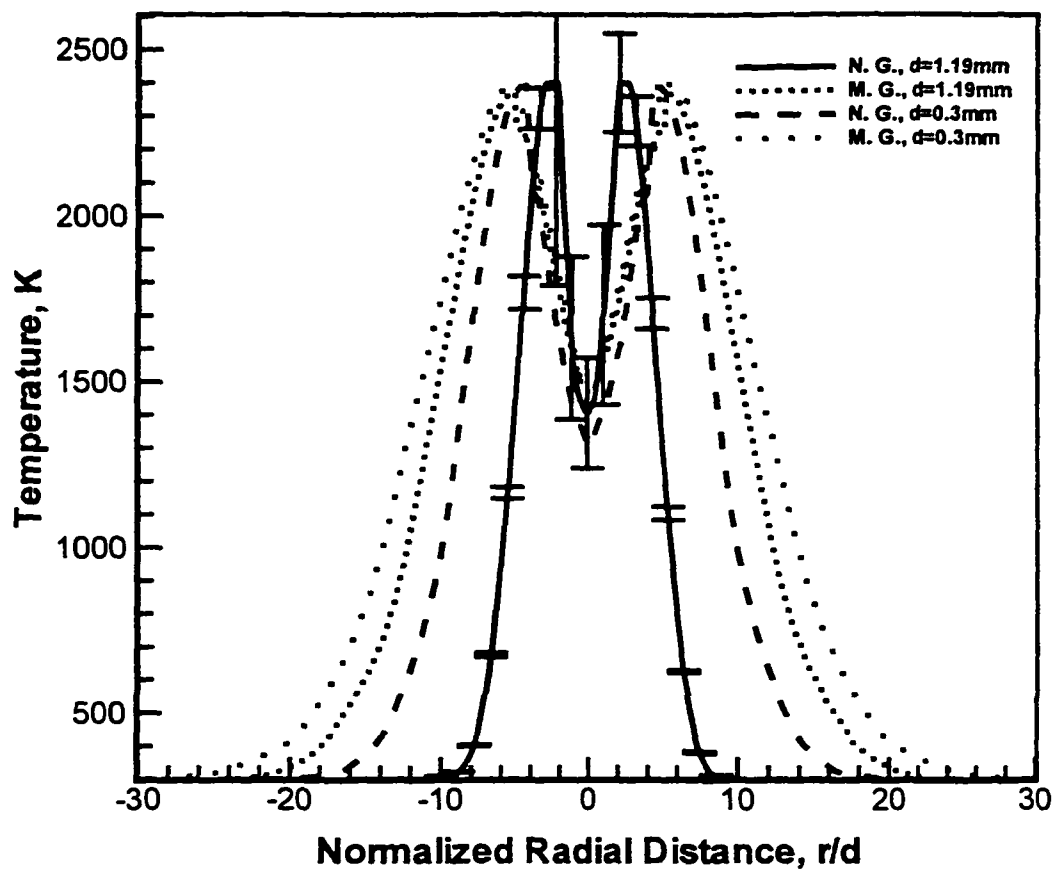


Figure 4.3.29: Burner diameter effect on temperature profiles in normal and microgravity; $Re = 70$ and $z/d = 8$

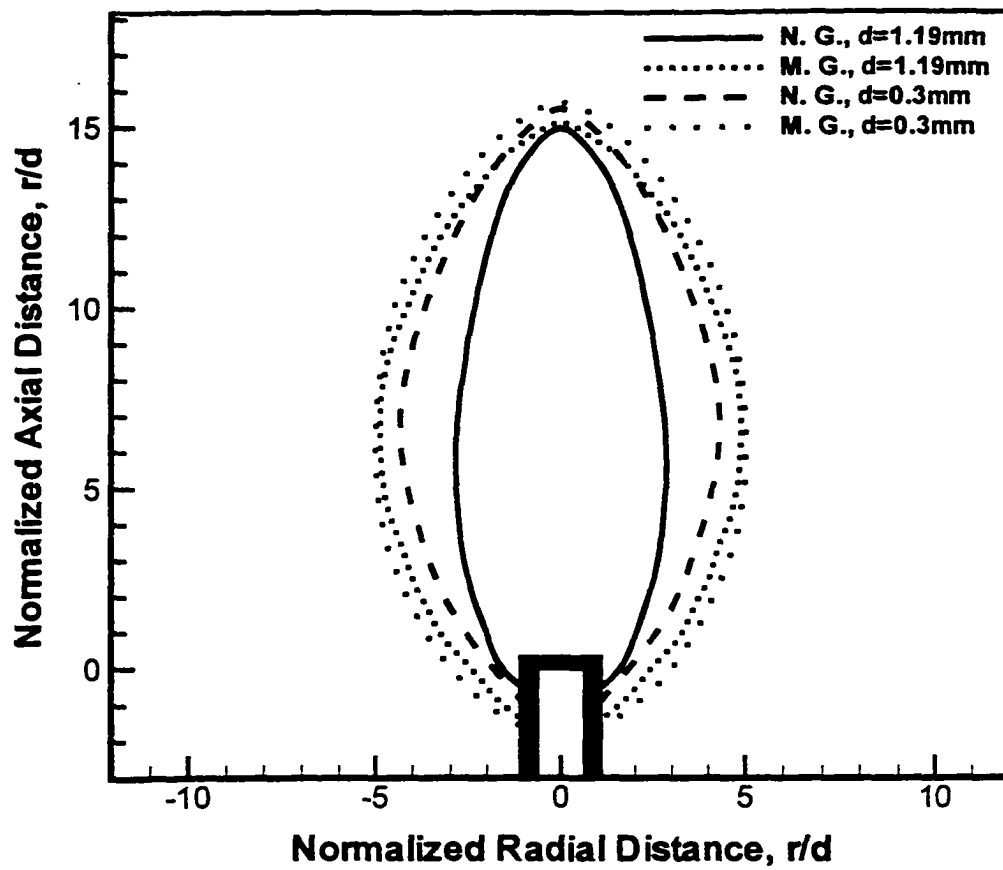


Figure 4.3.30: Burner diameter effect on flame shape in normal and microgravity; $Re = 70$

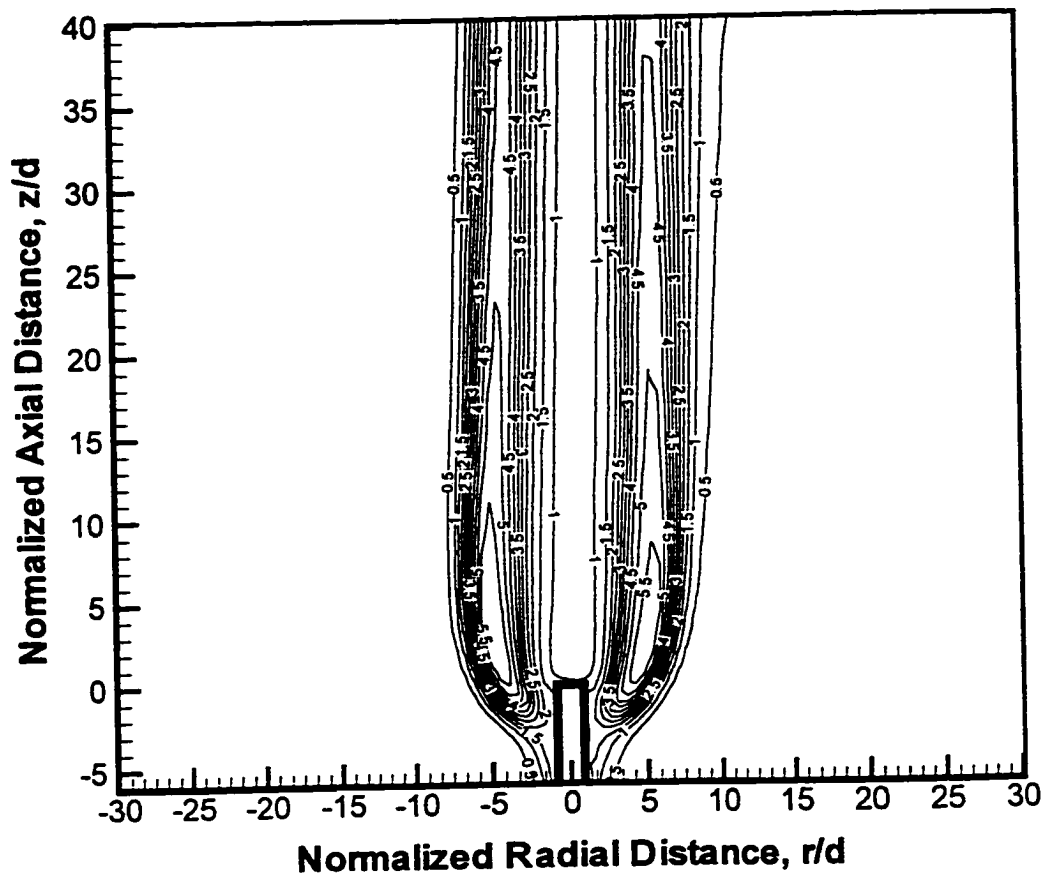


Figure 4.3.31: Contours of angular deflection in units of 10^{-4} radians in normal gravity; $Re = 40$ and $d = 1.19$ mm

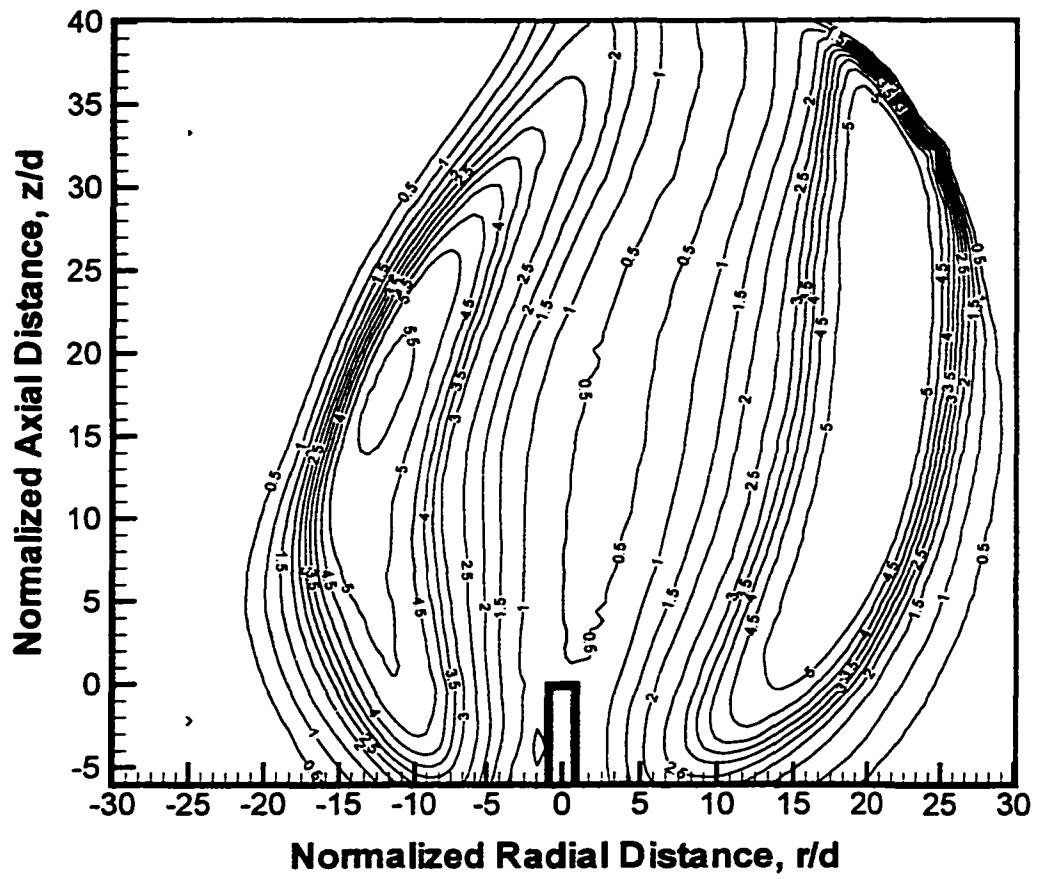


Figure 4.3.32: Contours of angular deflection in units of 10^{-4} radians in microgravity; $Re = 40$ and $d = 1.19$ mm

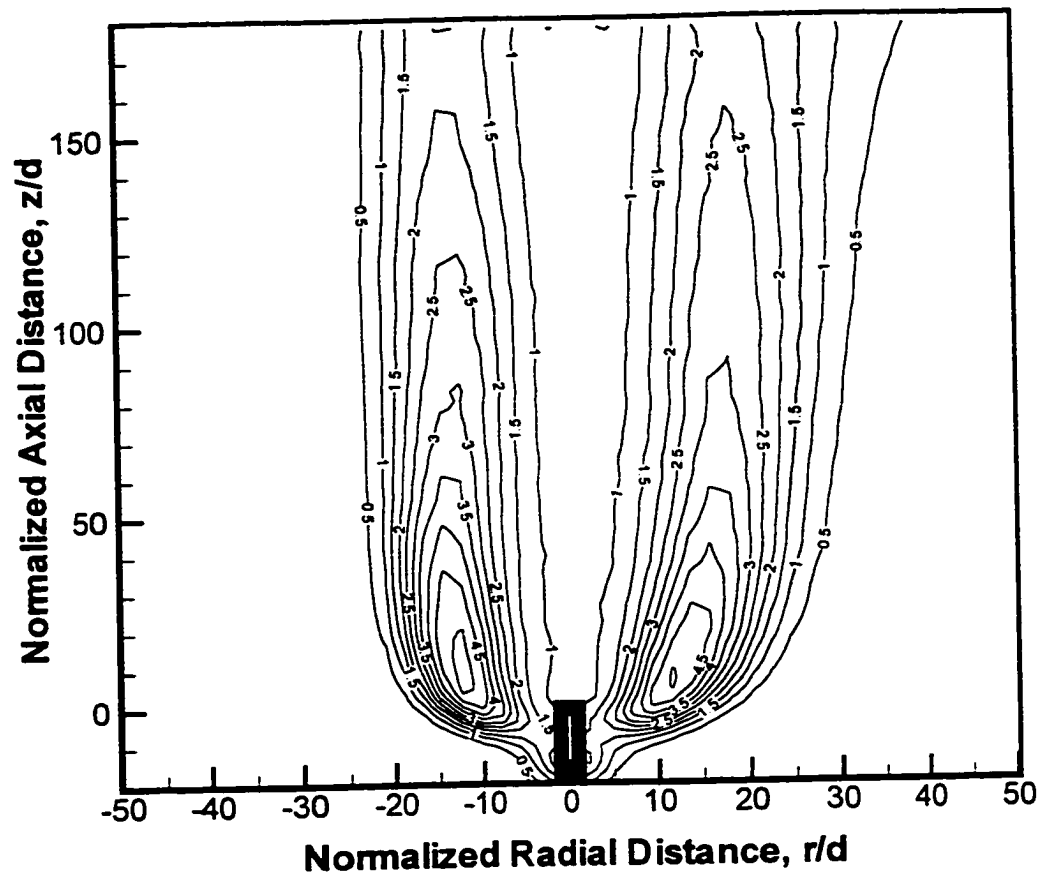


Figure 4.3.33: Contours of angular deflection in units of 10^{-4} radians in normal gravity; $Re = 40$ and $d = 0.3$ mm

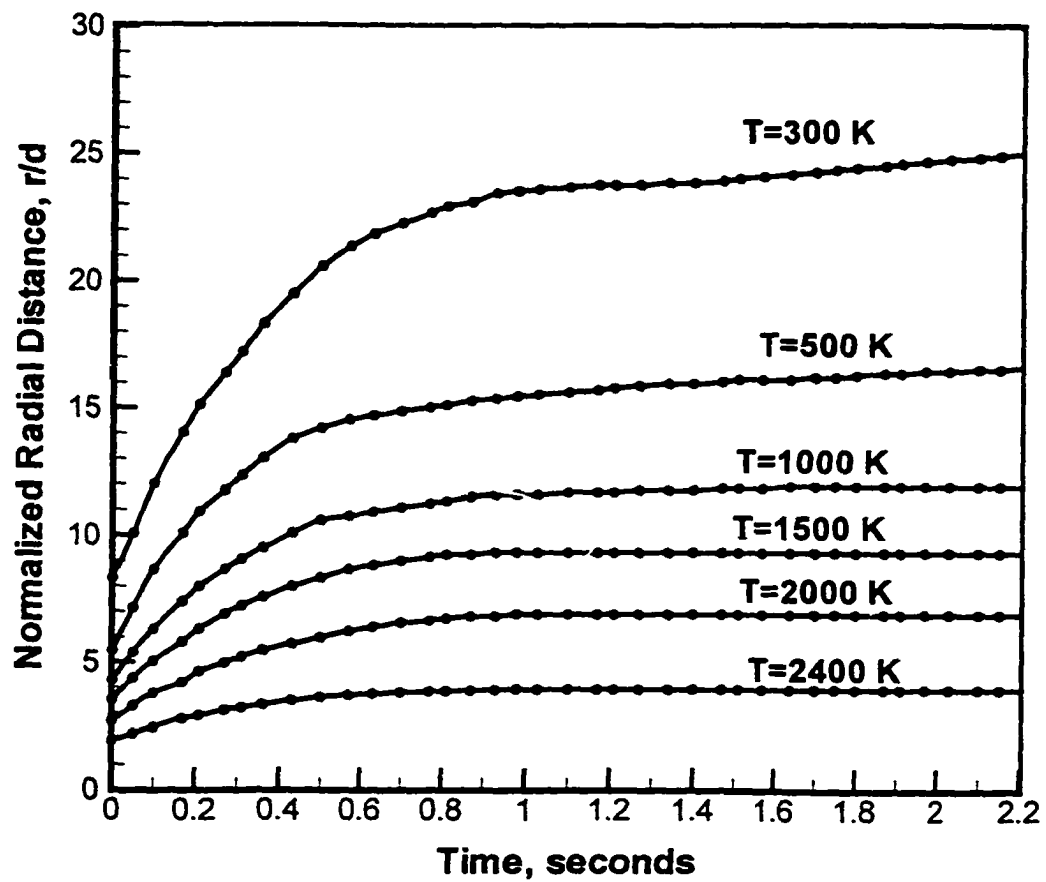


Figure 4.3.35: Temperature profiles during the drop; $z/d = 4$, $Re = 40$, and $d = 1.19$ mm

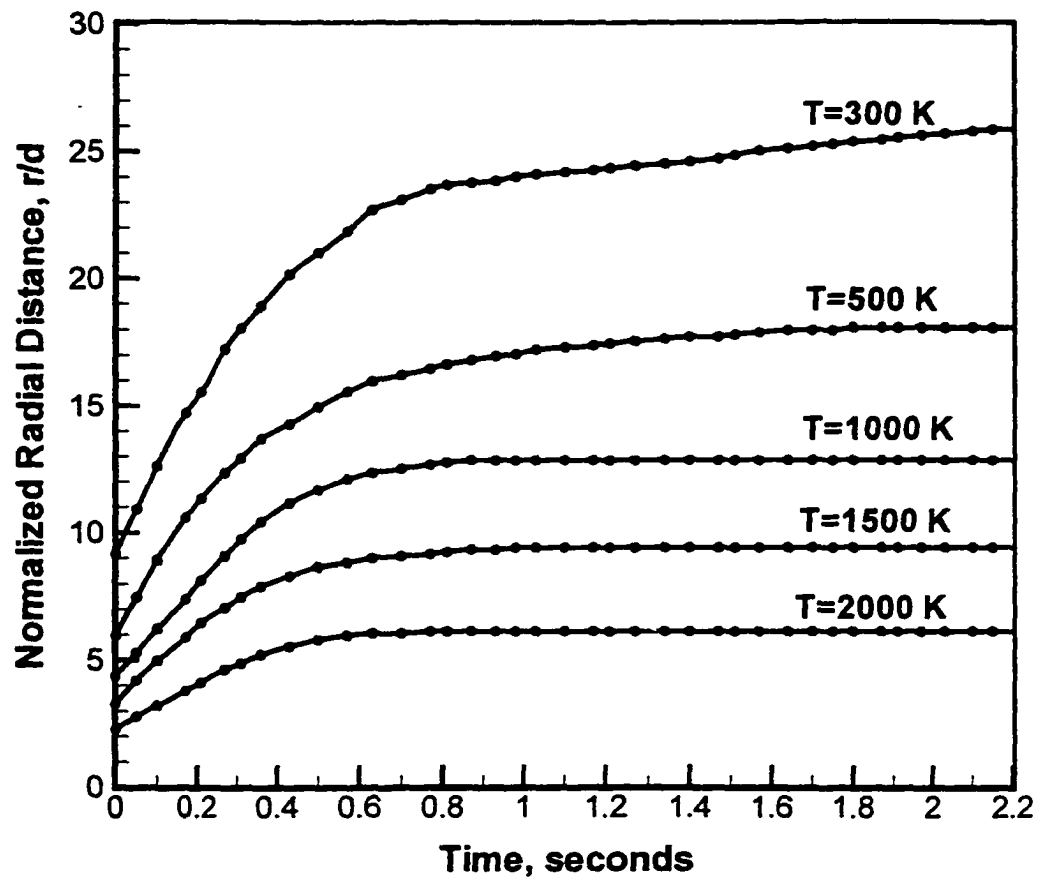


Figure 4.3.36: Temperature profiles during the drop; $z/d = 8$, $Re = 40$, and $d = 1.19$ mm

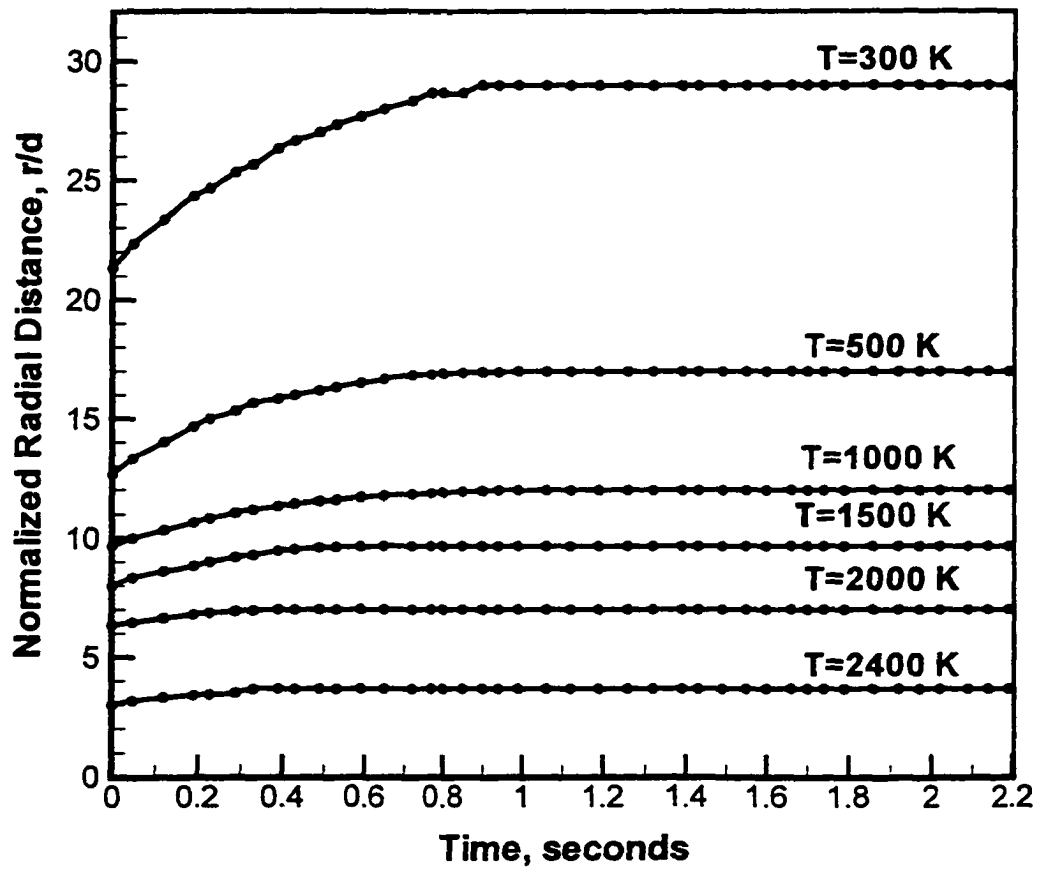


Figure 4.3.37: Temperature profiles during the drop; $z/d = 4$, $Re = 40$, and $d = 0.3$ mm

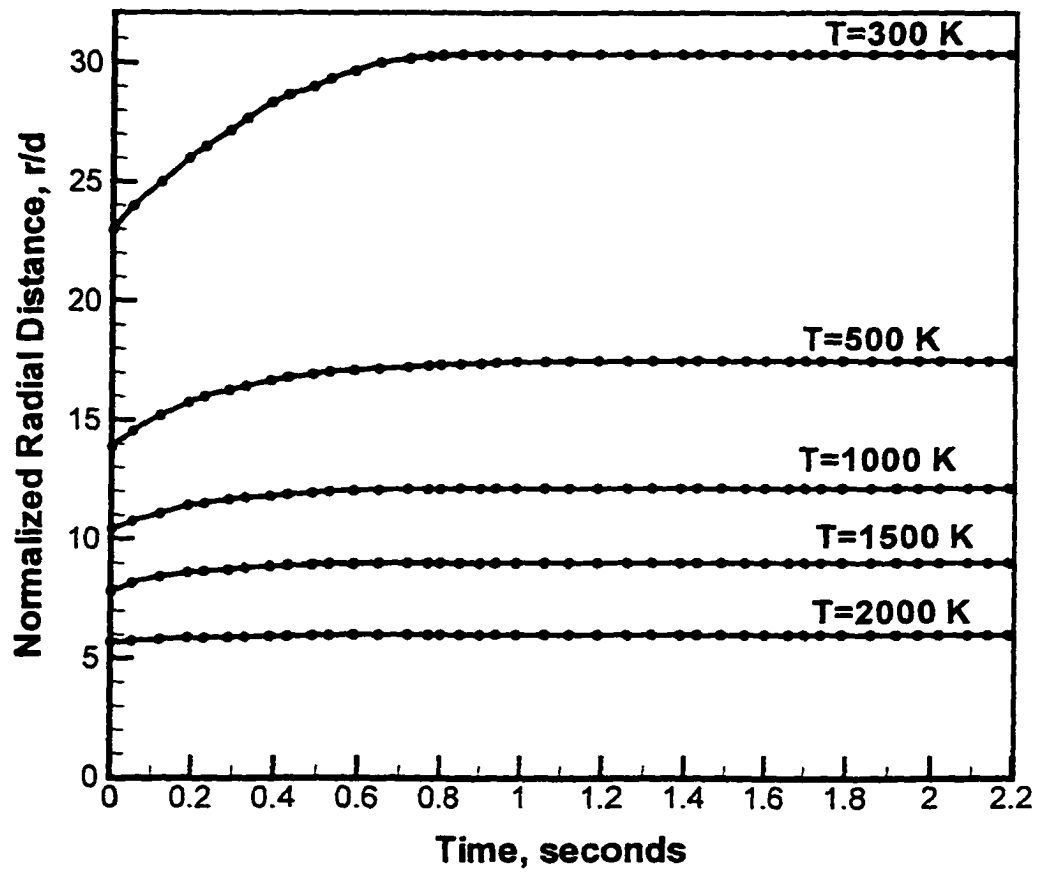


Figure 4.3.38: Temperature profiles during the drop; $z/d = 8$, $Re = 40$, and $d = 0.3$ mm

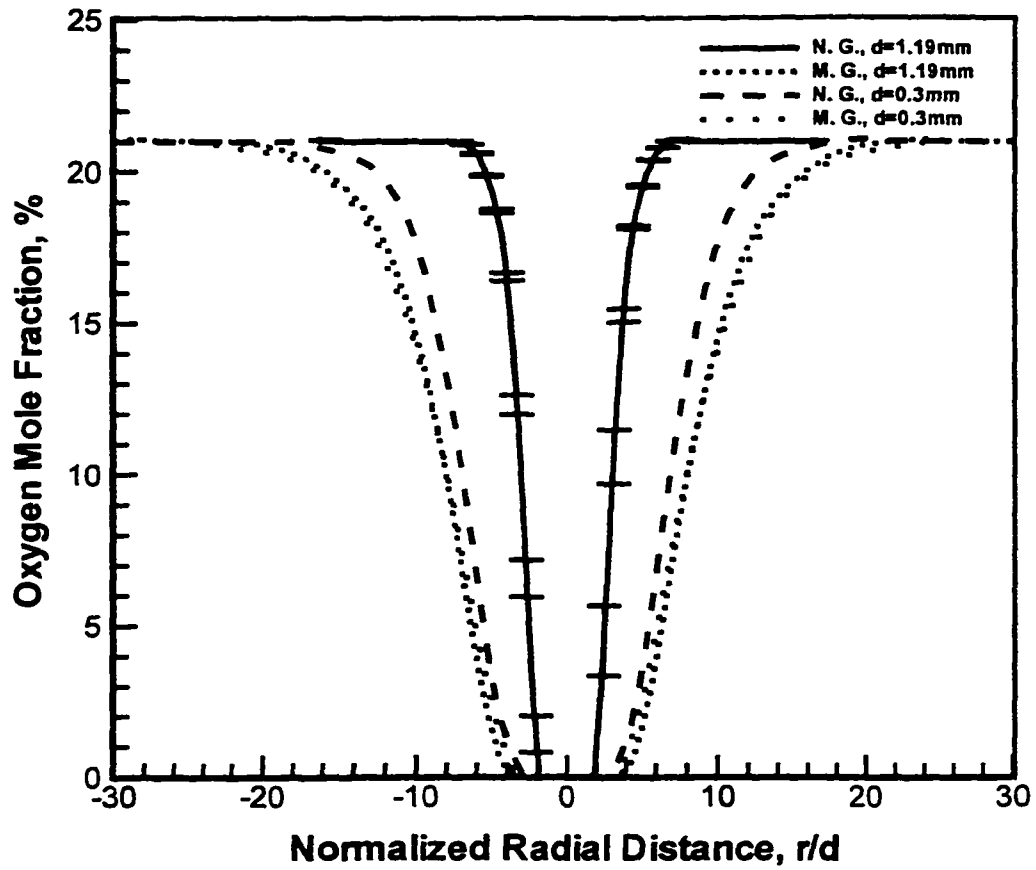


Figure 4.3.39: Burner diameter effect on oxygen mole fraction profiles in normal and microgravity; $Re = 40$ and $z/d = 4$

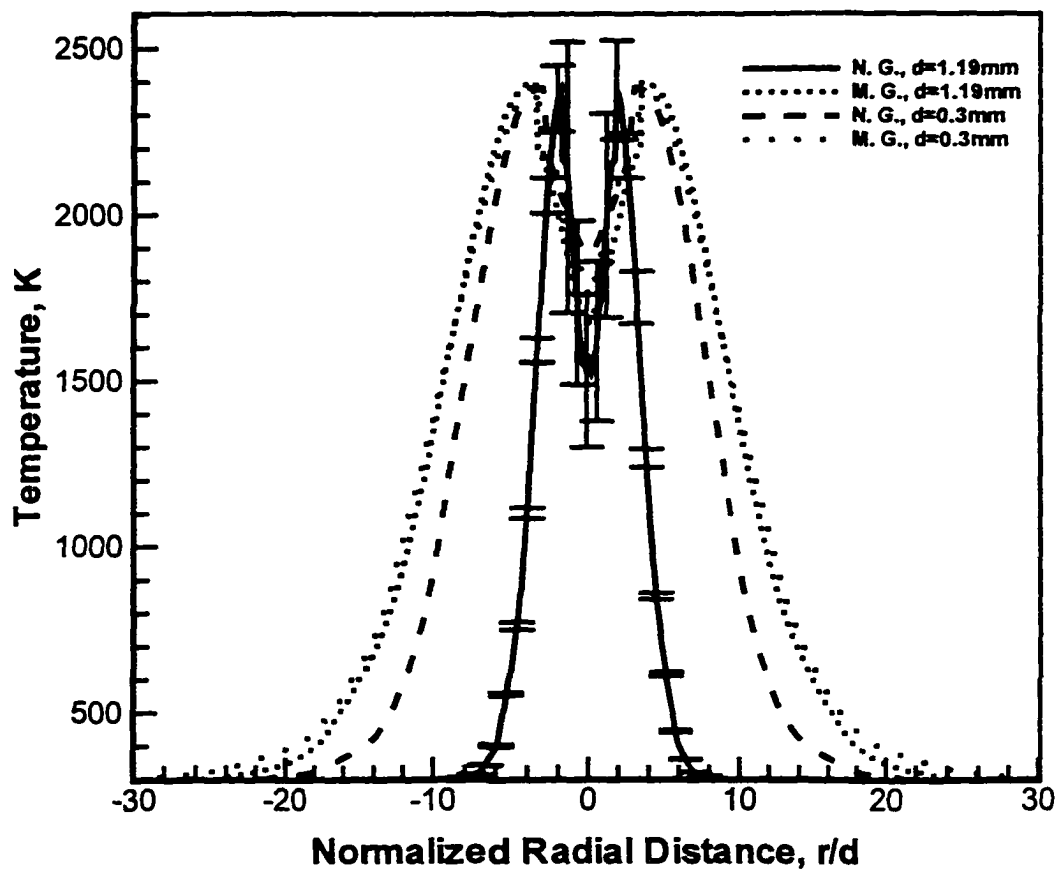


Figure 4.3.40: Burner diameter effect on temperature profiles in normal and microgravity; $Re = 40$ and $z/d = 4$

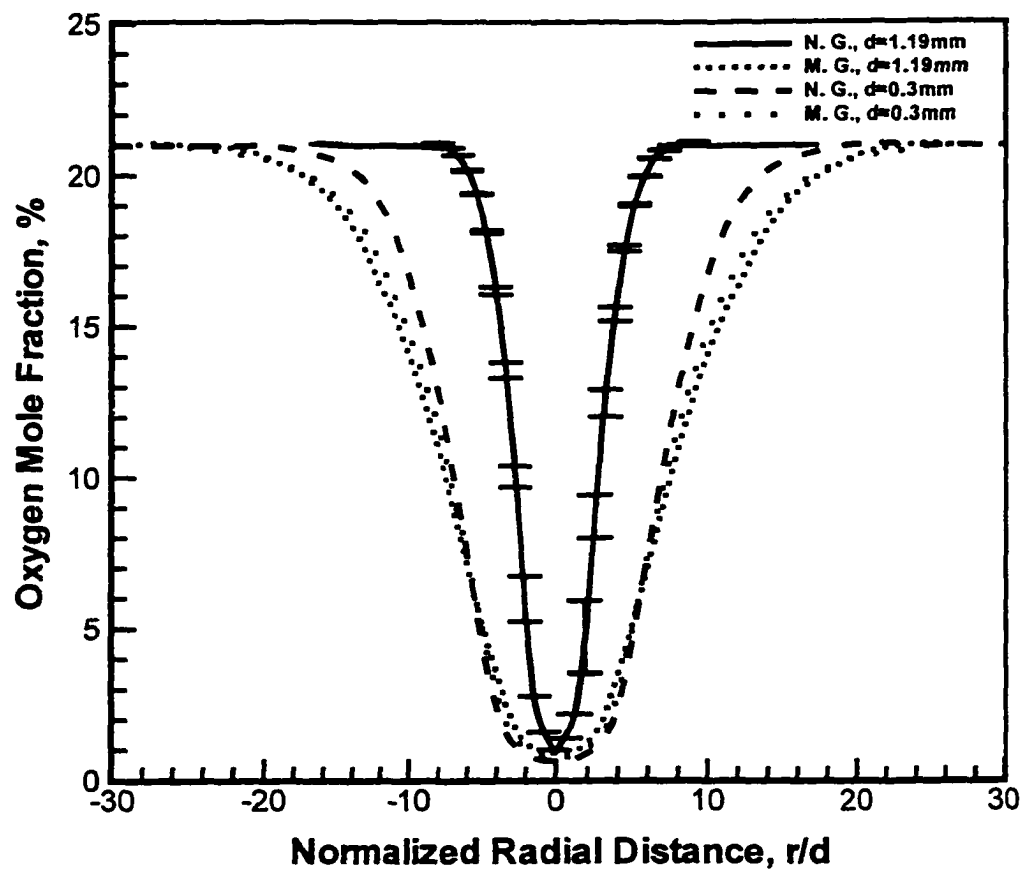


Figure 4.3.41: Burner diameter effect on oxygen mole fraction profiles in normal and microgravity; $Re = 40$ and $z/d = 8$

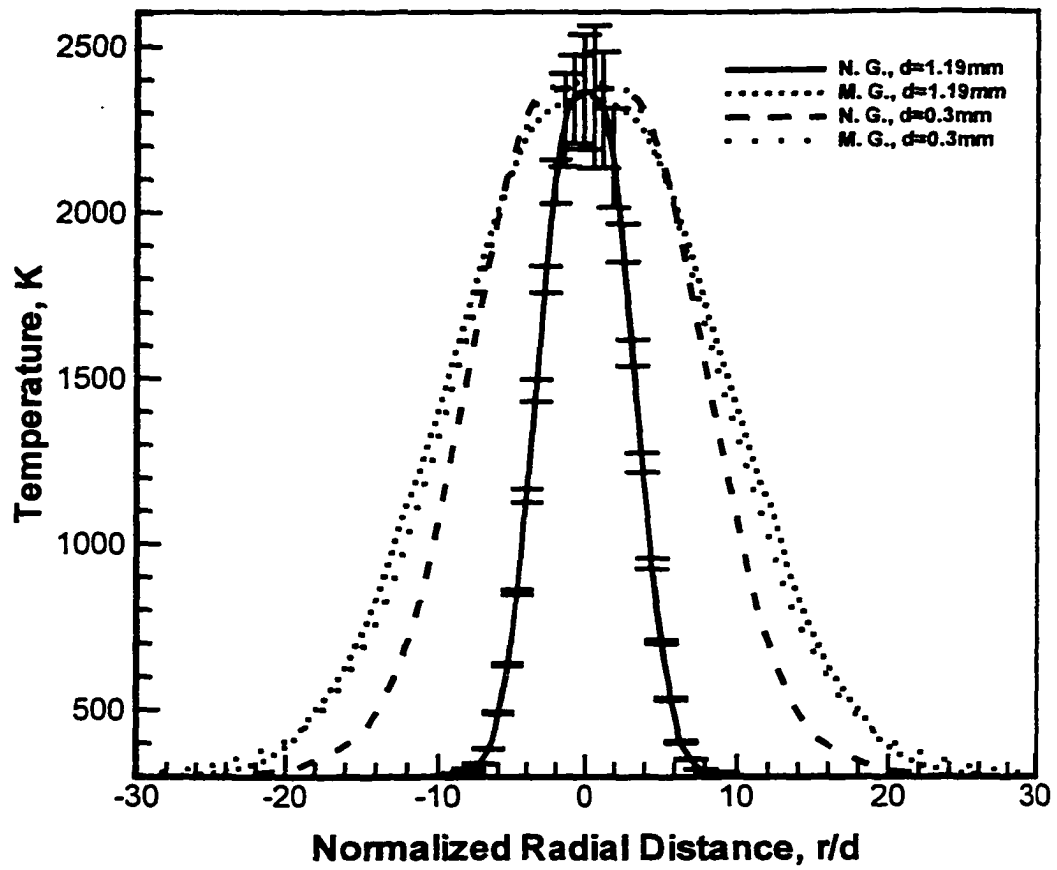


Figure 4.3.42: Burner diameter effect on temperature profiles in normal and microgravity; $Re = 40$ and $z/d = 8$

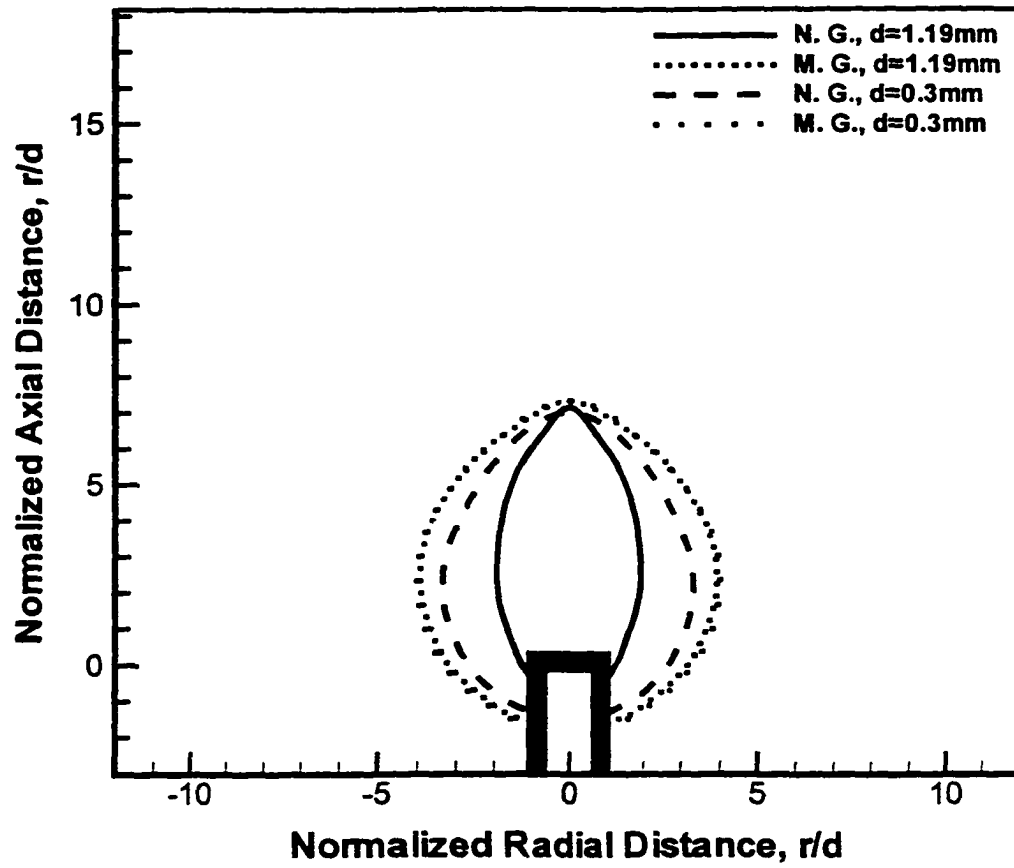


Figure 4.3.43: Burner diameter effect on flame shape in normal and microgravity; $Re = 40$

are closer to each other. Evidently, buoyancy was not significant in the case of smaller diameter burner, where the Froude number is 16 times larger.

Effect of Reynolds number on flame shape in normal and microgravity is shown in Fig. 4.3.48 for $d = 1.19$ mm. As previously observed in Figs. 4.3.43 and 4.3.30, it is shown here that the scaled flame height in normal and microgravity is the same i.e., the flame height varies linearly with the jet exit Reynolds number. Further, the flame width and hence, the flame shape did not scale linearly with the Reynolds number. Evidently, the maximum flame width in microgravity is roughly independent of the Reynolds number; an observation that was predicted by equation (2.12) in Chapter 2. The flame shape in normal and microgravity is shown in Fig. 4.3.49 for $d = 0.3$ mm, where similar trends are observed.

4.3.4 Comparison with Theory

In Chapter 2, two theories for diffusion flames in microgravity were presented. Model I, which was based on similarity, and model II, which had an exact solution. It was shown that both models, strictly speaking, were inapplicable in the context of this research because of the small Reynolds numbers used. In this subsection, model II is evaluated by comparing predictions of the oxygen mole fraction and temperature profiles and flame shape with measurement in microgravity. Again, because of the severe assumption of constant properties invoked in the theory, one cannot expect good agreement between the theory and measurement due to large variations of the fluid properties in a reacting system. However, the functional

relationship provided by the theory will be used to curve-fit the flame shape and scalar profiles; an approach similar to that in Lin et al. (1999).

The oxygen mole fraction profiles from model II theory and RSD measurements in microgravity are shown in Fig. 4.3.50 for jet-exit Reynolds number of 70 and $z/d = 4$. Note that the theoretical scalar profiles are independent of the burner diameter. The theoretical calculations are shown for theoretical Reynolds numbers (Re_τ) of 130 and 17 with Schmidt numbers of 0.2 and 0.36, respectively. Re_τ of 17 and Sc of 0.36 were obtained by curve-fitting the flame shape at $Re = 70$. Hence, a factor of 7.5 was required for Re_τ to match the experimental flame shape. This factor, in part, accounts for the changes in the density and kinematic viscosity in the flame. The discrepancy between the theoretical profile with $Re_\tau = 130$ and RSD measurement is attributed, in part, to the changes in density and kinematic viscosity because of the combustion. Measured and predicted flame shapes are shown in Fig. 4.2.51. Again, there is a discrepancy between measurement and theory using the theoretical Reynolds number of 130 and $Sc = 0.2$. However, the flame shape matches with theoretical prediction when a theoretical Reynolds number of 17 and $Sc = 0.36$ are used. Again, the lower Re_τ used accounts, on the average, for variation in the fluid properties. The measured and predicted oxygen mole fraction profiles in microgravity are shown in Fig. 4.2.52. A reasonably good agreement is reached up to $r/d \approx 9$, after which the theory begins to deviate, possibly because of the constant property assumption invoked.

The measured and predicted temperature profiles are shown in Fig. 4.2.53. Again, the discrepancy between theory and RSD measurements beyond $r/d \approx 9$ is

apparent. The oxygen mole fraction and temperature profiles are shown, respectively, in Figs. 4.3.54 and 4.3.55 for $z/d = 8$, where similar trends are observed. The theoretical flame shape with $Re_{\tau} = 17$ and $Sc = 0.36$ is compared with RSD measurements in Fig. 4.3.56. The theoretical flame shape is independent of the burner diameter, and hence no burner diameter was specified in the theory.

Next, the measurement and theoretical predictions are compared for $Re = 40$. Here, the original Re_{τ} was 75, and with the same reduction factor of 7.5, Re_{τ} becomes 10. The same Schmidt number of 0.36 was used. The measured and predicted oxygen mole fraction and temperature profiles in microgravity at $z/d = 4$ are shown, respectively, in Figs. 4.3.57 and 4.3.58. Again, the predictions agree well near the flame region, but deviate at $r/d > 9$. The oxygen mole fraction and temperature profiles at $z/d = 8$ are shown, respectively, in Figs. 4.3.59 and 4.3.60. Here, $z/d = 8$ is above the flame tip and hence, the profiles are parabolic in shape. The predicted flame shape is compared with RSD measurement in Fig. 4.3.61.

Comparison between Model II predictions and measurements has shown that although the theory based on constant property assumption is not adequate in predicting flame shape and scalar profiles in diffusion flames, it can still be used to develop functional relationship to curve-fit the measurements. Detailed computational models, however, are still required to incorporate effects of property variations in the flow field of reacting systems.

4.3 Buoyancy Effects on Transitional Diffusion Flames

In this section, the Reynolds number and fuel dilution effects on flame transition and scalar profiles in the laminar portion of transitional hydrogen gas-jet diffusion flames in normal and microgravity is presented. The transitional flame experiments were conducted for $d = 0.3$ mm. A small diameter burner was used because of the limitations imposed by the limited space on the drop rig and by safety requirements at the drop tower. The Reynolds number using pure hydrogen fuel was varied from 1300 to 1700. The effect of fuel dilution by helium was studied for a Reynolds number of 1700. In this case, the helium mole fraction in the fuel was varied from 0 to 40 %.

4.4.1 Reynolds Number Effect

The color schlieren images of hydrogen gas-jet diffusion flame in normal and microgravity at $Re = 1500$ and $d = 0.3$ mm are shown in Fig. 4.4.1. The flow symmetry in the images is fairly established. Quantitative details of the schlieren images are given next in terms of contours of the angular deflection.

The angular deflection contours at $Re = 1300$ in normal gravity are shown in Fig. 4.4.2. Note that the flow is transitional i.e., there is a laminar region near the burner exit, followed by a transitional region downstream. It is worth noting that the turbulent portion of the flow field was not quantified by the methods in this work because of the random fluctuations. In Fig. 4.4.2, large radial gradients in the outer region mark the thermal boundary layer between the flame surface and the surrounding cold air. The angular deflection contours in microgravity for $Re = 1300$

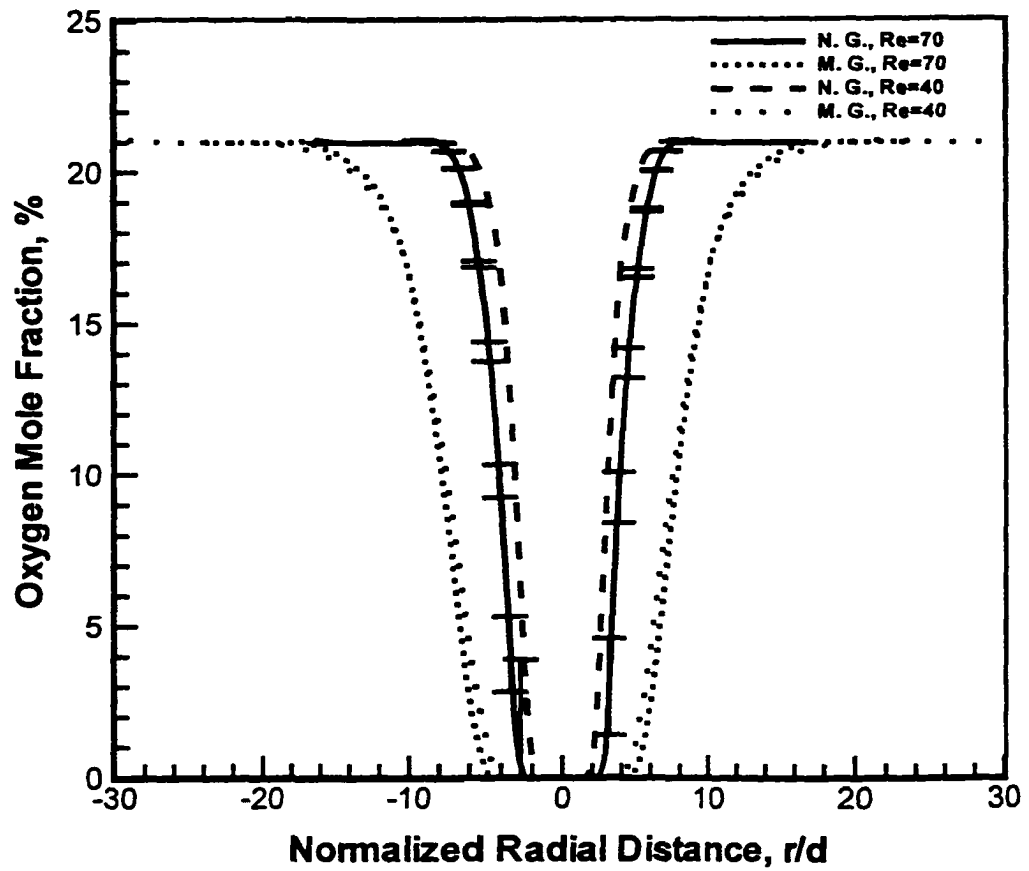


Figure 4.3.44: Reynolds number effect on oxygen mole fraction profiles in normal and microgravity for $d = 1.19$ mm; $z/d = 4$ for $Re = 70$, and $z/d = 2.3$ for $Re = 40$

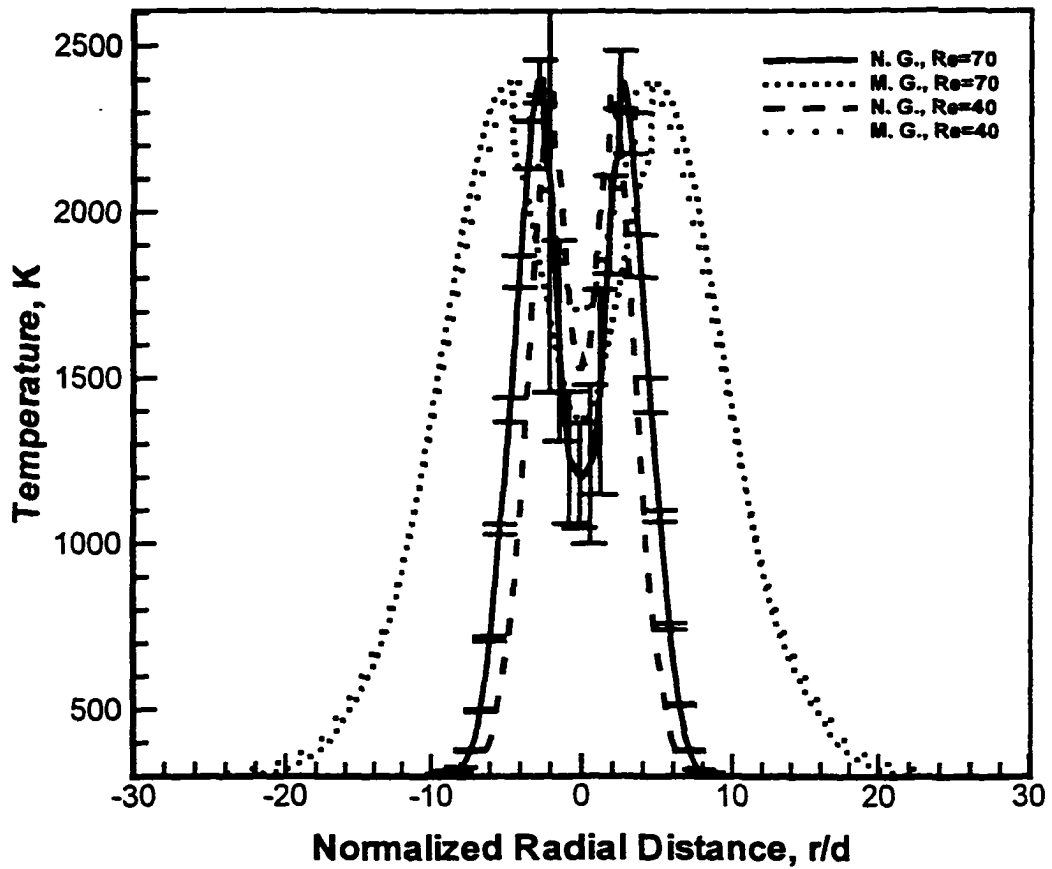


Figure 4.3.45: Reynolds number effect on temperature profiles in normal and microgravity; $d = 1.19$ mm, $z/d = 4$ for $Re = 70$, and $z/d = 2.3$ for $Re = 40$

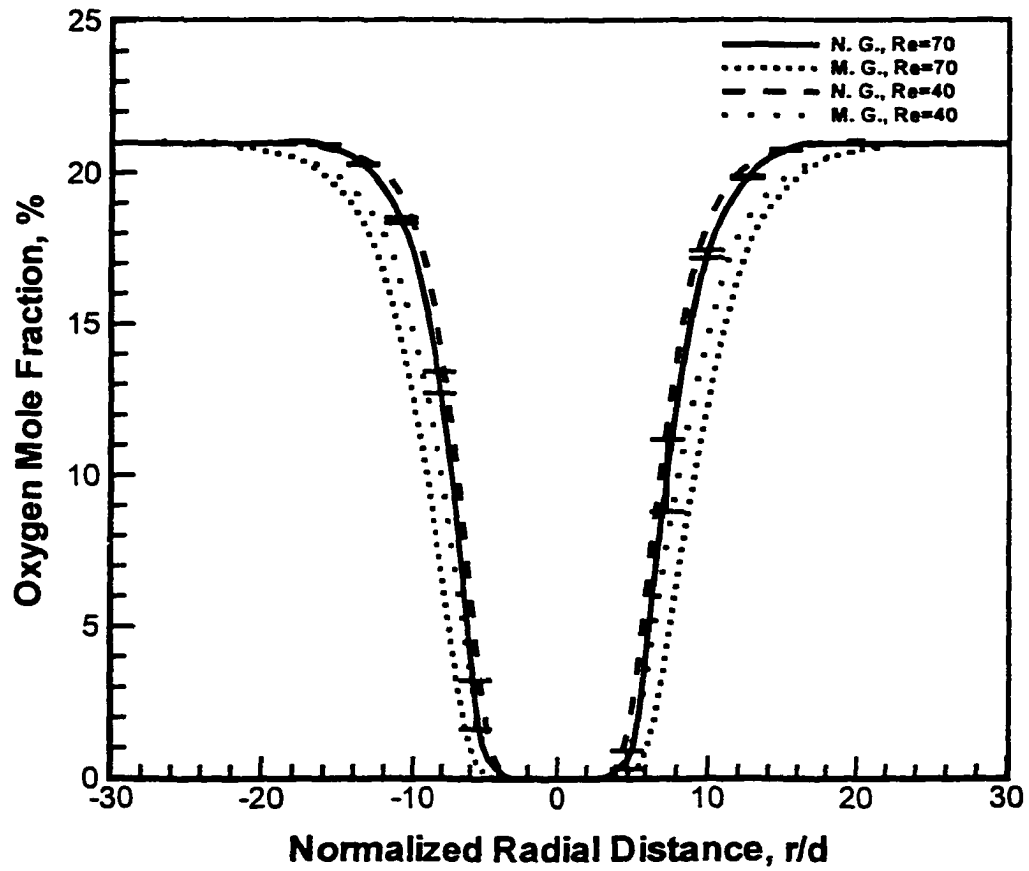


Figure 4.3.46: Reynolds number effect on oxygen mole fraction profiles in normal and microgravity; $d = 0.3$ mm, $z/d = 4$ for $Re = 70$, and $z/d = 2.3$ for $Re = 40$

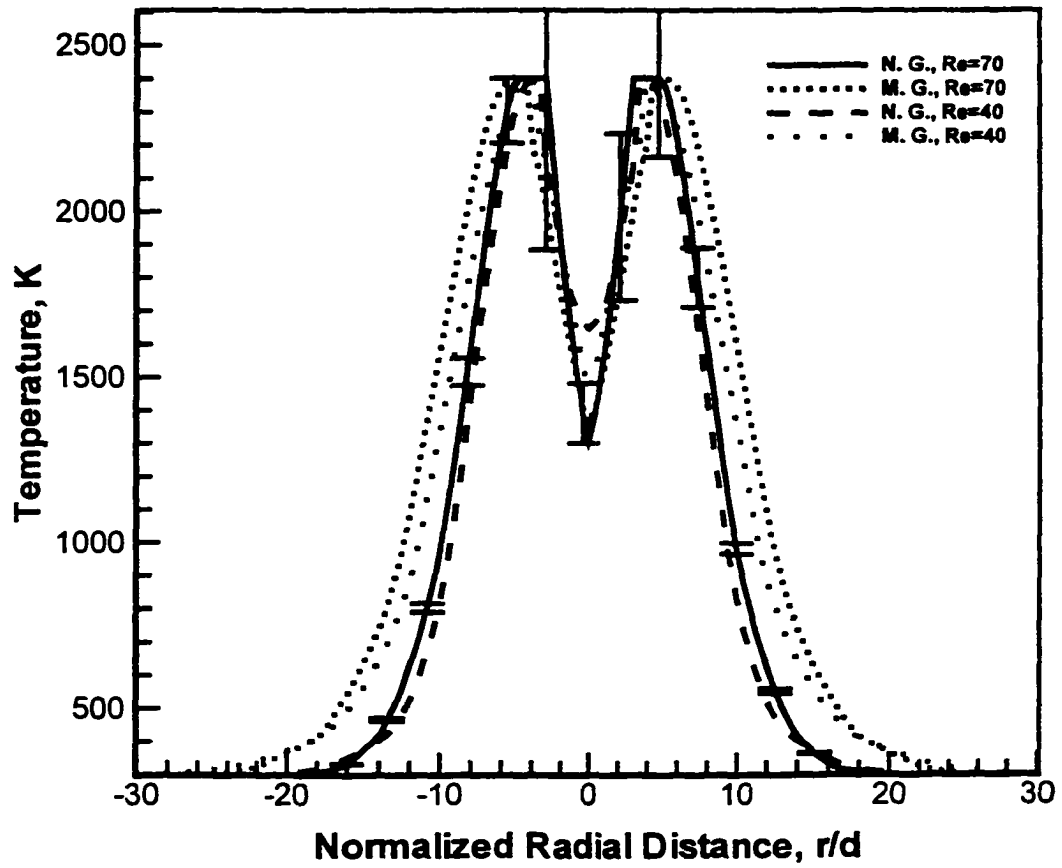


Figure 4.3.47: Reynolds number effect on temperature profiles in normal and microgravity; $d = 0.3$ mm, $z/d = 4$ for $Re = 70$, and $z/d = 2.3$ for $Re = 40$

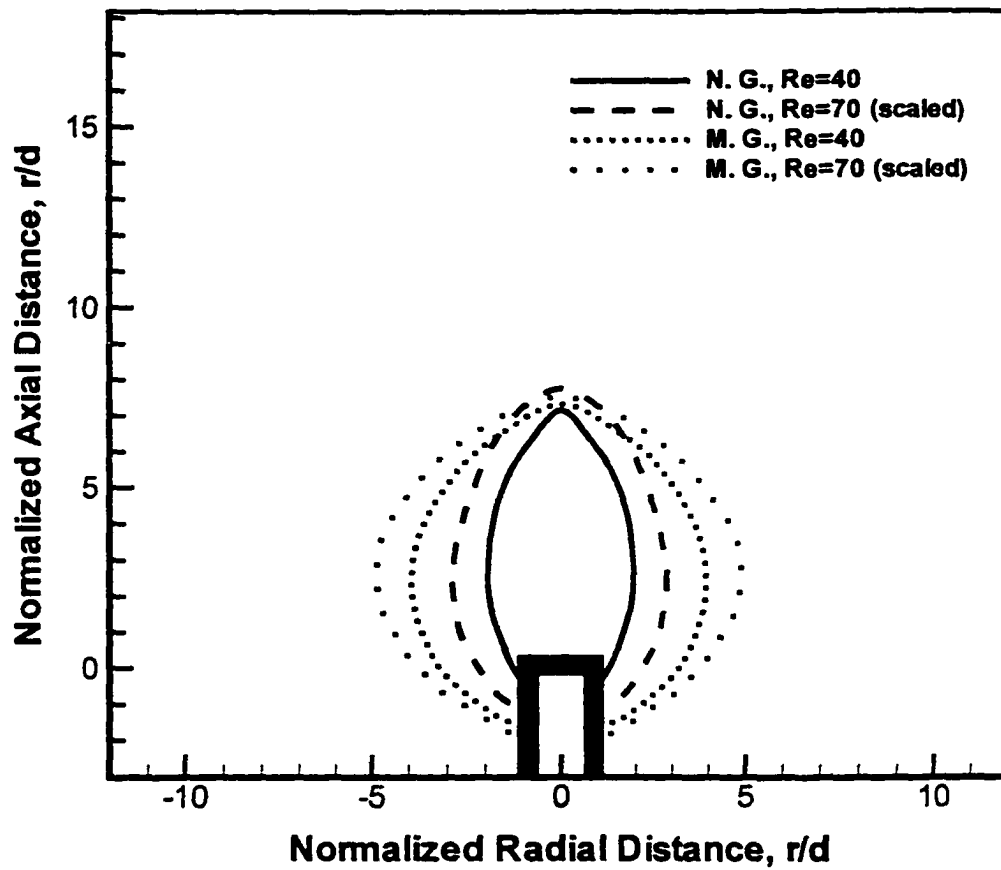


Figure 4.3.48: Reynolds number effect on flame shape in normal and microgravity; $d = 1.19$ mm

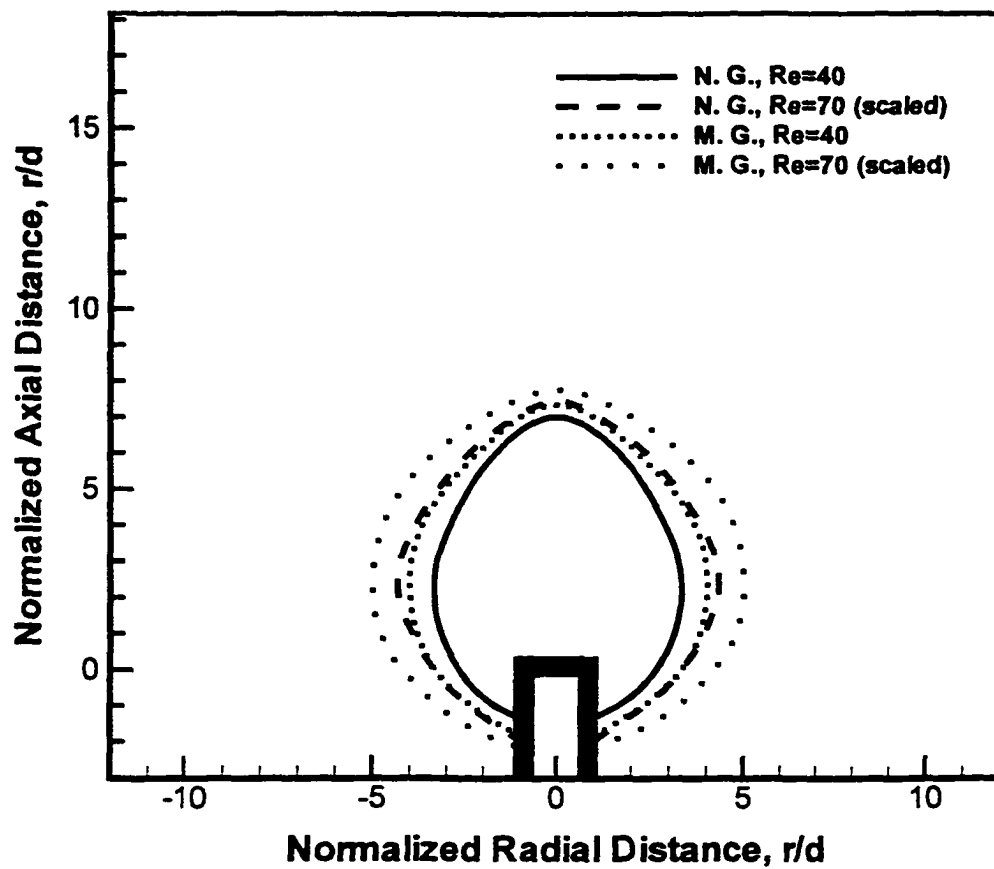


Figure 4.3.49: Reynolds number effect on flame shape in normal and microgravity; $d = 0.3$ mm

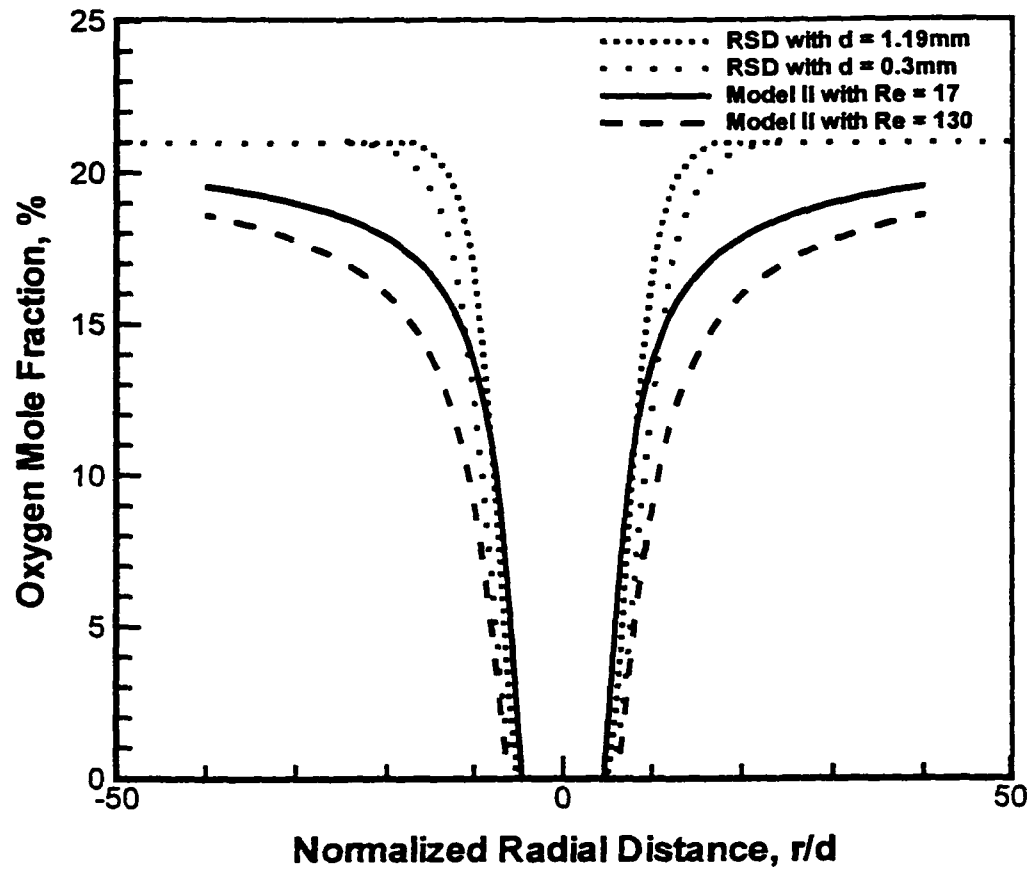


Figure 4.3.50: Oxygen concentration profiles from RSD and theory in microgravity; $Re = 70$ ($Re_T = 130$) and $z/d = 4$

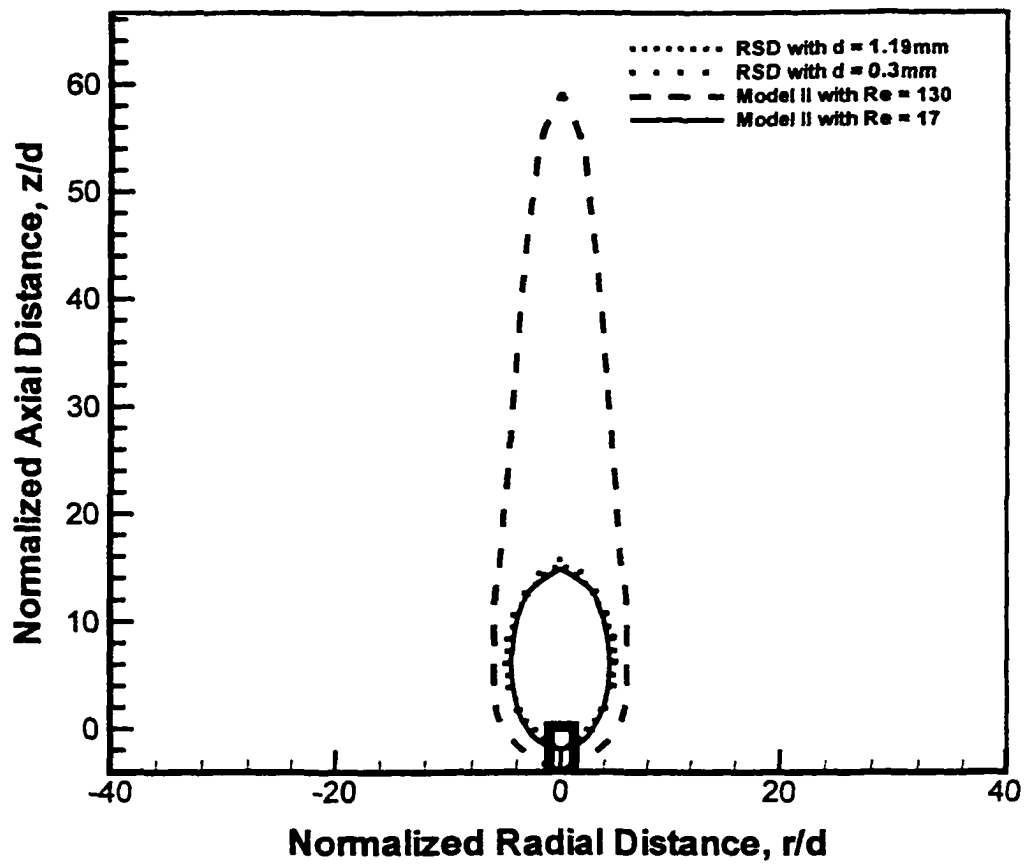


Figure 4.3.51: Flame shape from the RSD and theory in microgravity;
 $Re = 70$ ($Re_T = 130$)

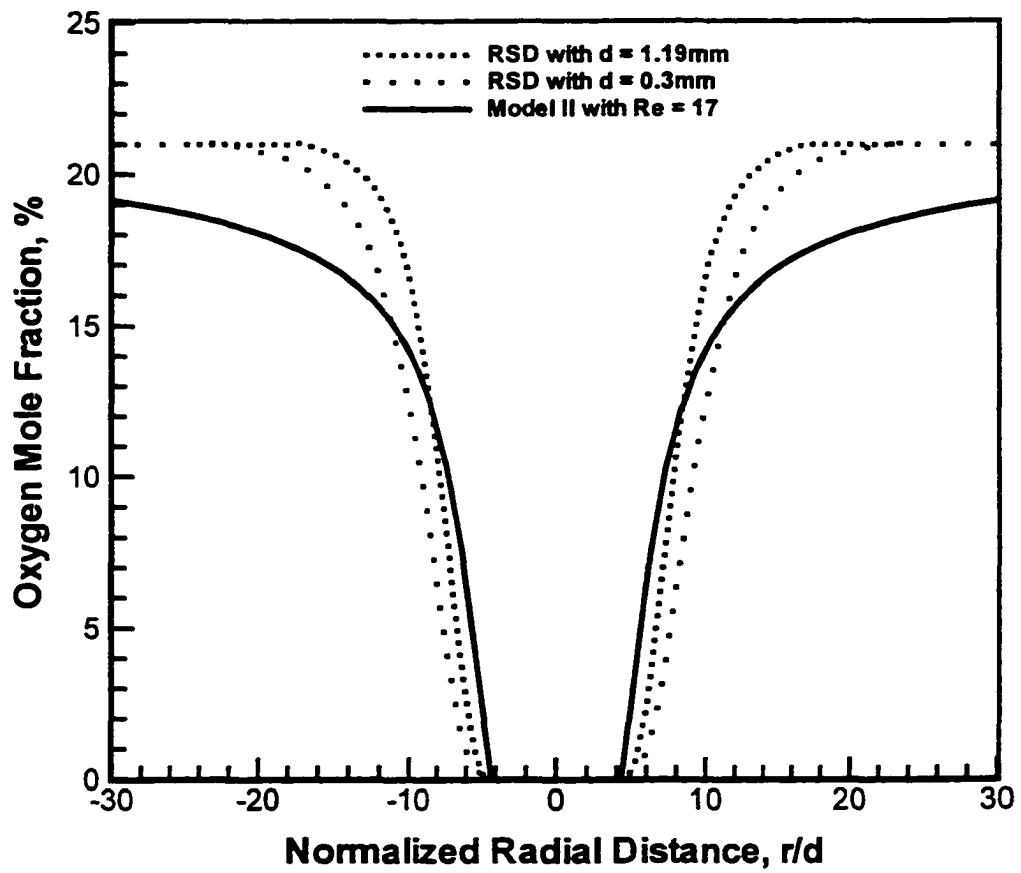


Figure 4.3.52: Oxygen mole fraction profiles from RSD and theory in microgravity; $Re = 70$ ($Re_r = 17$) and $z/d = 4$

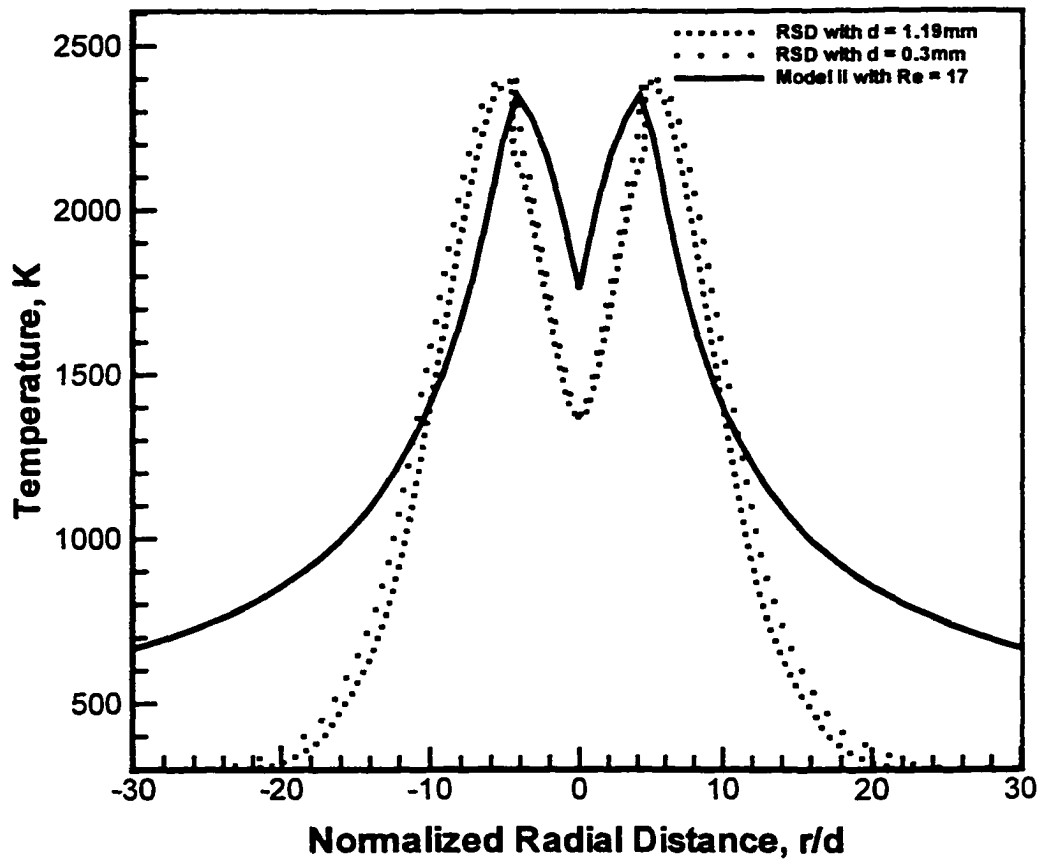


Figure 4.3.53: Temperature profiles from RSD and theory in microgravity;
 $Re = 70$ ($Re_r = 17$) and $z/d = 4$

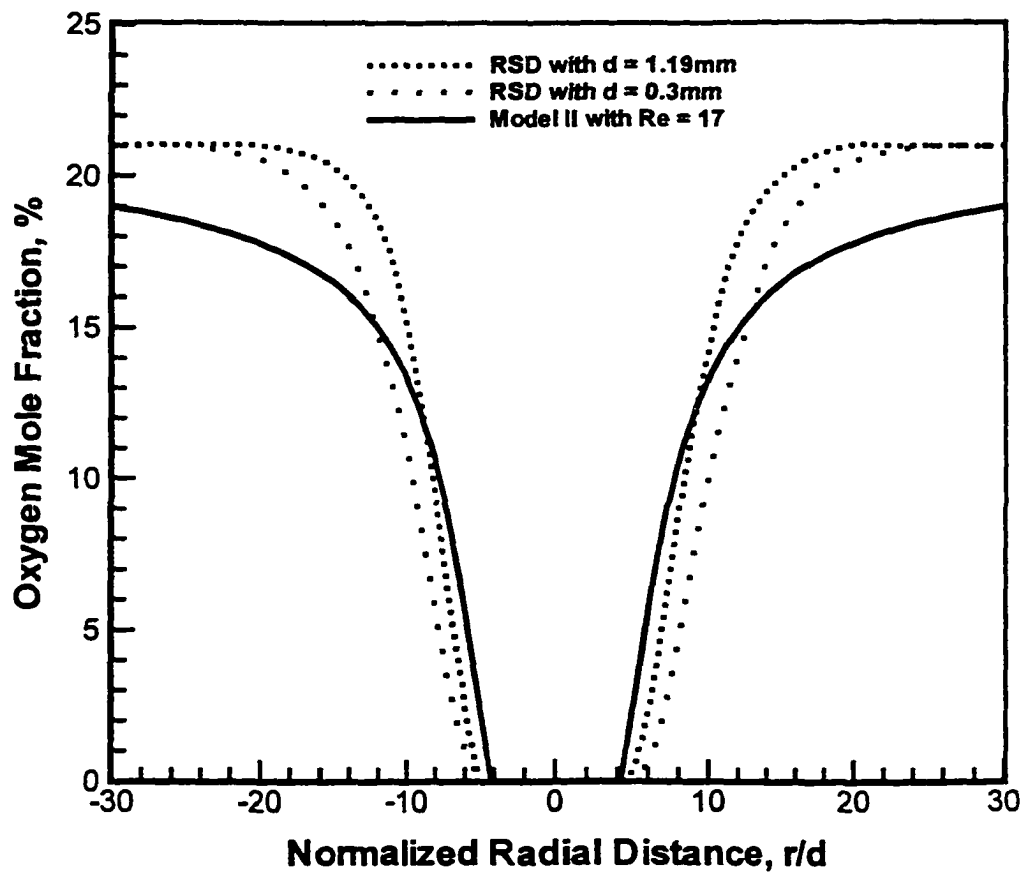


Figure 4.3.54: Oxygen mole fraction profiles from RSD and theory in microgravity; $Re = 70$ ($Re_{\tau} = 17$) and $z/d = 8$

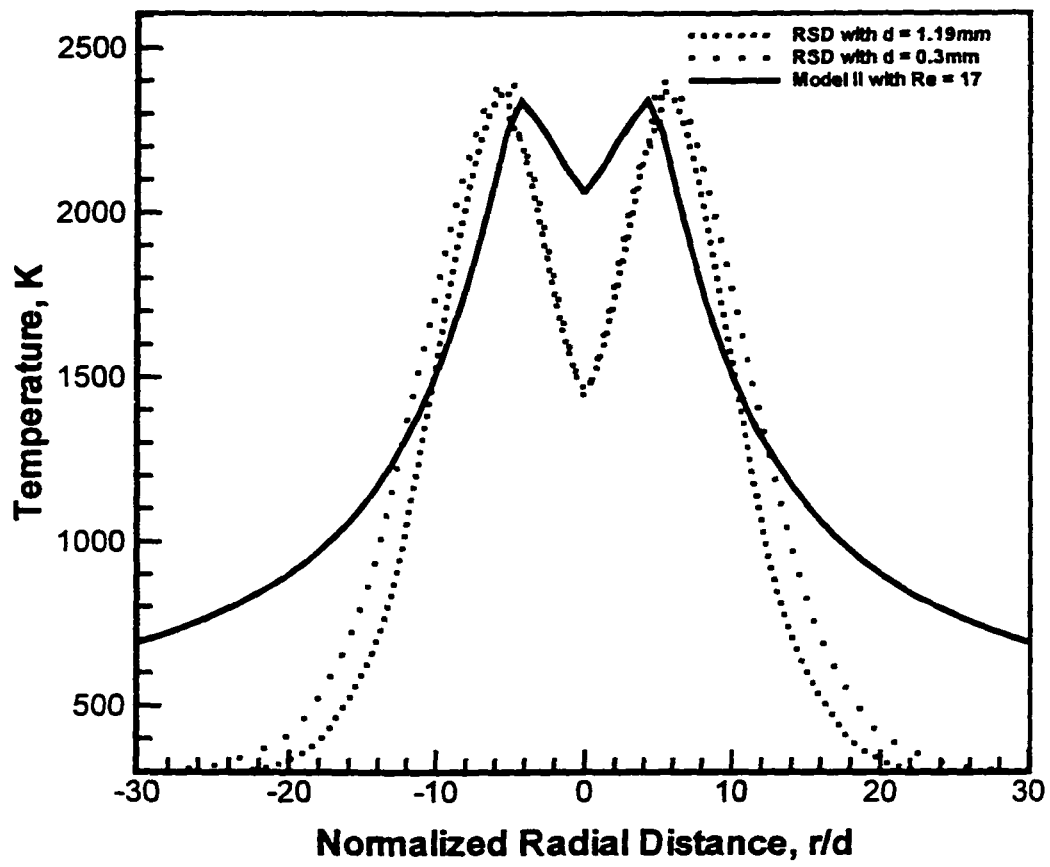


Figure 4.3.55: Temperature profiles from RSD and theory in microgravity;
 $Re = 70$ ($Re_r = 17$) and $z/d = 8$

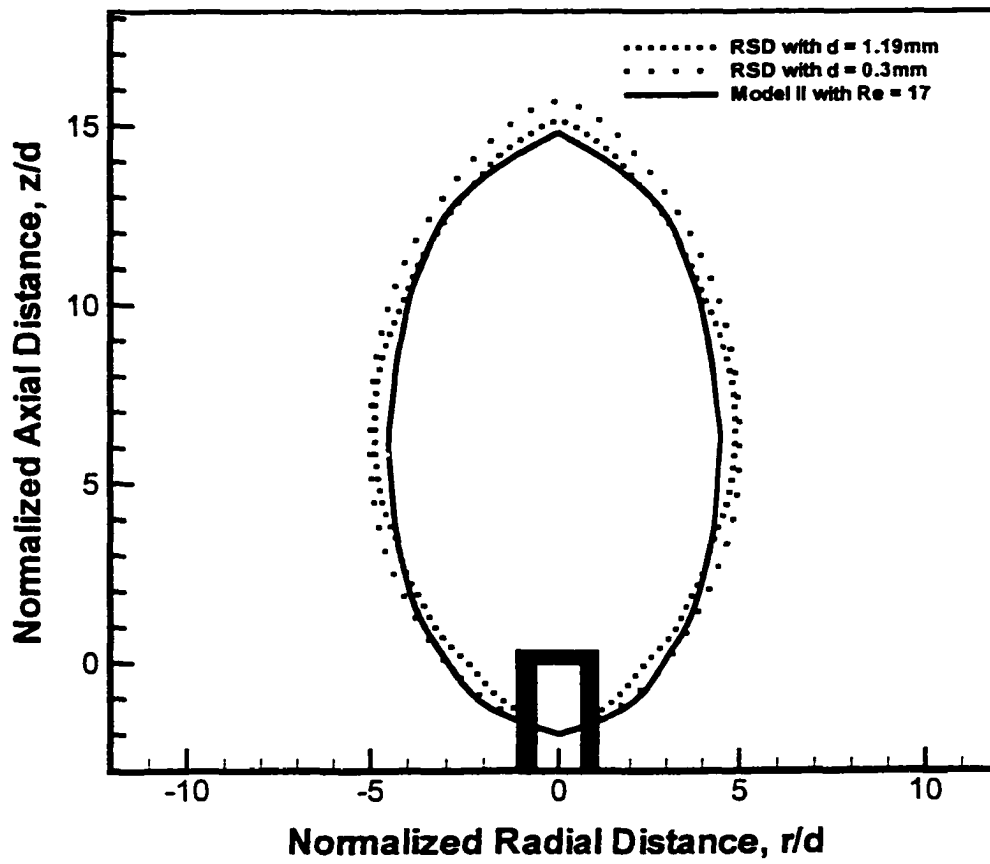


Figure 4.3.56: Flame shape from RSD and theory in microgravity;
 $Re = 70$ ($Re_T = 17$)

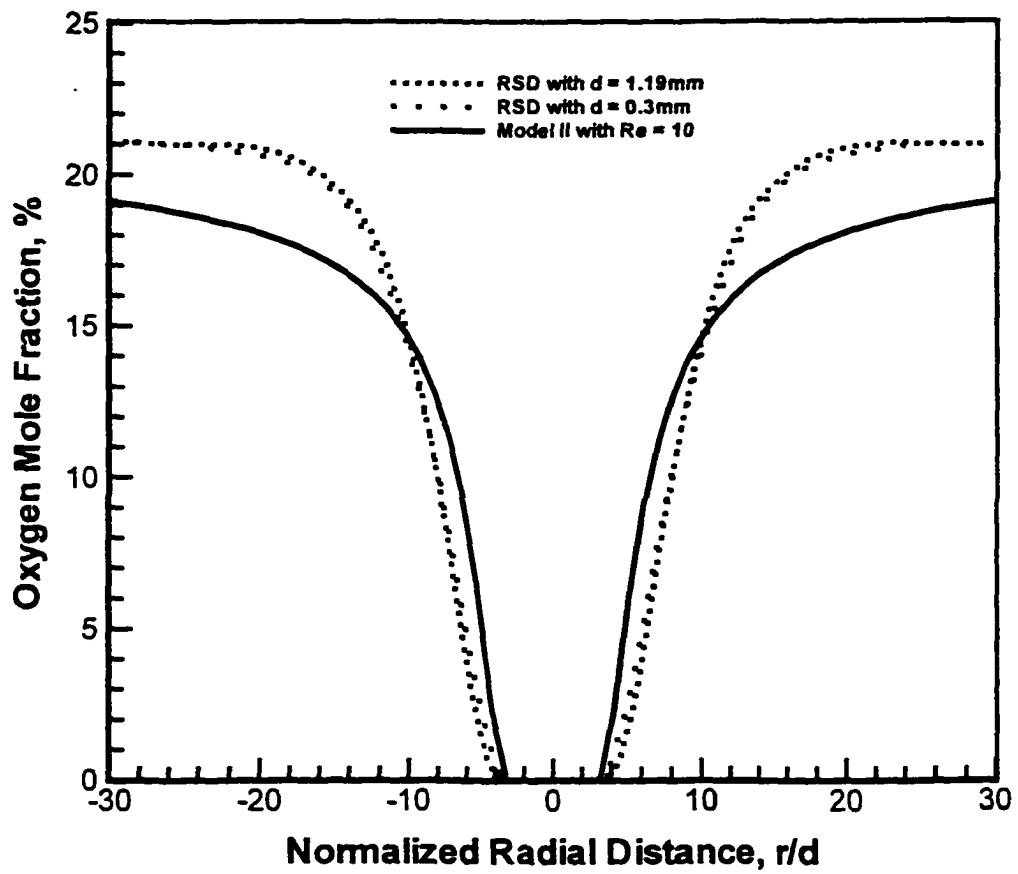


Figure 4.3.57: Oxygen mole fraction profiles from RSD and theory in microgravity; $Re = 40$ ($Re_{\tau} = 10$) and $z/d = 4$

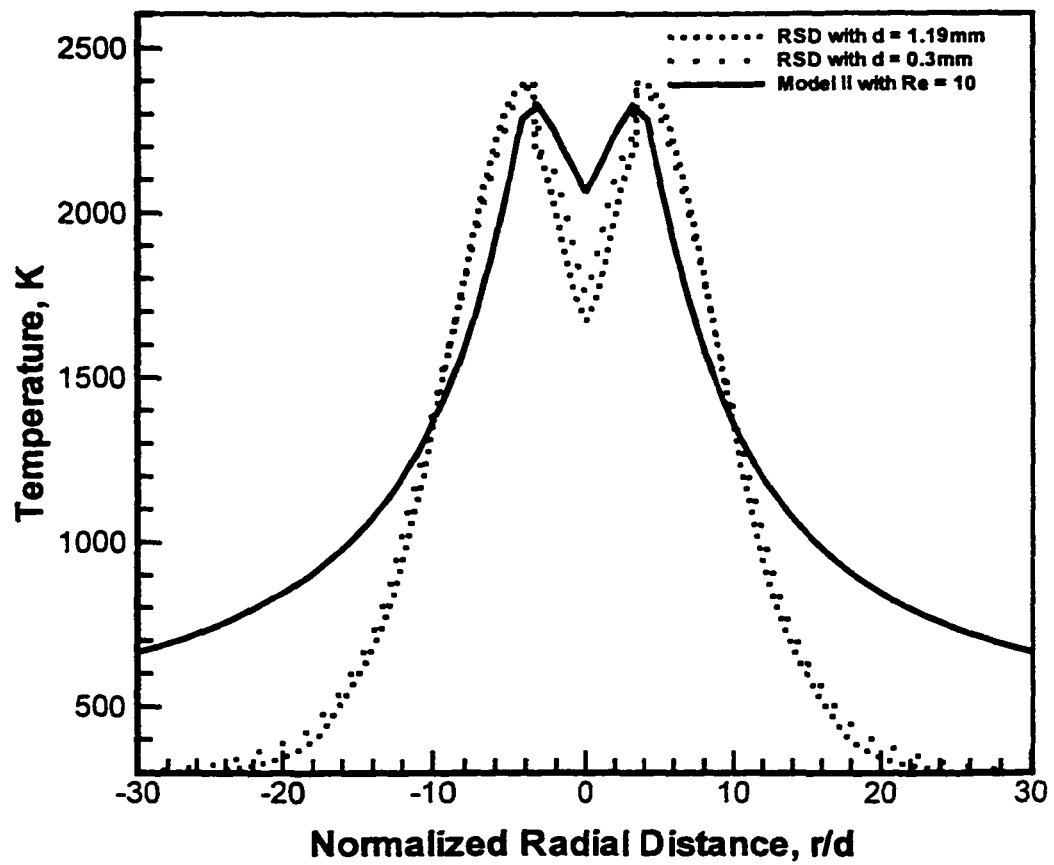


Figure 4.3.58: Temperature profiles from RSD and theory in microgravity; $Re = 40$ ($Re_{\tau} = 10$) and $z/d = 4$

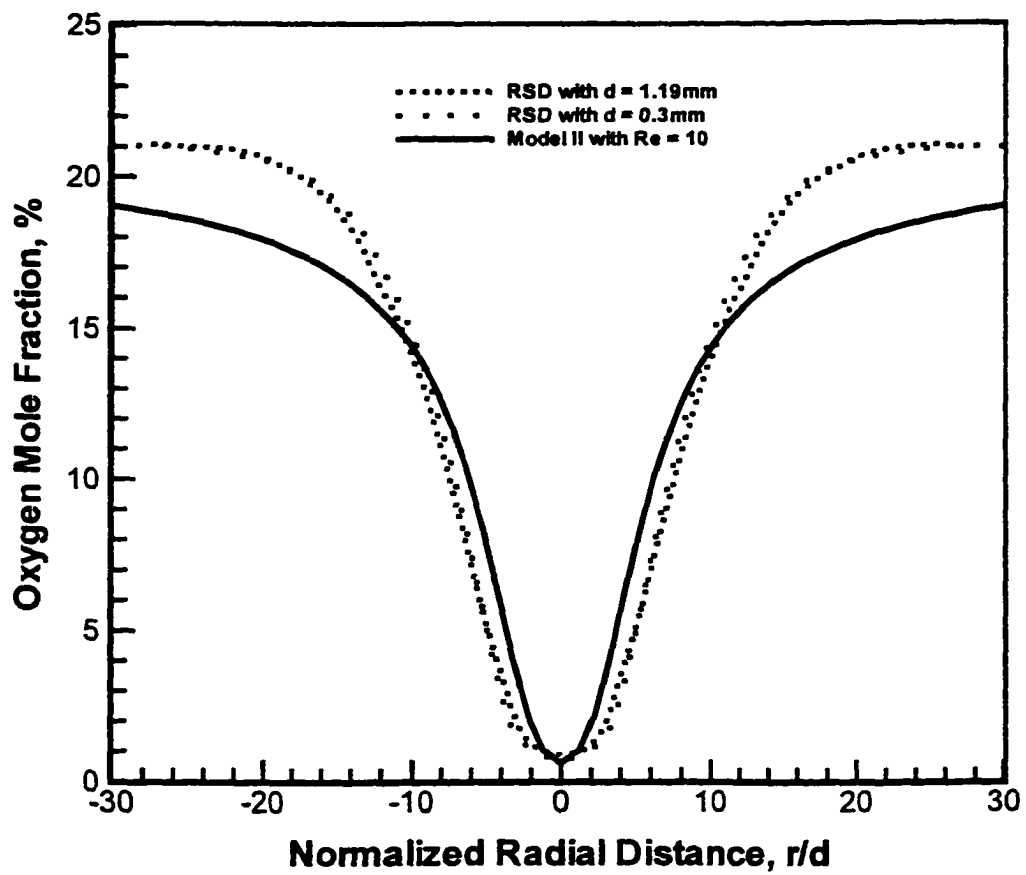


Figure 4.3.59: Oxygen mole fraction profiles from RSD and theory in microgravity; $Re = 40$ ($Re_T = 10$) and $z/d = 8$

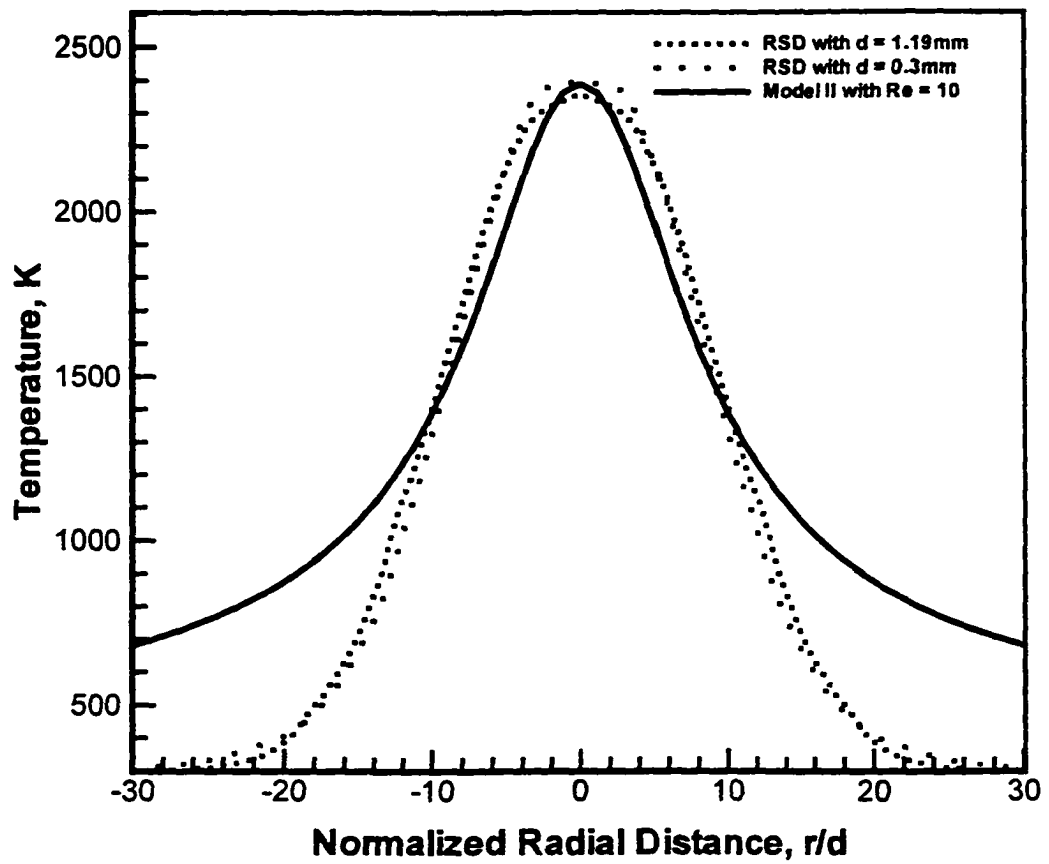


Figure 4.3.60: Temperature profiles from RSD and theory in microgravity; $Re = 40$ ($Re_r = 10$) and $z/d = 8$

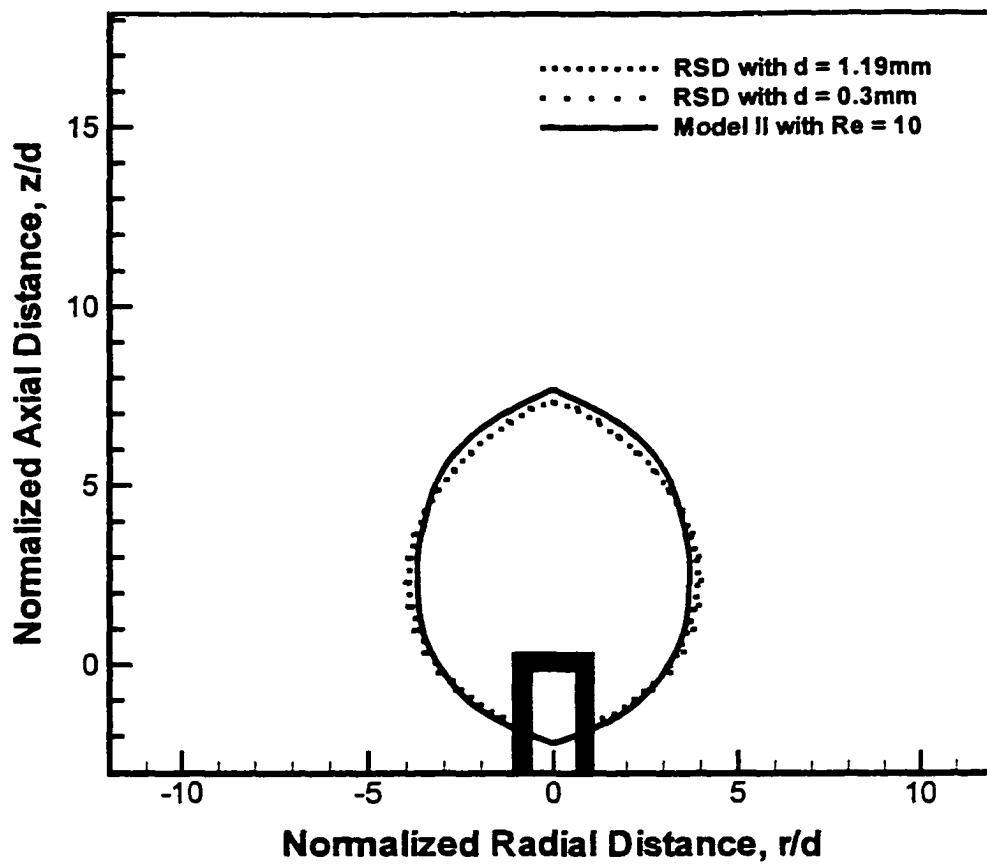


Figure 4.3.61: Flame shape from RSD and theory in microgravity;
 $Re = 40$ ($Re_T = 10$)

are shown in Fig. 4.4.3. Here, it is apparent that the transitional region has shifted downstream. This is caused, in part, by a reduction in effective Reynolds number because of the loss of buoyant acceleration. It is, therefore, possible that at some Reynolds number below 1300, a transitional flame in normal gravity will become laminar in microgravity. The angular deflection contours in normal gravity for Reynolds number of 1500 are shown in Fig. 4.4.4. Here, the transitional region has shifted upstream compared to that for $Re = 1300$. In microgravity (Fig. 4.4.5), the transition occurs further downstream compared to that in normal gravity. A similar effect of gravity is observed Figs. 4.4.6 and 4.4.7 for $Re = 1700$. However, the effect of gravity is less significant. This is because at higher Reynolds number, the jet inertia dominates the buoyancy acceleration i.e., the Froude number is high.

The transitional height, defined as the axial distance between the jet exit and transitional plane, is shown in Fig. 4.4.8 as a function of Reynolds number in normal and microgravity. Here, it is shown that the transitional height decreases as the Reynolds number increases. Judging from the slope at $Re = 1300$, it appears that the microgravity flame may laminarize at $Re < 1300$. Figure 4.4.8 also reveals that the difference between normal and microgravity transitional heights decreases with increasing Reynolds numbers.

The Reynolds number effect on oxygen mole fraction profiles in the laminar portion of the transitional flames is shown in Fig. 4.4.9. Unlike the laminar flames discussed in section 4.2.3, it is shown that the profiles in normal and microgravity are not independent of the Reynolds number when the axial location is normalized in the manner shown i.e., by scaling the axial distance with Reynolds number. The

corresponding temperature profiles are shown in Fig. 4.4.10. The same scaling trends are also observed here.

4.3.2 Helium Dilution Effect.

The angular deflection contours in normal gravity for $Re = 1700$ and helium mole fraction in fuel, $X_{He} = 0.2$ are shown in Fig. 4.4.11. Here, the radial flow domain is smaller than that for $X_{He} = 0.0$ (see Fig. 4.4.6). This is because of the smaller stoichiometric air fuel ratio required for the diluted fuel. Transition region has also shifted downstream by adding the diluent in the fuel. This shift is perhaps caused by a reduced effective Reynolds number resulting from dilution. The deflection angle contours in microgravity are shown in Fig. 4.4.12. Again, the transition region is downstream of that in normal gravity.

Effect of increasing the helium mole fraction on flame transition in normal and microgravity is depicted, respectively, in Figs. 4.4.13 and 4.4.14. Results show trends similar to those observed previously for $X_{He} = 0.2$ i.e., narrowing of the angular deflection contours and shift of the transitional region. The transitional height as a function of helium mole fraction is shown in Fig. 4.4.15 for $Re = 1700$. Here, it is shown that the transitional height increases with increasing helium mole fraction, and that the difference between normal and microgravity transitional heights increases with increasing helium mole fraction.

The helium mole fraction profiles in normal and microgravity for $Re = 1700$ and $z/d = 20$ are shown in Fig. 4.4.16. These profiles reflect the amount of initial dilution introduced in the fuel. The effect of helium dilution on oxygen mole fraction

profiles is shown in Fig. 4.4.17 for $\phi = 1700$. Here, the helium dilution is shown to narrow the profiles both in normal and microgravity. This is because the stoichiometric reaction with diluted fuel requires less oxygen. Similar trends are observed in Fig. 4.4.18, where the temperature profiles are shown.



4.4.1: Schlieren images of hydrogen gas-jet diffusion flame in normal (a) and microgravity (b); $Re = 1500$ and $d = 0.3$ mm

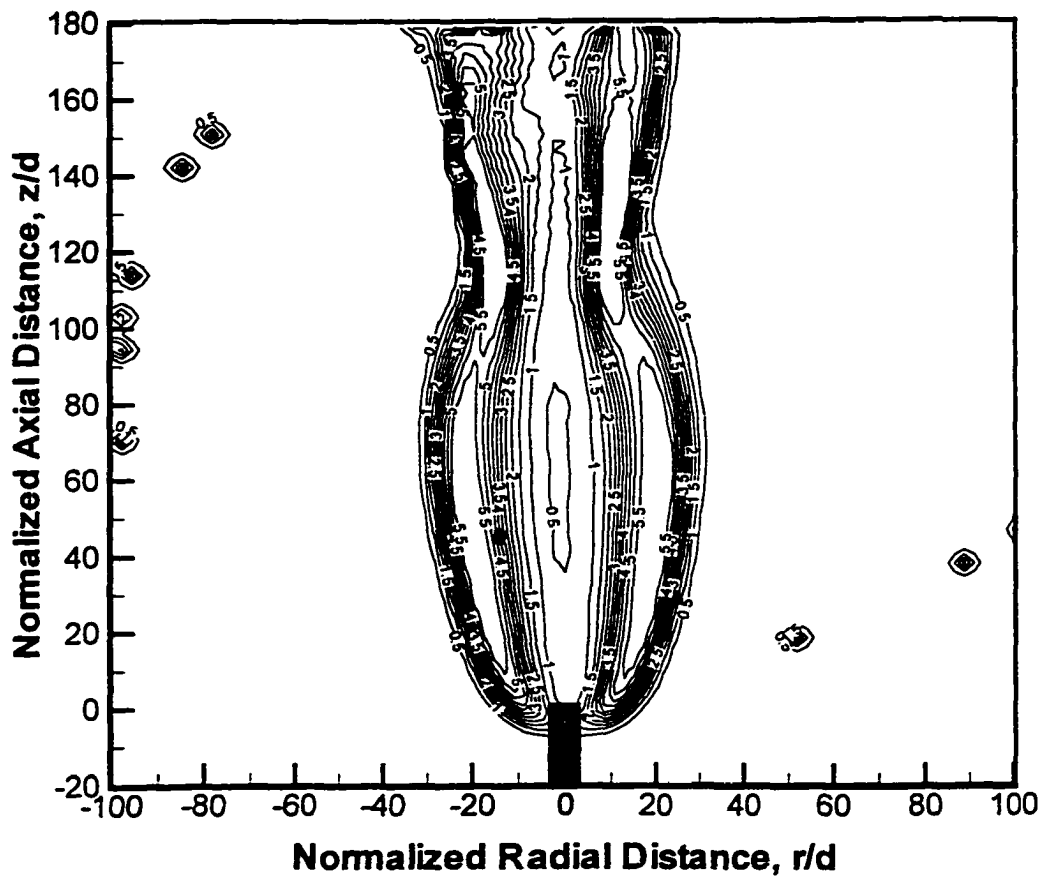


Figure 4.4.2: Contours of angular deflection in units of 10^{-4} radians in normal gravity; $Re = 1300$ and $d = 0.3$ mm

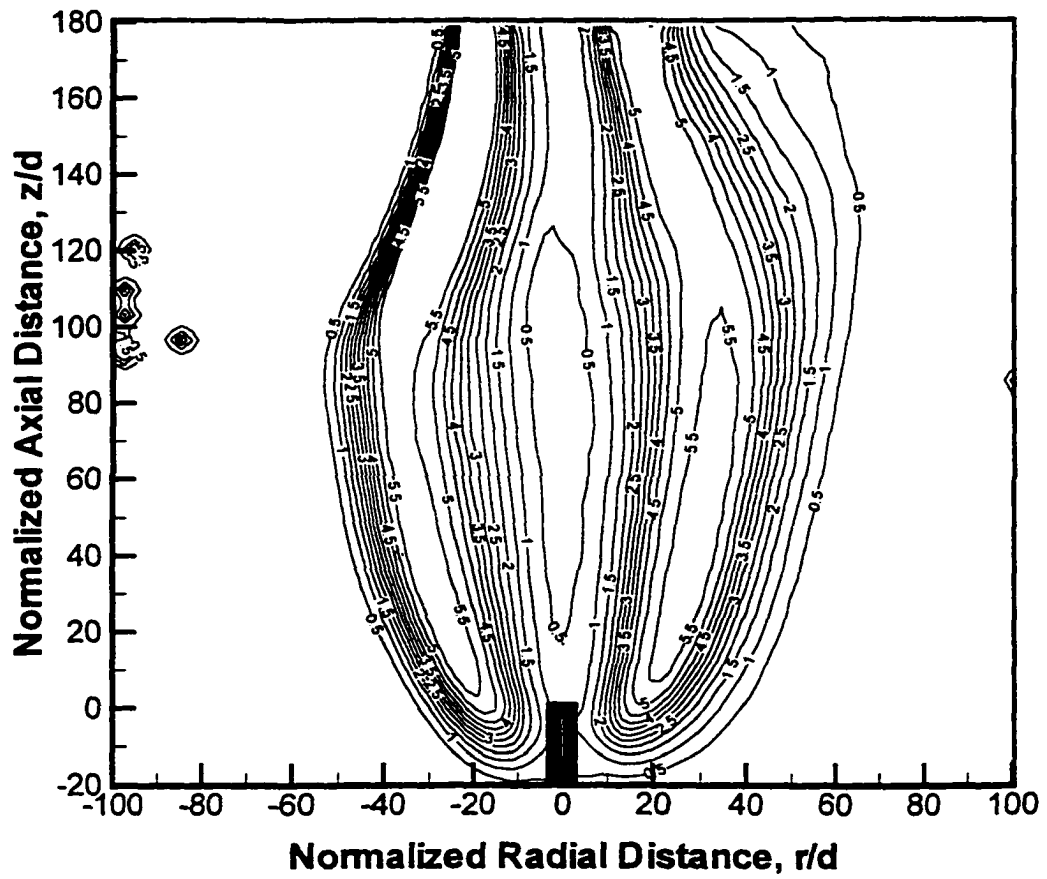


Figure 4.4.3: Contours of angular deflection in units of 10^{-4} radians in microgravity; $Re = 1300$ and $d = 0.3$ mm

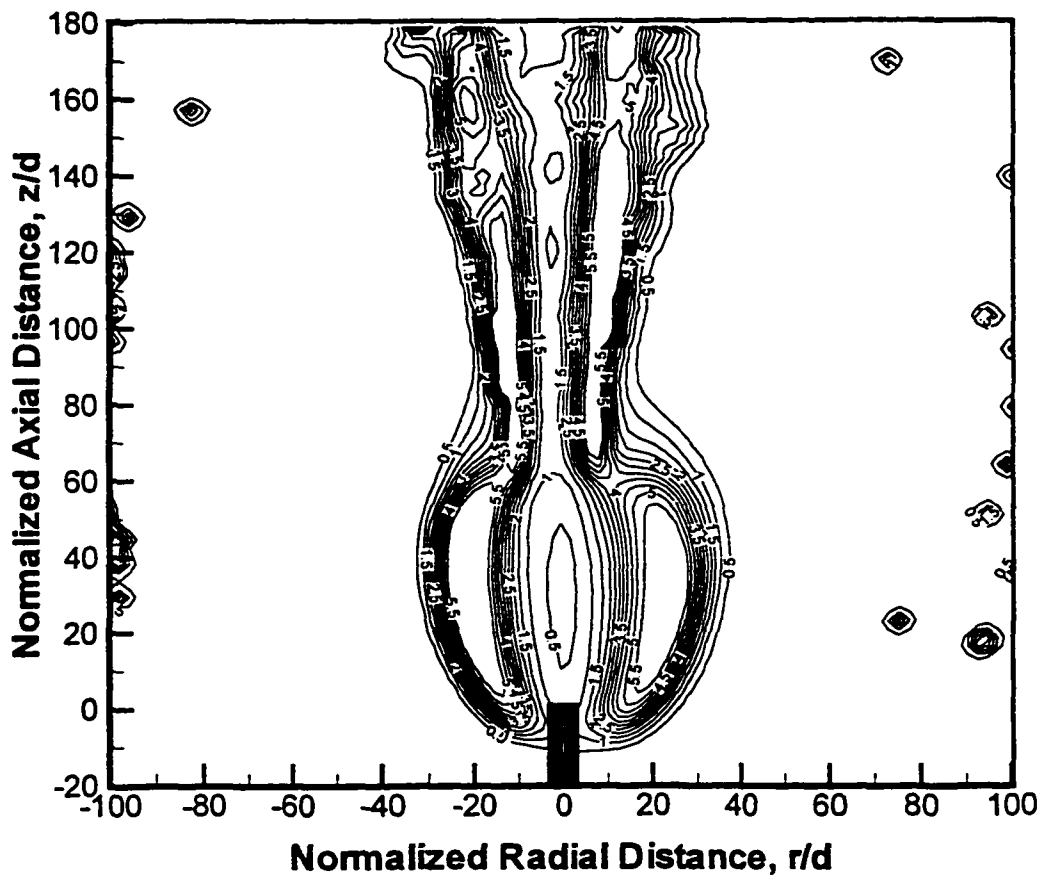


Figure 4.4.5: Contours of angular deflection in units of 10^{-4} radians in microgravity; $Re = 1500$ and $d = 0.3$ mm

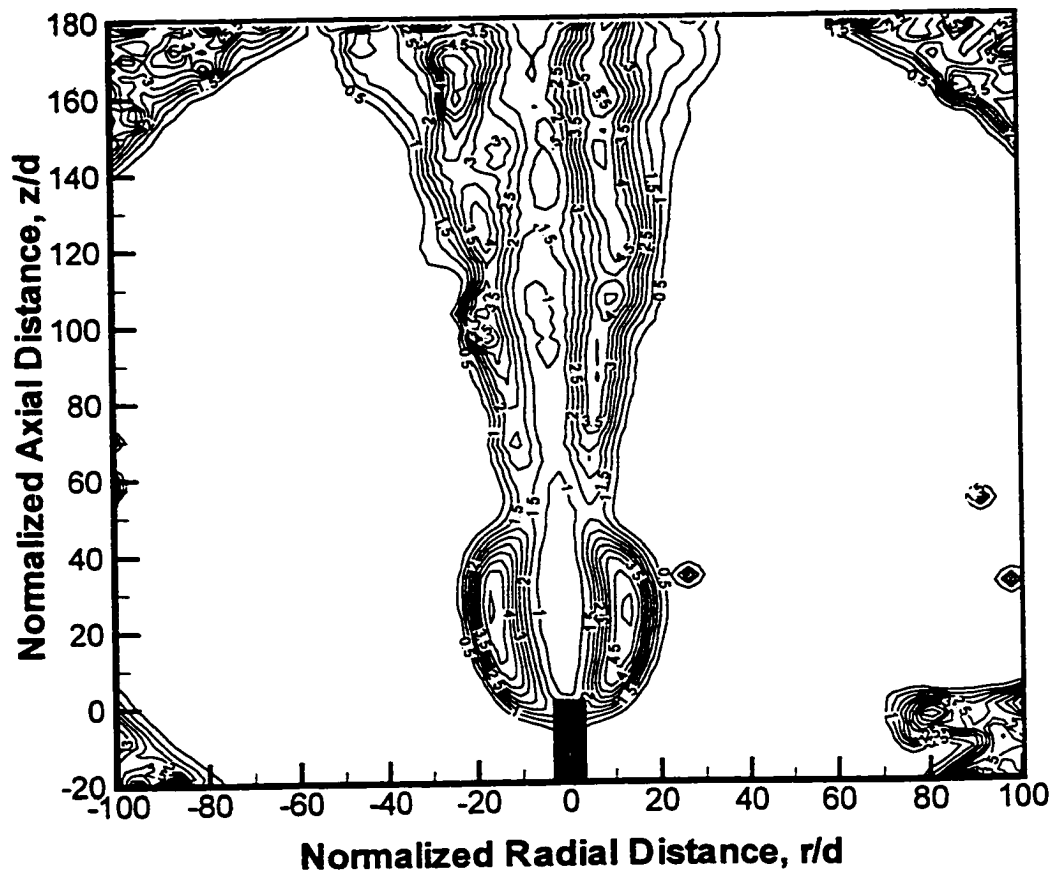


Figure 4.4.6: Contours of angular deflection in units of 10^{-4} radians in normal gravity; $Re = 1700$ and $d = 0.3$ mm

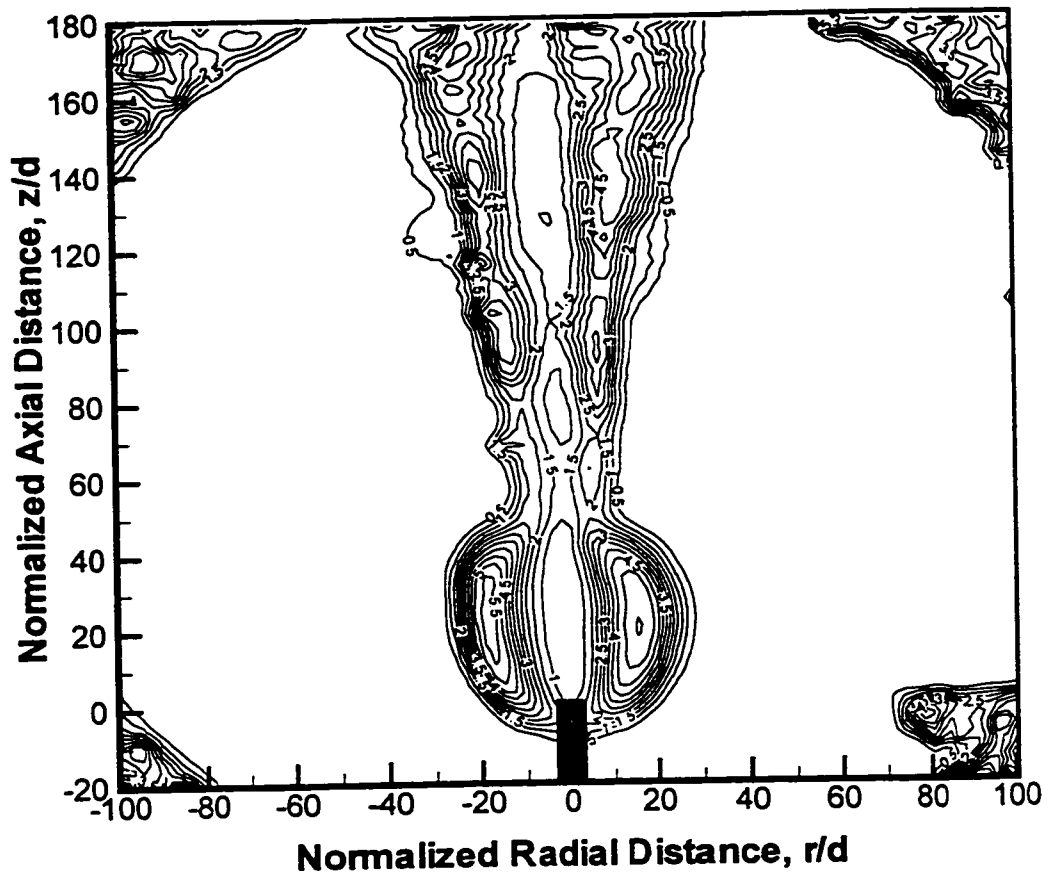


Figure 4.4.7: Contours of angular deflection in units of 10^{-4} radians in microgravity; $Re = 1700$ and $d = 0.3$ mm

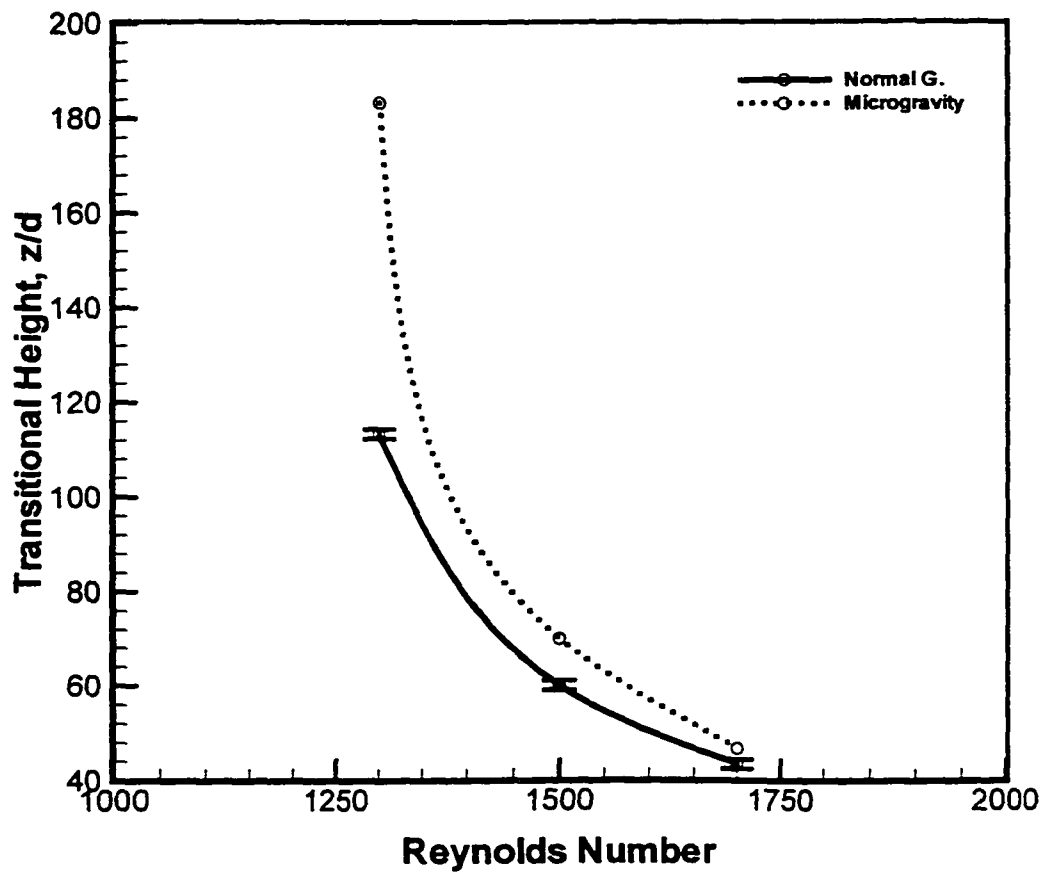


Figure 4.4.8: Transitional height as a function of Reynolds number for the pure hydrogen case; $d = 0.3$ mm

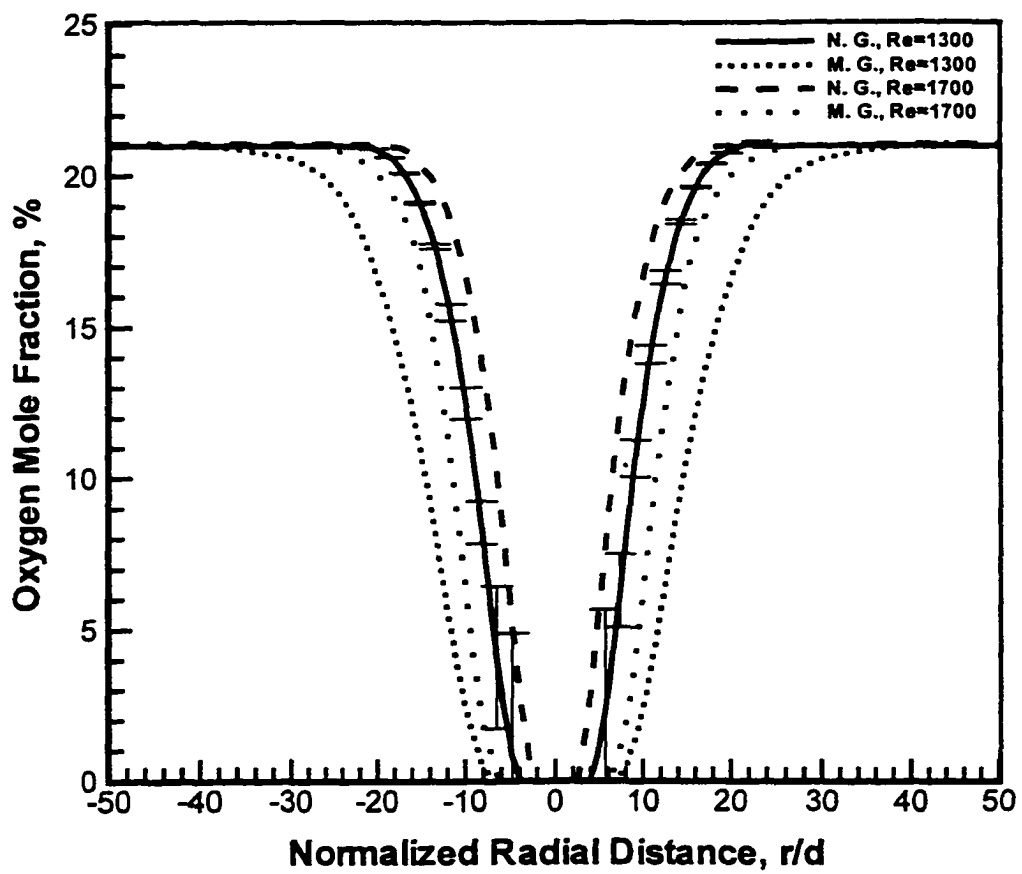


Figure 4.4.9: Buoyancy effect on oxygen mole fraction profiles in normal and microgravity; $d = 0.3$ mm, $z/d = 20$ for $Re = 1700$, and $z/d = 15.3$ for $Re = 1300$

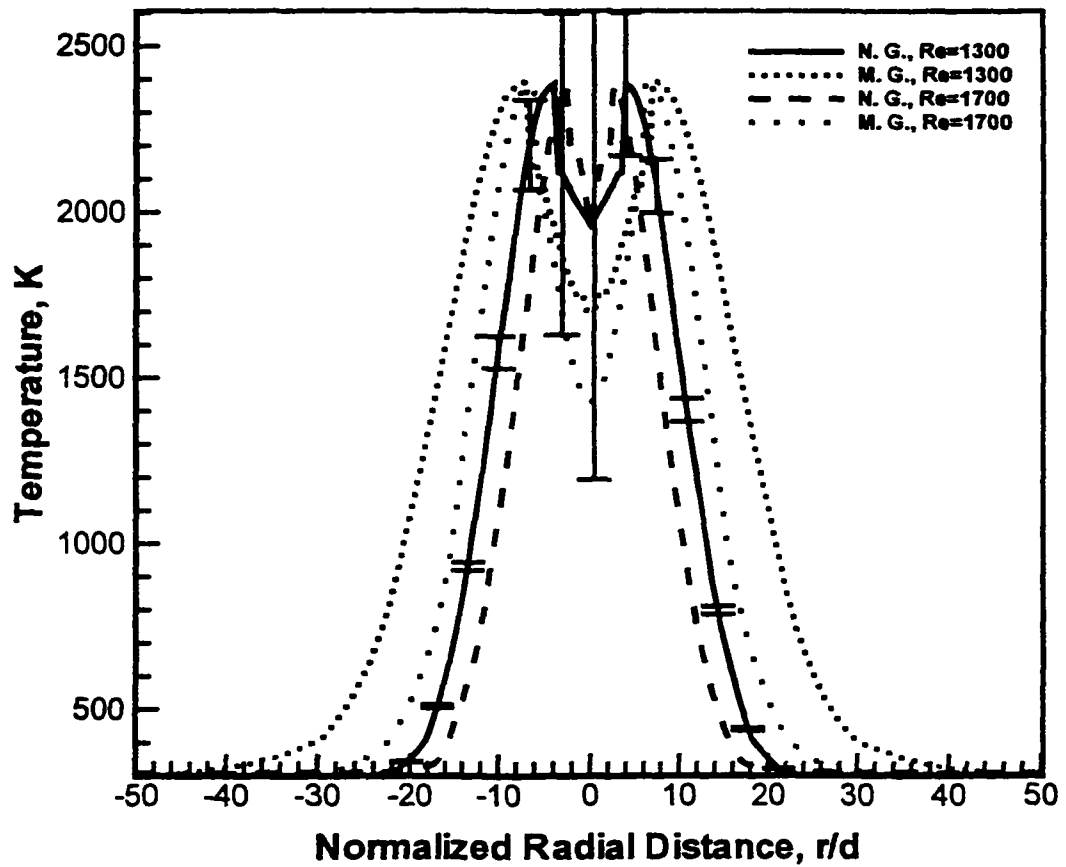


Figure 4.4.10: Buoyancy effect on temperature profiles in normal and microgravity; $d = 0.3$ mm, $z/d = 20$ for $Re = 1700$, and $z/d = 15.3$ for $Re = 1300$

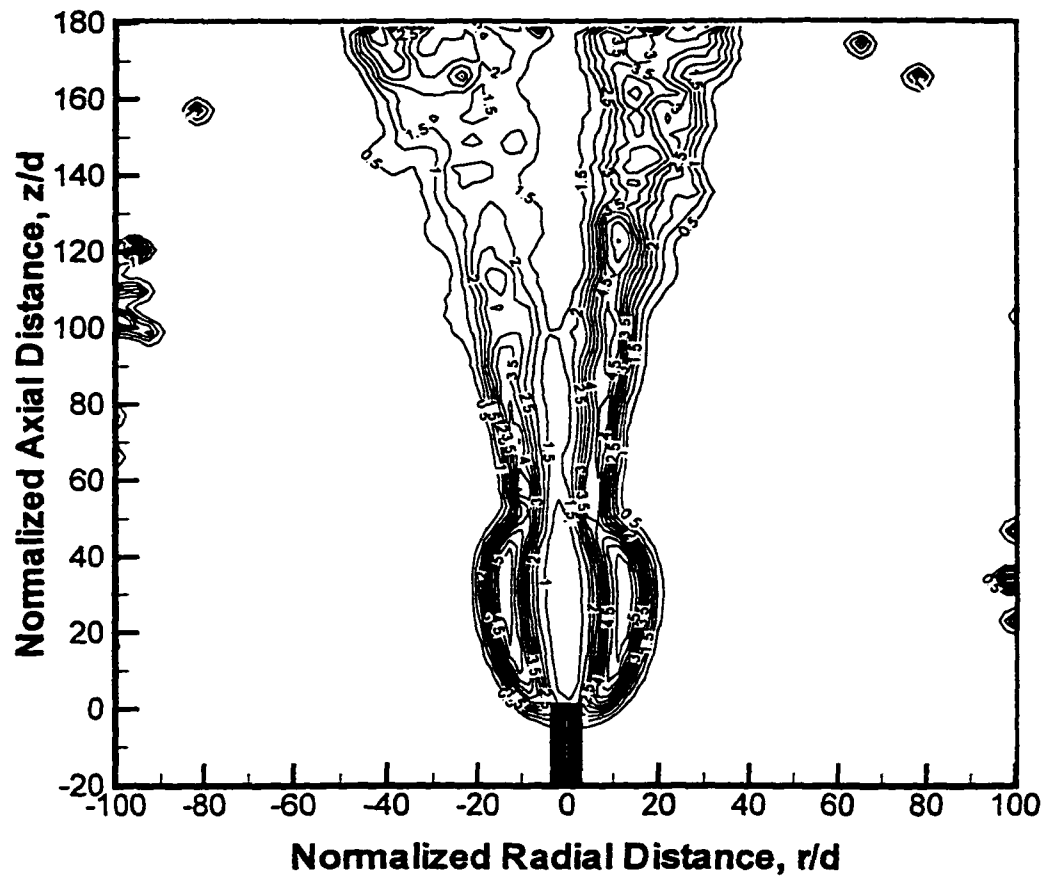


Figure 4.4.11: Contours of angular deflection in units of 10^{-4} radians in normal gravity; $Re = 1700$, $d = 0.3$ mm, and 0.2 He (molar)

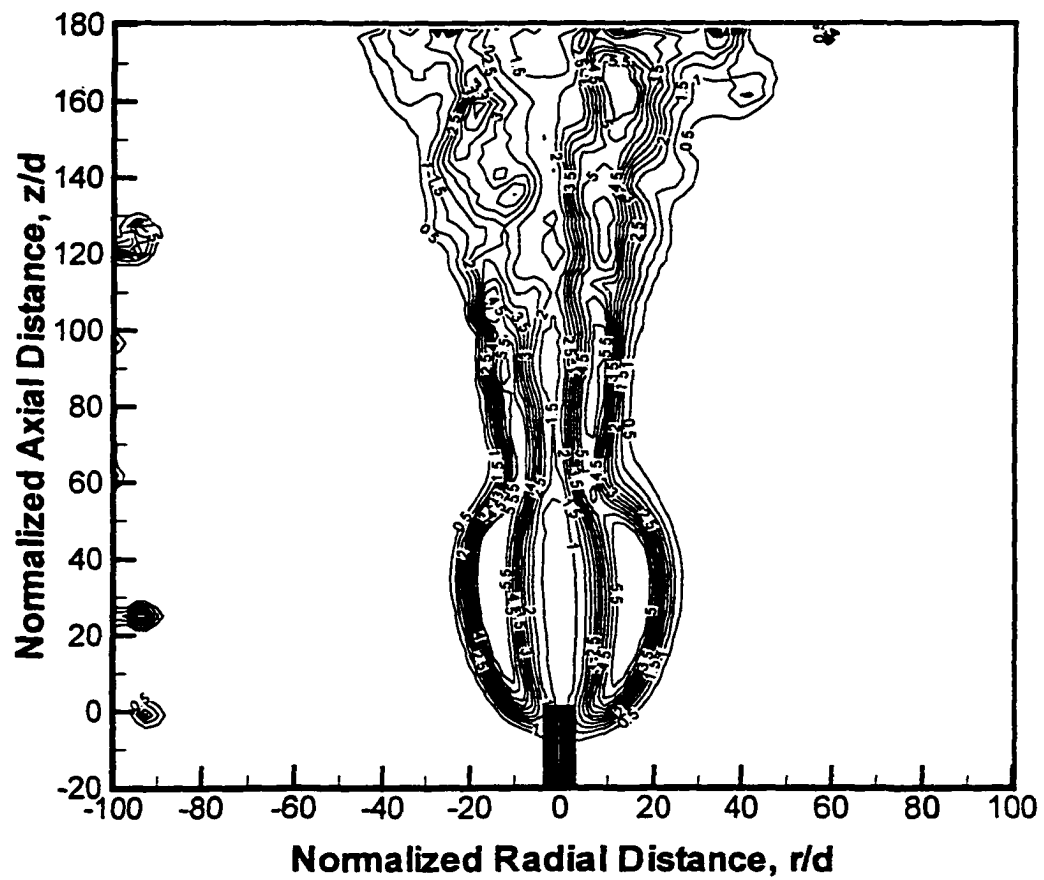


Figure 4.4.12: Contours of angular deflection in units of 10^{-4} radians in microgravity; $Re = 1700$, $d = 0.3$ mm, and 0.2 He (molar)

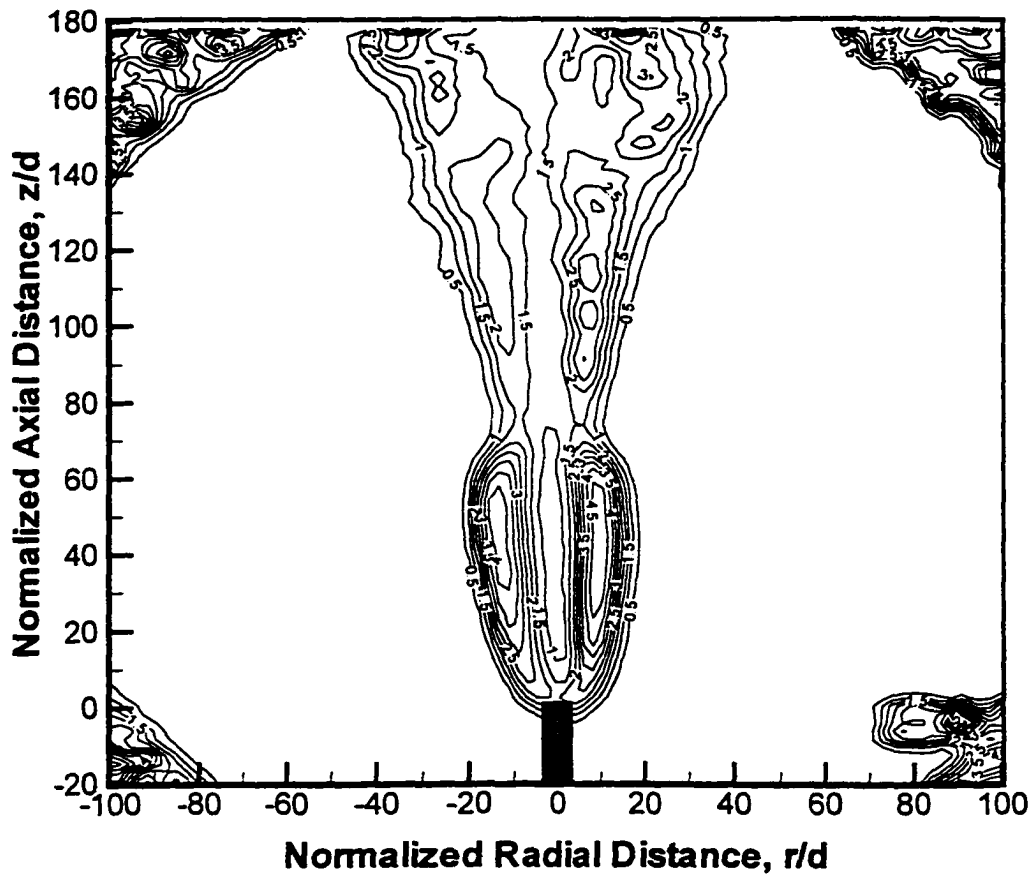


Figure 4.4.13: Contours of angular deflection in units of 10^{-4} radians in normal gravity; $Re = 1700$, $d = 0.3$ mm, and 0.4 He (molar)

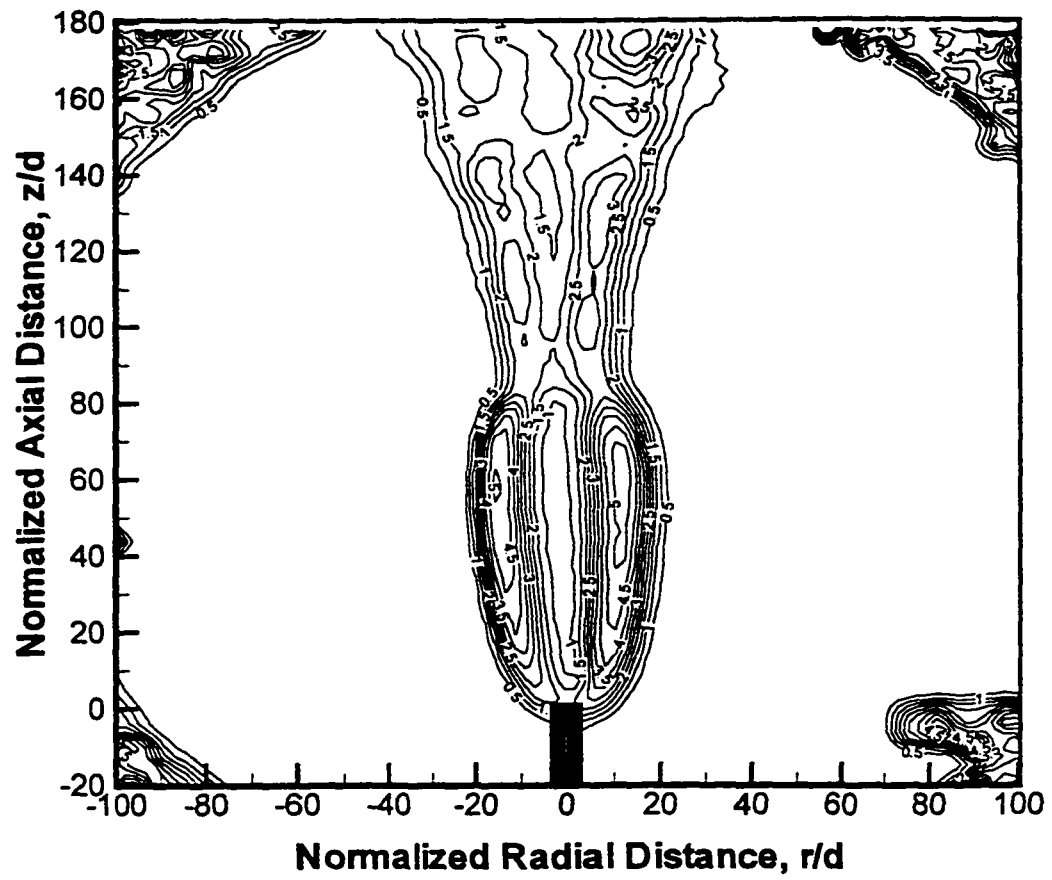


Figure 4.4.14: Contours of angular deflection in units of 10^{-4} radians in microgravity; $Re = 1700$, $d = 0.3$ mm, and 0.4 He (molar)

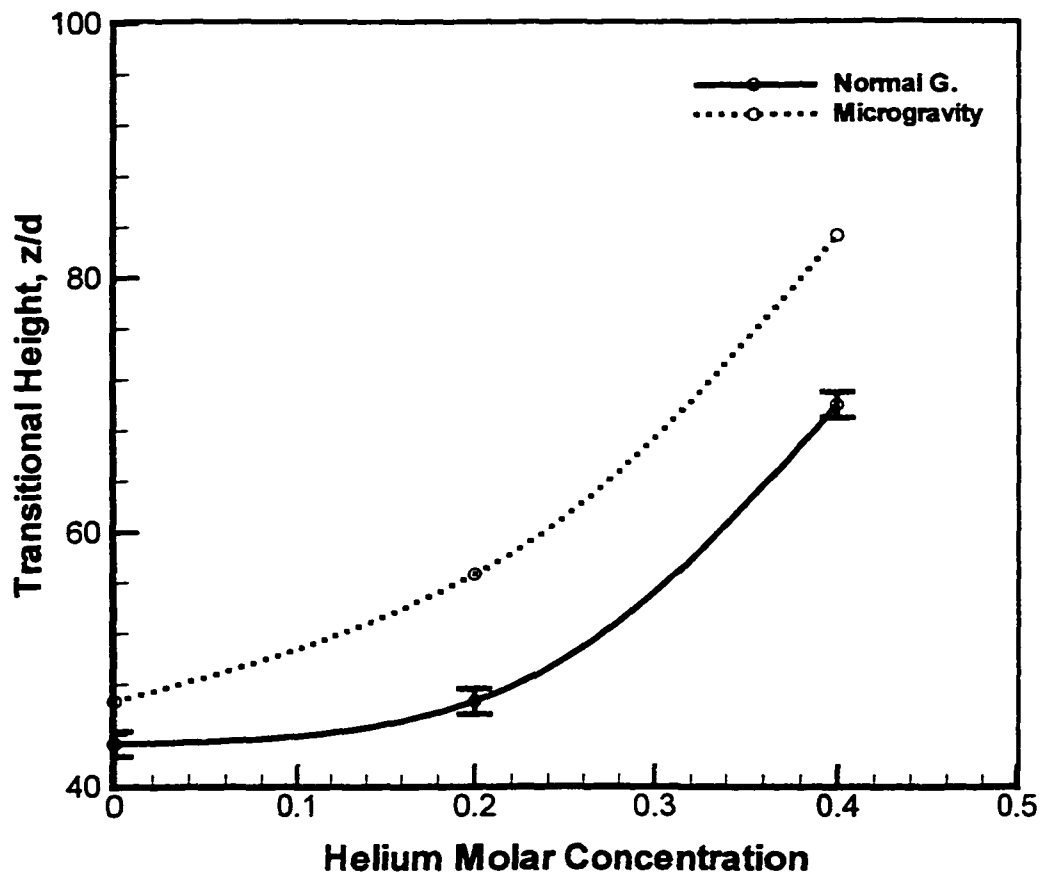


Figure 4.4.15: Transitional height as a function of helium mole fraction in hydrogen; $Re = 1700$ and $d = 0.3$ mm

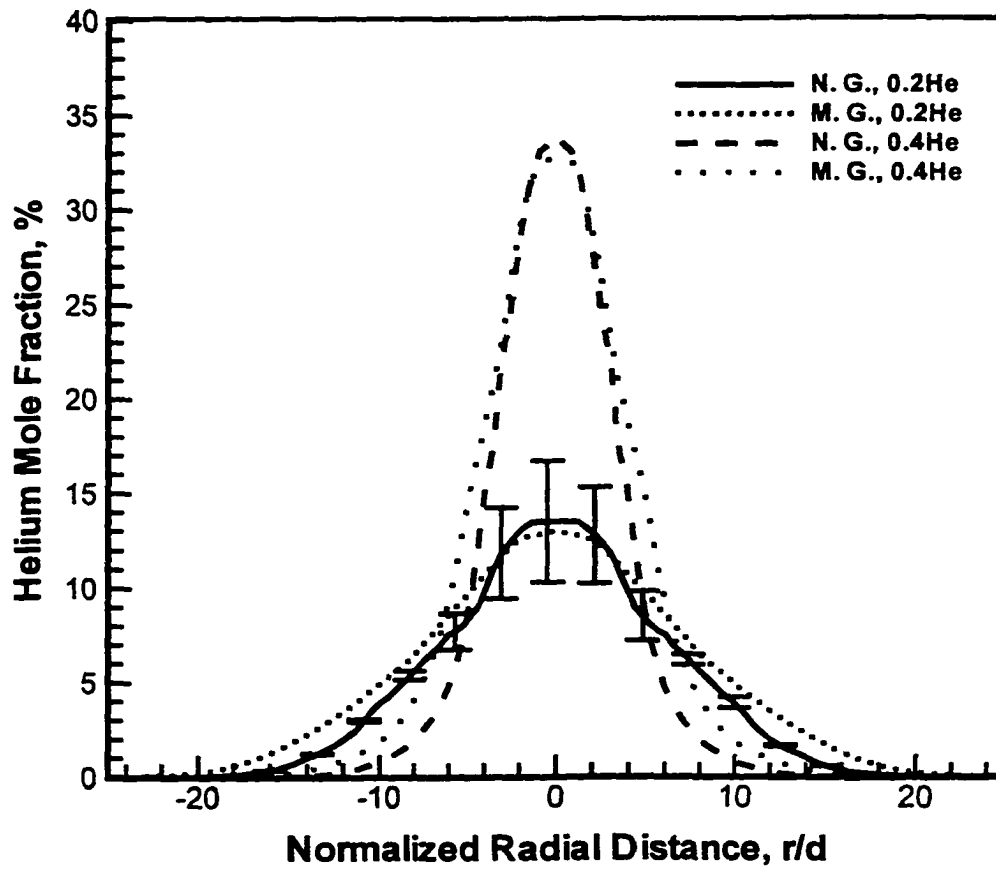


Figure 4.4.16: Helium mole fraction profiles; $Re = 1700$, $d = 0.3$ mm, and $z/d = 20$

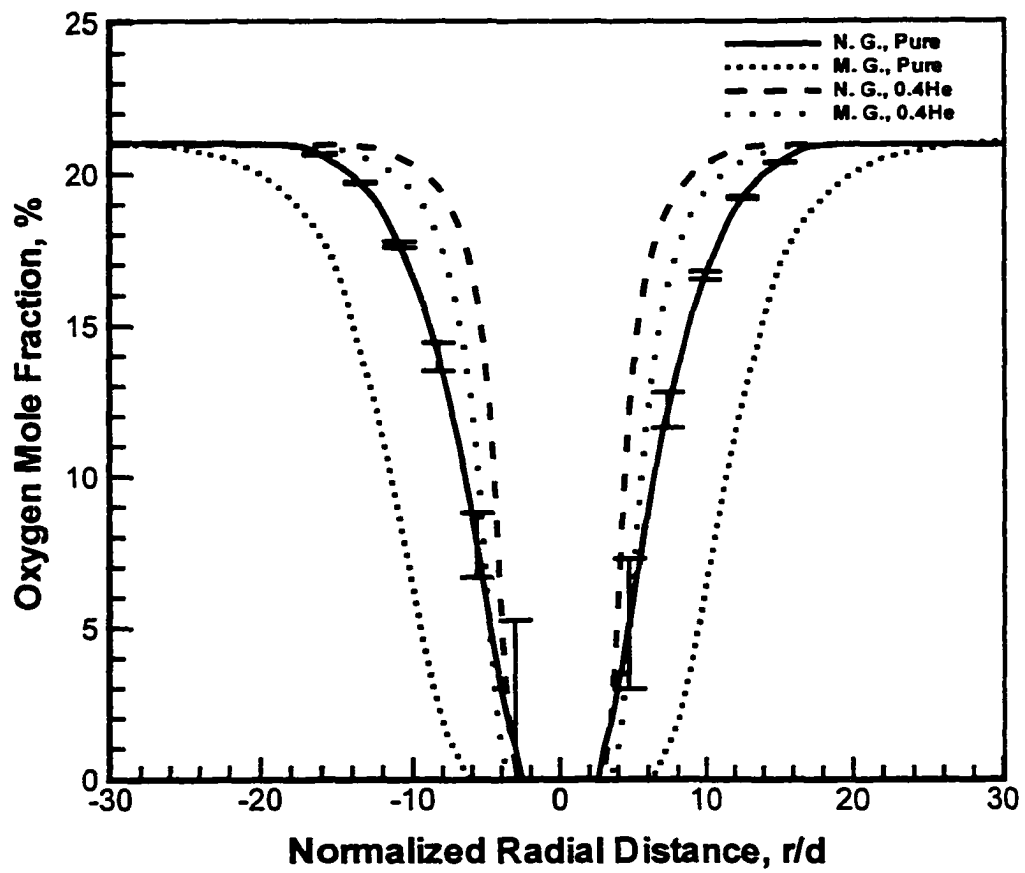


Figure 4.4.17: Helium dilution effect on oxygen mole fraction profiles in normal and microgravity; $Re = 1700$, $d = 0.3$ mm, and $z/d = 20$

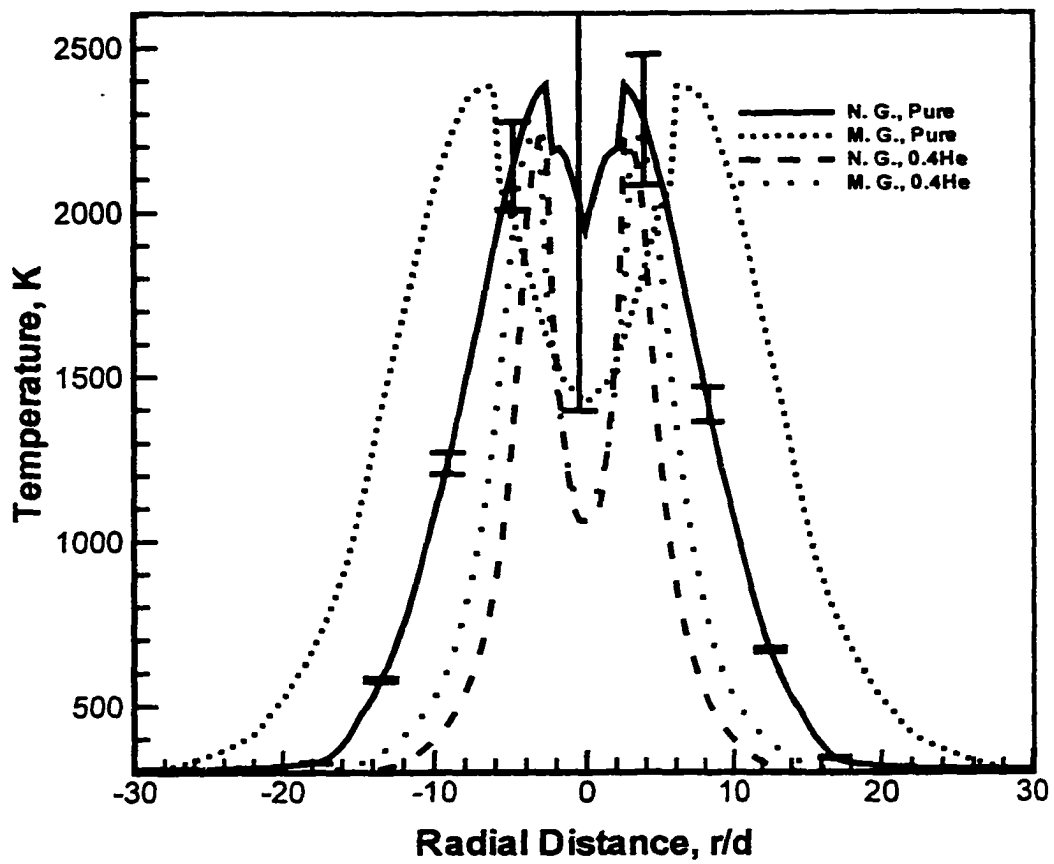


Figure 4.4.18: Helium dilution effect on temperature profiles in normal and microgravity; $Re = 1700$, $d = 0.3$ mm, and $z/d = 20$

Chapter 5

CONCLUSIONS AND RECOMMENDATIONS

The non-intrusive, line-of-sight Rainbow Schlieren Deflectometry (RSD) technique was utilized with chemical equilibrium to quantitatively measure the temperature and oxygen mole fraction profiles in hydrogen gas-jet diffusion flames in normal and microgravity. Comprehensive measurements of temperature and oxygen concentration profiles were obtained. As a first step, the RSD measurements were validated by comparing with data obtained by a thermocouple and a continuous sampling probe. Results show very good agreement between the two measurement techniques in the fuel-lean region of the flame. The RSD measurements were less reliable in the fuel-rich-region because of the chromatic aberration in the decollimating lens, reconstruction errors, high sensitivity of temperature and oxygen mole fraction to the refractive index, and preferential diffusion and/or incomplete combustion effects not accounted for in state relations employing the chemical equilibrium.

As a second step, the validated RSD technique was used to obtain quantitative details of the flame structure in normal and microgravity laminar and transitional gas-jet diffusion flames. Only the near-nozzle laminar portion of the transitional flame was investigated. In particular, the RSD data were used to study the temporal evolution of the flame in the drop tower, scalar profiles, and flame shapes. Important results are summarized in the following:

Time-dependent contours revealed that the angular deflection and hence, the density gradients were smaller in microgravity than those in normal gravity. Transient temperature profiles during transition from normal to microgravity were obtained for laminar flames to show steady-state applicability in the drop tower. These profiles revealed that flames with higher jet exit velocity reached steady-state conditions before flames with lower jet exit velocity. Also, the profiles show that higher temperature regions in the flame reached steady-state faster than the lower temperature regions, and that the low temperature regions did not reach steady-state at a low jet exit velocity.

Effects of burner diameter and Reynolds number on flame shape and scalar profiles in normal and microgravity were evaluated. The flame height varied linearly with Reynolds number, and it was independent of gravity in the range of the Reynolds numbers studied. The flame shape normalized by the burner diameter was nearly independent of the burner diameter. Scalar profiles in microgravity were shown to extend further in the radial direction compared to those in normal gravity. The radial expansion was greater for flames with a higher jet exit velocity.

Two pre-existing theoretical models for axisymmetric diffusion flames in microgravity were considered. One model was based on the similarity analysis and the other model provided an explicit solution. Both models were shown to be inaccurate in the context of this research, in part, because of the low jet exit Reynolds numbers used in experiments. The predicted flame height was four times larger than the measured flame height when the jet exit Reynolds number was used as a parameter. A good agreement was reached when an effective Reynolds number

accounting for the increase in the kinematic viscosity due to combustion was used. The exact solution was inaccurate in predicting the scalar profiles, in part, because of the constant property assumption in the theoretical model. Numerical techniques are, therefore, required to solve the governing equations in reacting flows with sharply varying transport and physical properties.

Finally, the transitional flames were investigated to evaluate the effects of Reynolds number and helium dilution on scalar profiles in the laminar portion of the flame and on flame transition location. It was shown that both in normal and microgravity, the transition point moved upstream as the Reynolds number was increased. It was also shown that the transition was delayed in microgravity. Adding helium to the fuel delayed transition in both normal and microgravity.

Overall, the RSD technique was shown to be effective in visualizing and quantifying hydrogen gas-jet diffusion flames in microgravity. Further research is needed to decrease the measurement errors of the RSD technique. Accordingly, the following recommendations are made:

- Use of reflective-type optics will eliminate chromatic aberrations although difficulties such as spherical aberration may arise.
- A different calibration procedure, such as that using a calibration lens of known refractive index characteristics may prove useful.
- The present RSD apparatus, given the space constraints, can be improved by acquiring color schlieren images at a higher spatial.

- Increasing the effective focal length of the decollimating lens by placing a magnifying lens between the decollimating lens and the color filter will increase the system sensitivity, although this may increase the chromatic aberration.

REFERENCES

1. Agrawal, A. K., Butuk, N. K., Gollahalli, S. R., and Griffin, D., "Three-Dimensional Rainbow Schlieren Tomography of A Temperature Field in Gas Flows," *Applied Optics*, Vol. 37, No. 3, pp. 479-485, 1998.
2. Agrawal, A. K., Cherry, S. M., and Gollahalli, S. R., "Effects of Buoyancy on Steady Hydrogen Gas-Jet Diffusion Flames," *Combustion Science and Technology*, in press, (to be published in 1999).
3. Agrawal, A. K., Shenoy, A. K., Gollahalli, S. R., and Griffin, D., "Gravitational Effects on Transition to Turbulence in Gas-Jet Diffusion Flames," in preparation.
4. Al-Ammar, et al., "Application of Rainbow Schlieren Deflectometry for Concentration Measurements in An Axisymmetric Helium Jet," *Experiments in Fluids*, Vol. 25, No. 2, pp. 89-95, 1998.
5. Bahadori, M. Y., Edelman, R. B., Stocker, D. P., and Olson, S. L., "Ignition and Behavior of Laminar Gas-Jet Diffusion Flames in Microgravity," *AIAA Journal*, Vol. 28, No. 2, pp. 236-244, 1990.
6. Bahadori, M. Y., Stocker, D. P., Vaughan, D. F., Zhou, L., and Edelman, R. B., "Effects of Buoyancy on Laminar, Transitional, and Turbulent Gas Jet Diffusion Flames," In Williams, F. A., Oppenheim, A. K., Olfe, D. B., and Lapp, M. (Eds.), *Modern Developments in Energy, Combustion and Spectroscopy*, Pergamon Press, pp. 49-66, 1993.
7. Bilger, R. W., "The Structure of Diffusion Flames," *Combustion Science and Technology*, Vol. 13, pp. 155-170, 1976.

8. Bray, K. N. C., "Hottel Plenary Lecture : The Challenge of Turbulent Combustion," *Twenty-Sixth Symposium (International) on Combustion*, The Combustion Institute, Pittsburgh, PA, pp. 1-26, 1996.
9. Brown, T. M., Tanoff, M. A., Osborne, R. J., Pitz, R. W., and Smooke, M. D., "Experimental and Numerical Investigation of Laminar Hydrogen-Air Counterflow Diffusion Flames," *Combustion Science and Technology*, Vol. 131, pp. 77-88, 1998.
10. Burke, S. P. and Schumann, T. E. W., "Diffusion Flames," *Industrial and Engineering Chemistry*, vol. 20, p. 998, 1928.
11. Cochran, T. H., "Experimental Investigation of Laminar Gas Jet Diffusion Flames in Zero Gravity," *NASA TN D-6523*, NASA Lewis Research Center, Cleveland, OH, 1972.
12. Cochran, T. H. and Masica, W. J., " An Investigation of Gravity Effects on Laminar Gas-Jet Diffusion Flames, " *Thirteenth Symposium (International) on Combustion*, The Combustion Institute, Pittsburgh, PA, pp. 821-829, 1971.
13. Dasch C., "One-Dimensional Tomography: A Comparison of Abel, Onion-Peeling, and Filtered Backprojection Methods," *Applied Optics*, Vol. 31, 1146-1152, 1992.
14. Eckbreth, A. C., "Laser Diagnostics For Combustion Temperature and Species," *Overseas Publishers Association*, Amsterdam B.V., 1996.
15. Edelman R. B. and Bahadori, M. Y., "Effects of Buoyancy on Gas-Jet Diffusion Flames : Experiment and Theory," *Acta Astronautica*, Vol. 13, No. 11/12, pp. 681-688, 1986.

16. Edelman, R. B., Fortune, O. F. and Weilerstein, G., "An Analytical and Experimental Investigation of Gravity Effects Upon Laminar Gas Jet-Diffusion Flames," *Fourteenth Symposium (International) on Combustion*, The Combustion Institute, Pittsburgh, PA., pp. 3999-412, 1973.
17. Faeth, G. M. and Samuelsen, G. S., "Fast Reaction Nonpremixed Combustion," *Progress in Energy and Combustion Science*, Vol. 12, pp. 305-372, 1986.
18. Fay, J. A. "The Distribution of Concentration and Temperature in a Laminar Jet Diffusion Flame," *Journal of Aeronautical Sciences*, Vol. 21, pp. 681-689, 1954.
19. Fristrom, R. M., *Flame Structure and Processes*, Oxford University Press, New York, NY, 1995.
20. Goldstein, R. J. and Kuehn, T. H., *Fluid Mechanics Measurements*, chapter 7, Taylor and Francis, Washington DC, 1996.
21. Goldstein, S., *Modern Developments in Fluid Dynamics*, Section 57, Oxford University Press, 1938.
22. Greenberg, P. S., Klimek, R. B., and Buchele, D. R., "Quantitative Rainbow Schlieren Deflectometry," *Applied Optics*, Vol. 34, 3810-3822, 1995.
23. Haggard J. B., JR. and Cochran T. H., "Stable Hydrocarbon Diffusion Flames in a Weightless Environment," *Combustion Science and Technology*, Vol. 5, pp. 291-298, 1972.
24. Hawthorne, W. R., Weddell, D. S., and Hottel, H. C., "Mixing and Combustion in Turbulent Gas Jets," *Third Symposium on Combustion, Flame, and Explosion Phenomena*, Williams & Wilkins, Baltimore, pp. 266-288, 1949.
25. Hegde, U. and Bahadori, M. Y., "An Analytical Model For Gravitational Effects

- On Burke-Schumann Flames,” *Western States Meeting of the Combustion Institute*, Fall, 1992.
26. Hegde, U. and Zhou, L., “The Transition to Turbulence of Microgravity Gas Jet Diffusion Flames,” *Combustion Science and Technology*, Vol. 102, pp. 95-113, 1994.
27. Holman, J. P., *Experimental Methods for Engineers*, Chapter 8, McGraw-Hill, 1989.
28. Howes, W. L., “Rainbow Schlieren and Its Applications,” *Applied Optics* Vol. 23, 2449-2460, 1984.
29. Kee, R. J., Rupley, F. M., and Miller, J. A., “Chemkin II : A FORTRAN Chemical Kinetics Package for the Analysis of Gas Phase Chemical Kinetics,” *SAND89-809B-UC-706*, 1993.
30. Kuo, K. K., *Principles of Combustion*, Chapter 1, John Wiley & Sons, New York, 1986.
31. Lekan, J., “Microgravity Research in NASA Ground-Based Facilities,” *NASA TM-101397*, NASA Lewis Research Center, Cleveland, Ohio, 1996.
32. Lin, K. C., Faeth, G. M., Sunderland, P. B., Urban, D. L., and Yuan, Z. G., “Shapes of Nonbuoyant Round Luminous Hydrocarbon/Air Laminar Jet Diffusion Flames,” *Combustion and Flame*, Vol. 116, pp. 415-431, 1999.
33. Linan, A. and Williams, F. A., *Fundamental Aspects of Combustion*, Chapter 3, Oxford University Press, 1993.
34. Mahalingam, S., Ferziger J. H., and Cantwell, B. J., “Brief Communications : Self-Similar Diffusion Flame,” *Combustion and Flame*, Vol. 82, pp. 231-234,

1990.

35. Miller, J. A. and Kee, R. J., "Chemical Nonequilibrium Effects in Hydrogen-Air Laminar Jet Diffusion Flames," *The Journal of Physical Chemistry*, V. 81, No. 25, pp. 2534-2542, 1977.
36. Parthasarathy, R. N. and Emanuel, G., personal discussion, 1998.
37. Roper, F. G., "The Prediction of Laminar Jet Diffusion Flame Sizes : Part I. Theoretical Model," *Combustion and Flame*, Vol. 29, pp. 219-226, 1977.
38. Rubinstein, R., Greenberg, P. S., "Rapid Inversion of Angular Deflection Data for Certain Axisymmetric Refractive Index Distributions," *Applied Optics*, Vol. 33, 1141-1144, 1994.
39. Savas, O. and Gollahalli, S. R., "Stability of Lifted Laminar Round Gas-Jet Flame," *Journal of Fluid Mechanics*, Vol. 165, pp. 297-318, 1986.
40. Shenoy, A. K., *Effects of Non-Unity Lewis Number and Buoyancy in Hydrogen Jet Diffusion Flames*, M.S. Thesis, School of Aerospace and Mechanical Engineering, University of Oklahoma, Norman, Oklahoma, 1998.
41. Shenoy, A. K., Agrawal A. K., and Gollahalli, S. R., " Quantitative Evaluation of Flow Computations by Rainbow Schlieren Deflectometry, *AIAA Journal*, Vol. 36, pp. 1953-1960, 1998.
42. Silver, J. A., Kane, D. J., and Greenberg, P. S., "Quantitative Species Measurements in Microgravity Flames with Near-IR Diode Lasers," *Applied Optics*, Vol. 34, No. 15, pp. 2787-2801, 1995.
43. Sivathanu, Y. R. and Faeth, G. M., "Generalized State Relationships for Scalar Properties in Nonpremixed Hydrocarbon/Air Flames," *Combustion and Flame*,

Vol. 82, pp. 211-230, 1990.

44. Spalding, D. B., *Combustion and Mass Transfer*, Chapters 9 and 10, Pergamon Press, 1979.
45. Spalding, D. B., "Mixing and Chemical Reaction in Steady Confined Turbulent Flames," *Thirteenth Symposium (International) on Combustion*, The Combustion Institute, Pittsburgh, PA, pp. 649-657, 1971.
46. Stocker, D. P., "Size and Shape of Laminar Burke-Schumann Diffusion Flames in Microgravity," *Proceedings of the 1990 Spring Technical Meeting of the Central States*, The Combustion Institute, pp. 281-286, May 1990.
47. Sunderland, P. B., Mendelson, B. J., Yuan, Z. G., and Urban, D. L., "Shapes of Buoyant and Nonbuoyant Laminar Jet Diffusion Flames," *Combustion and Flame*, Vol. 116, pp. 376-386, 1999.
48. Sunderland, P. B., Mortazavi, S., and Faeth, G. M., "Laminar Smoke Points of Nonbuoyant Jet Diffusion Flames," *Combustion and Flames*, Vol. 96, pp. 97-103, 1994.
49. Tittmann, K., Sitzki, L., Bringezu, D., Rau, H., and Grabski, R., "Hydrogen Diffusion Flames under Microgravity," *Microgravity Science Technology*, Hanser Publishers, Munich, Vol. IX/I, pp. 40-45, 1996.
50. Tittmann, K., Sitzki, L., Rau, H., Wienecke, F., and Grabski, R., "Concentration and Temperature Profiles of Diffusion Flames in Drop tower Experiments," *AIAA Journal*, Vol. 36, No. 9, pp. 1743-1744, 1998.
51. Vasil'ev, L. A., "Schlieren Methods," *Israel Program for Scientific Translation*, New York, pp. 176-177, 1971.

52. Wehrmeyer, J. A., Yeralan, S., and Tecu, K. S., "Influence of Strain Rate and Fuel Dilution on Laminar Nonpremixed Hydrogen-Air Flame Structure," *Combustion and Flame*, Vol. 107, pp. 125-140, 1996.
53. Yates, L. A., "Constructed Interferograms, Schlieren and Shadowgraphs: A User's Manual," *NASA CR-194530*, 1993.

APPENDIX A

The governing equation for the mixture friction is given by

$$u \frac{\partial f}{\partial x} + v \frac{\partial f}{\partial r} = \frac{D}{r} \frac{\partial}{\partial r} \left(r \frac{\partial f}{\partial r} \right) \quad (\text{A.1})$$

with boundary conditions :

$$r = 0 : \quad \frac{\partial f}{\partial r} = 0 \quad (\text{A.2a})$$

$$r \rightarrow \infty : \quad f = 0 \quad (\text{A.2b})$$

Let

$$f = \frac{D}{z} G(\eta) \quad (\text{A.3a})$$

$$u = \frac{v}{z} \frac{F'}{\eta} \quad \text{and} \quad v = \frac{v}{z} \left(F' - \frac{F}{\eta} \right) \quad (\text{Goldstein, 1938}) \quad (\text{A.3b})$$

where $\eta = \frac{y}{z}$ and the derivatives are with respect to η .

Substituting (A.3) into equation (A.1) and simplifying, we have

$$-v (F'G + FG') = D(G' + G''\eta) \quad (\text{A.4})$$

Integrating equation (A.4) once, we get

$$-v FG = DG'\eta + C \quad (\text{A.5})$$

$$\text{with } F=0 \text{ at } \eta = 0 \quad \Rightarrow \quad C = 0 \quad (\text{A.6})$$

Now let

$$\xi = \gamma\eta \quad (\text{A.7})$$

where γ is a constant of integration determined from the initial momentum flux.

Substituting (A.6) and (A.7) into (A.5) and rearranging, we obtain

$$\frac{dG}{G} = -Sc \frac{F}{\xi} d\xi \quad (A.8)$$

Here,

$$F = \frac{\xi^2}{1 + \frac{1}{4}\xi^2} \quad (\text{Goldstein, 1938}) \quad (A.9)$$

Substituting (A.9) into equation (A.8) and integrating, we get

$$G = \frac{A}{\left(1 + \frac{1}{4}\xi^2\right)^{2Sc}} \quad (A.10)$$

Where A is a constant of integration determined from the initial flux of the mixture fraction, and is given in our case as follows :

$$2\pi \int_0^{\infty} u f r dr = d^2 u_0 = 16\nu DA \int_0^{\infty} \frac{\xi d\xi}{\left(1 + \frac{1}{4}\xi^2\right)^{2Sc}}$$

or

$$A = \frac{Re d}{32 D} (2Sc + 1) \quad (A.11)$$

Substituting equation (A.10) and (A.11) into (A.3a), we obtain

$$f = \frac{2Sc + 1}{32} \left(\frac{Re \cdot d}{z}\right) \left(1 + \frac{1}{4}\xi^2\right)^{-2Sc} \quad (A.12)$$

APPENDIX B

Sample Calculations

Radiation correction for Thermocouple Readings

The steps for calculating the temperature correction due to radiation from the thermocouple (Pt-Pt 13% Rh) reading of 1500 K, which corresponds to about $r = 4.4$ mm (see Fig. 4.2.6) are given below. The bead diameter, D was 0.7 mm. A surrounding temperature, T_s of 300 K was assumed. A balance between convective and radiative heat transfer to the thermocouple results in the following:

$$h(T_g - T_t) = \epsilon\sigma(T_t^4 - T_s^4)$$

Hence,

$$T_g = \frac{\epsilon\sigma(T_t^4 - T_s^4)}{h} + T_t \quad (\text{B.1})$$

where the subscripts g , t , and s correspond to the gas, thermocouple, and surrounding, respectively. Also, ϵ is the thermocouple emissivity, $\sigma = 5.669 \times 10^{-8} \text{ W/m}^2 \cdot \text{K}^4$ is Stefan-Boltzmann constant, and h is the average heat transfer coefficient given as follows (Holman, 1989):

$$h = \frac{0.37kRe^{0.6}}{D} \quad \text{W/m}^2 \cdot ^\circ\text{C} \quad (\text{B.2})$$

Here, k is thermal conductivity of the thermocouple, D is the bead diameter, and Re is the Reynolds number based on D . The following curve-fit relations were used to evaluate the properties:

$$u(r) = -0.023r^2 + 0.0094r + 7.7 \text{ m/s} \quad (\text{B.3})$$

Here, the velocity was based on the exit jet velocity plus 20 % to account for buoyant acceleration near the nozzle.

$$\varepsilon(T) = 0.00010T + 0.03 \quad (\text{B.4})$$

$$k(T) = -1.3393 \times 10^{-8} T^2 + 7.4690 \times 10^{-5} T + 5.5583 \times 10^{-3} \text{ W/m} \cdot ^\circ \text{C} \quad (\text{B.5})$$

and finally, the kinematic viscosity of the fluid, assumed air, is given as follows:

$$\nu(T) = 5.0893 \times 10^{-11} T^2 + 8.4286 \times 10^{-8} T - 1.6732 \times 10^{-5} \text{ m}^2 / \text{s} \quad (\text{B.6})$$

First, the Reynolds number is obtained from equations (B.3) and (B.6) using $r = 4.4 \text{ mm}$ and $T = 1500 \text{ K}$. This gives $Re = 22.8$. Next, the average heat transfer coefficient is obtained from equation (B.2), which gives $h = 301.8 \text{ W/m}^2 \cdot ^\circ \text{C}$. Also, the thermocouple emissivity is calculated from equation (B.4) to be 0.18. Now, the temperature of the gas can be obtained from equation (B.1), which a value of 1695 K for the gas temperature after one iteration.

Theoretical Calculation of Oxygen and Temperature Profiles

Next, calculations of oxygen mole fraction and temperature profiles and flame height are considered for $Re_\tau = 130$, $d = 1.19 \text{ mm}$, $Sc = 0.2$ at $z/d = 4$ and $r/d = 30$. First, the parameters a and b are calculated, respectively, from equations (2.14) and (2.15) as follows:

$$Re_\tau^2 = 32 \left[\frac{8(a+1)}{3a(a+2)} + (a+1)^2 \ln\left(\frac{a}{a+2}\right) + 2(a+1) \right] = 16900$$

which gives $a = 0.0025$. Also,

$$b = \frac{4Sc^2 - 1}{(2Sc + a + 1)(a + 2)^{-2Sc} + (2Sc - a - 1)a^{-2Sc}} = 0.151.$$

Next, the mixture fraction is obtained from equation (2.13) as follows:

$$f = \frac{Re_T d}{32\sqrt{r^2 + z^2}} \frac{b}{\left(1 + a - \frac{z}{\sqrt{r^2 + z^2}}\right)^{2Sc}} \left(\frac{\rho_0}{\rho_\infty}\right)^{\frac{1}{2}} = 0.0058.$$

The oxygen mole fraction and temperature is obtained from the lookup-table generated from the chemical equilibrium calculation (see Figs. B1 and B.2). For $f = 0.0058$, the oxygen mole fraction is 17.7 and the temperature is 921 K (see Fig. 4.3.50). The flame height is calculated from equation (2.16) as

$$\frac{z_{flame}}{d} = \frac{Re b}{32a^{2Sc} f_{st}} = 59$$

where $f_{st} = 0.03$ and $d = 1.19$ mm are used.

Uncertainty Analysis

The angular deflection, ε , is given by equation (3.2) in Chapter 3 as follows:

$$\varepsilon = \frac{d}{f} \tag{B.7}$$

where d is the displacement at the filter plane and $f = 1000$ mm is the focal length of the decollimating lens in the RSD apparatus. The uncertainty in the angular deflection is given by equation (3.11) as follows:

$$\Delta\varepsilon = \frac{\Delta d}{f} \tag{B.8}$$

Assuming a hue of 150 degrees, the filter calibration table (see Fig. 3.5) gives a displacement of 0.4 mm. Using equation (B.7), the angular deflection is obtained as follows:

$$\varepsilon = \frac{d}{f} = 4 \times 10^{-4} \text{ radians.}$$

The uncertainty in hue is also obtained from the filter calibration curve (the standard deviation at hue = 150 degrees). Hence, $\Delta\varepsilon = 7$ degrees. Adding 7 degrees to the hue value of 150 gives a displacement of 0.42 mm. Hence, the uncertainty in the displacement is 0.02 mm. Finally, the uncertainty in the angular deflection is obtained from equation (B.8) as follows:

$$\Delta\varepsilon = \frac{\Delta d}{f} = 2 \times 10^{-5} \text{ radians.}$$

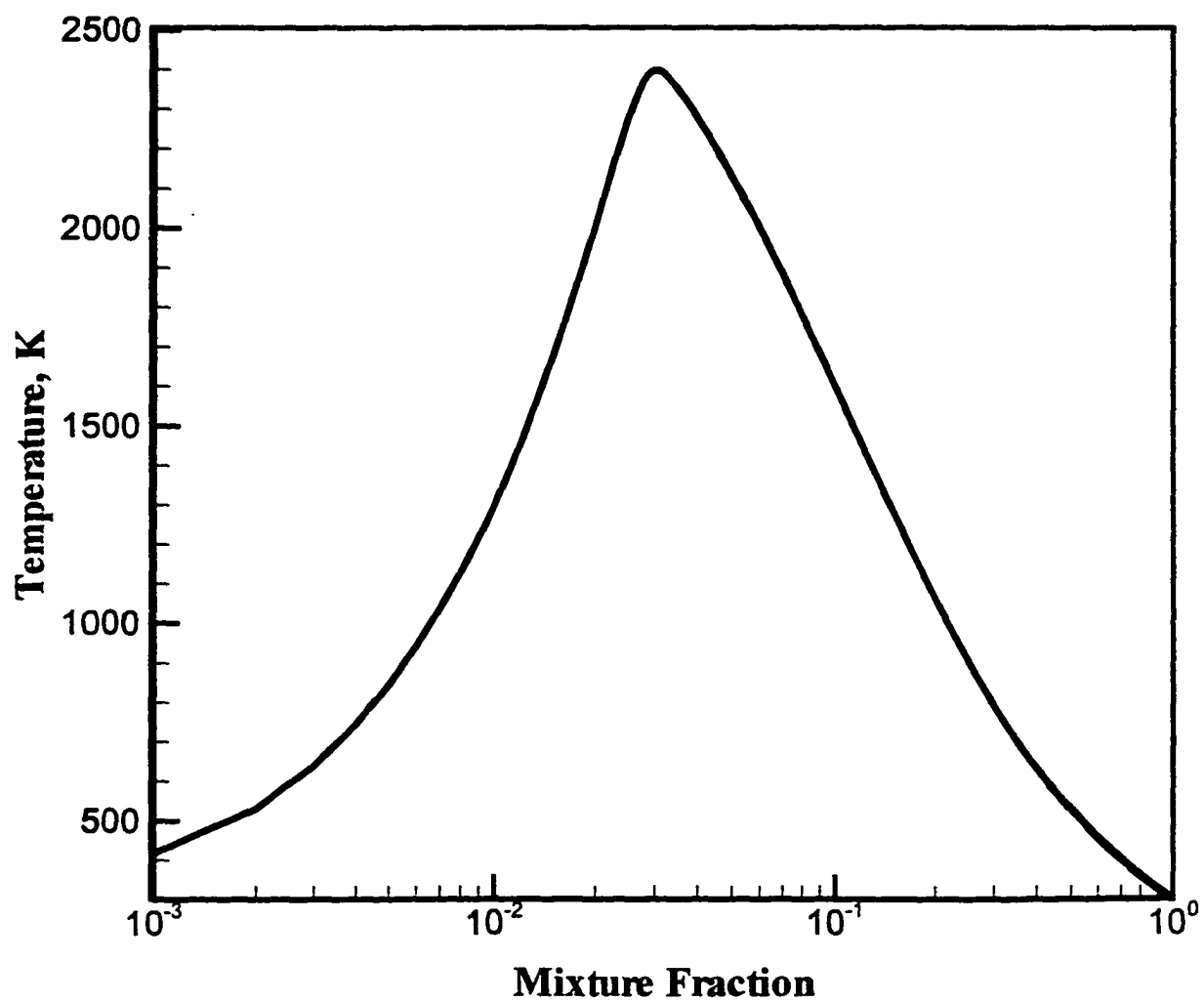


Figure B1: Temperature versus mixture fraction as obtained from chemical equilibrium calculation

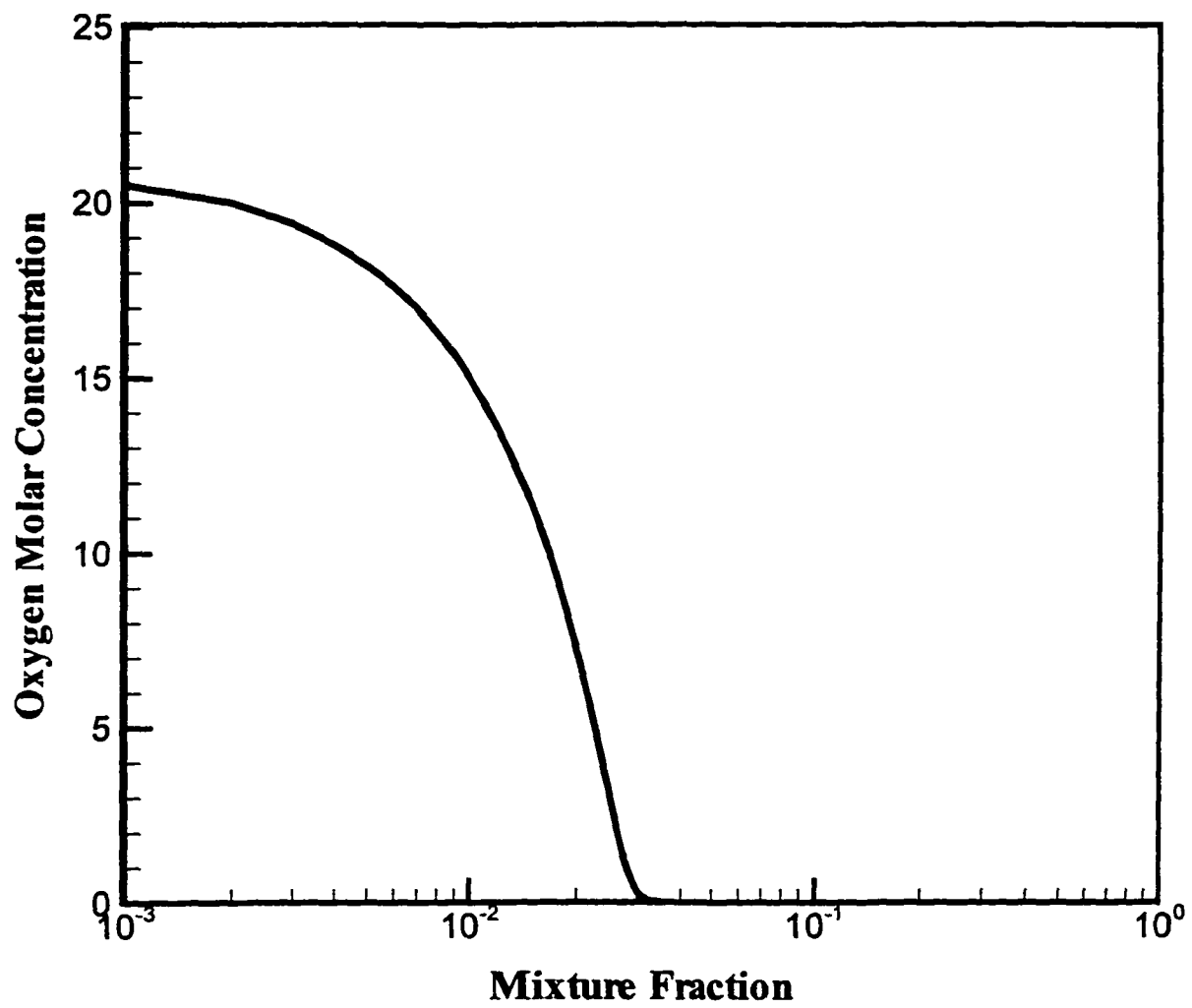
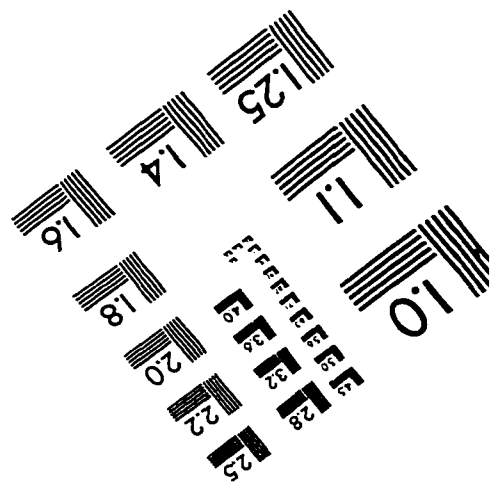
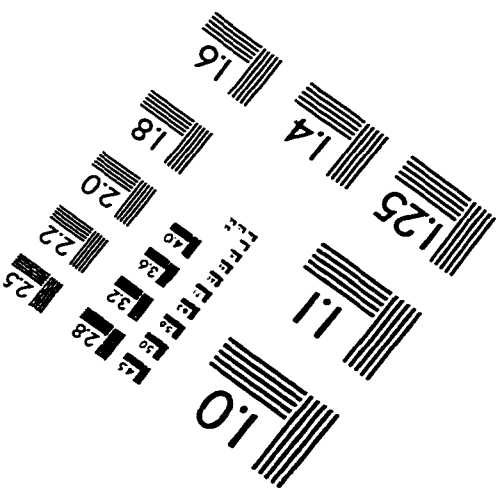
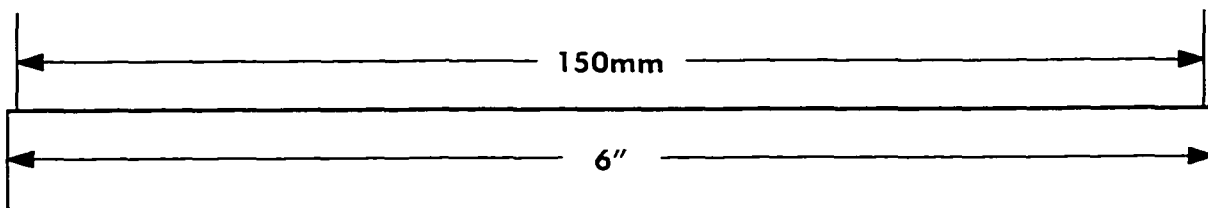
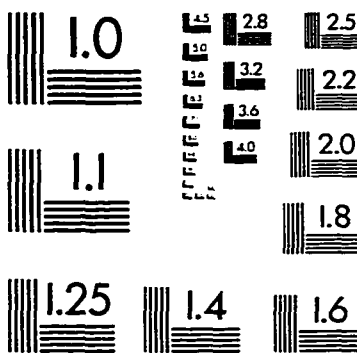
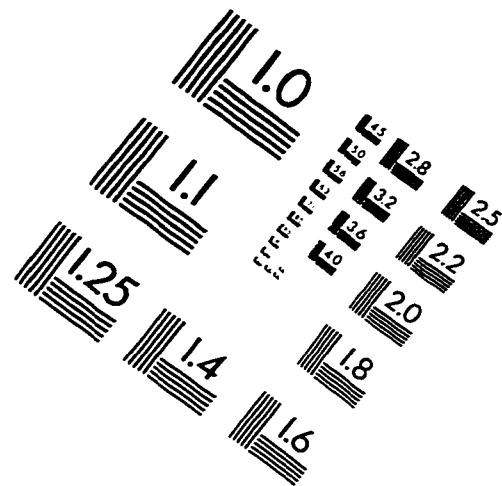
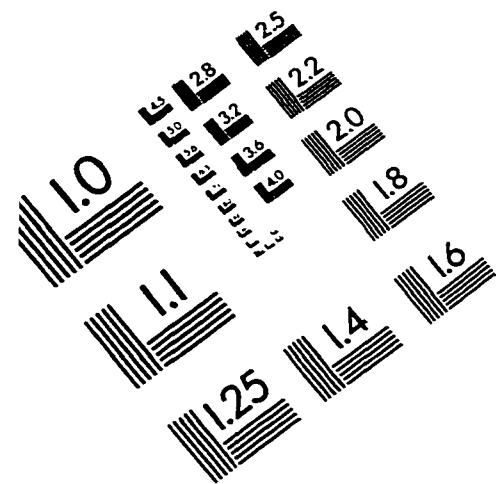


Figure B2: Oxygen mole fraction versus mixture fraction as obtained from chemical equilibrium calculation

IMAGE EVALUATION TEST TARGET (QA-3)



APPLIED IMAGE . Inc
1653 East Main Street
Rochester, NY 14609 USA
Phone: 716/482-0300
Fax: 716/288-5989

© 1993, Applied Image, Inc., All Rights Reserved